Hail statistics for European countries

Zur Erlangung des akademischen Grades eines
DOKTORS DER NATURWISSENSCHAFTEN
von der Fakultät für Physik des
Karlsruher Instituts für Technologie (KIT)

genehmigte

DISSERTATION

von

M.Sc. Elody Fluck
aus Andlau (France)

Tag der mündlichen Prüfung:	12 Mai 2017
Referent:	Prof. Dr. Michael Kunz
Korreferent:	Prof. Dr. Christoph Kottmeier

Abstract

This work presents an analysis of the spatiotemporal variability of hail in Germany, France, Belgium, and Luxembourg for the period 2005-2014. As conventional observation data, such as weather stations or individual observations, are neither accurate nor available comprehensively to establish a climatology of hail, proxies estimated from 2D radar data combined with lightning data were used to produce a high-resolution hail potential composite of 1×1 km^2. This study describes the first hail potential derived from radar data including analysis of the pre-convective environments using ERA-Interim reanalysis data.

Individual past hailstorm trajectories were reconstructed using a cell-tracking algorithm adapted and applied on 2D radar composites corrected beforehand and filtered with lightning data. For the detection of hail in the radar data, the simplified Mason (1971) criterium was applied that considers a radar reflectivity more than 55 dBZ as hail signal. A radar convective severity index (RCSI) was developed and estimated for each hail swath detected by the algorithm to determine the severity of a swath and to compare among all reconstructed past events. The most severe event recorded during the 10-year period occurred on 9 June 2014 and crossed France and Belgium as well as the western part of Germany. Another severe hailstorm on 28 July 2013 affecting South-West Germany was the second most severe swath.

The hail potential is investigated and discussed regarding various influencing factors relevant to severe convective storms. On the local-scale, orographically-driven flow deviations play an important role in the development of convection on the leeward side, which is found as favored regions for hail occurrence. In this area, low-level moist convergence permits a vertical rise of air, and a moisture supply favors an air parcel to reach the level of free convection required for the development of deep moist convection. Pre-convective environments in terms of thermal stability, wind speed, and other quantities relevant for convection are analyzed near hail onsets using reanalysis data. The regions most affected by hail have, for example, high wind shear permitting the development of organized convective storms that can produce large hail. Also, a capping inversion of temperature due to dry and warm flow coming from South-West Europe at upper-tropospheric scales combined with moist and colder air advection coming from the Atlantic at lower levels are favorable environments for the development of deep moist convection.

Contents

1. Introduction

Convective storms and related hail constitute a major atmospheric risk in various parts of Europe, including Southern France, Germany, Austria, and Switzerland (for example Dessens, 1986; Punge and Kunz, 2016; Puskeiler et al., 2016; Nisi et al., 2016). Several studies show that the number of hail-damage days increased substantially in the last two decades, which may be related to an increase in the convective potential of the atmosphere (Soden and Held, 2006; Kunz et al., 2009; Mohr and Kunz, 2013). However, because of the local-scale extent of hail affected areas, referred to as hail streaks, with typical widths only between several hundred meters to several kilometers, hail is not captured accurately and uniquely by a single observation system. Currently, there are no dedicated and automatic monitoring systems for hail detection installed with sufficient spatial coverage. Numerical models, such as weather forecasts or regional climate models (RCM), on the other hand, are also not able to reliably reproduce these storms due to a high degree of uncertainty in the initial conditions, a lack of knowledge in cloud microphysics, and the low resolution of the models. Therefore, little is known about the hail probability and hail risk within Europe. Since hail damage can cost more than one billion Euros for a single event (cf. Andreas hailstorm on 28 July 2013 over the Southern part of Germany), hail constitutes a considerable interest for the insurance industry. Improved knowledge about hail frequency, intensity, and additional hailstorm characteristics will help to understand the potential related risks better. Even if continuous hail observations are in existence, different hail proxies are available from which the presence of hail on the ground can be estimated using different methods, although some limitations remain:

- Insurance loss data provide information about large hail occurrence on the ground but are often restricted to a few insurance companies that differentiate between hail and storm, and data are restricted to settled (insured) regions, whereas unsettled areas are not considered.

- Hail reports archived by the European Severe Weather Database (ESWD) operated by the European Severe Storms Laboratory (ESSL; Dotzek et al., 2009): datasets comprise valuable information, such as date, time, geolocalisation, maximum, and the mean diameter of hailstones. These are based on eyewitness reports, storm chasers, newspapers, and other similar sources of data. The quality and reliability of the data is very heterogeneous with most of the reports available after 2005. Furthermore, most of the reports are restricted to Germany (23.4%), and only a few hail reports are available for France.

- Severe convective storm signals, including overshooting tops (OT) and cold arc clouds, can be detected by satellites, such as Meteosat Second Generation (MSC), with a sufficient spatial resolution. Even if these signals serve as proxies for severe convection (Bedka, 2011), the relation to hail, in particular on the ground, is unclear and leads to increased uncertainty in the analysis (Punge et al., 2014).

- For precipitation radars with large areas of high spatial resolution under constant surveillance, radar reflectivity may serve as a proxy for hail. Several algorithms, based on reflectivity composites, exist that estimate hail signals from reflectivity, sometimes in combination with other data, such as satellite or radiosonde data. Furthermore, tracking algorithms follows convective structures in time and space to reconstruct entire hail swaths (Hohl et al., 2002; Kunz and Puskeiler, 2010; Puskeiler, 2013; Puskeiler et al., 2016).

- Even if numerical models are not able to reliably reproduce hail events (e.g., Noppel et al., 2010), they are able to simulate temperature, moisture, and wind at different levels of the atmosphere from which the hail potential can be estimated. Based on different methods, such as the use of a specific logistic regression model developed by Mohr (2013), hail climatology can be estimated for larger regions. An advantage of model data is its long-term availability (30-50 years) and large spatial coverage.

- Lightning datasets are available for several years over large areas with a high accuracy. Even if hail is directly connected to thunderstorms, a systematic relationship between lightning data and hail cannot be established.

The present work is carried out within the framework of the project HAMLET (Hail Model for Europe by Tokio Millennium) funded by the reinsurance company Tokio Millennium Re based in Zürich, Switzerland. Started in January 2013, the project focuses on the analysis of past severe hail events over six European countries and aims to create a stochastic hail event set based on the latest scientific developments. This stochastic event set forms the basis to quantify hail risk and to estimate probable maximum loss (e.g., PML200) for a given industry motor or property (building) portfolio. The results help identify regions frequently affected by hail. Statistics of hail events give further insights into the mechanisms driving the onset of deep moist convection.

In this study, daily maximum reflectivity composites obtained from the combination and merging of single radar locations with additional lightning data form the basis for proper detection of individual hail events over Europe. The total investigation period covers the years from 2005 through 2014 during

which time radar data for the four European countries are available. Convective signals from radar data were tracked by applying an appropriate algorithm. Hail signals were estimated from the tracks using the simple Mason (1971) criterion that estimates hail corresponding to a radar reflectivity more than 55 dBZ. To further improve the reliability of the results obtained from this analysis, additional methods were developed to correct radar data, including an advection correction, which interpolates reflectivity values between the single MaxCAPPIs (Maximum Constant Altitude Plan Position Indicator) along hail tracks. The spatial and temporal variability of the hail events is discussed with respect to continentality, general climatic conditions, and orographically-induced flow modifications that may trigger deep moist convection. A new Radar Convective Severity Index (RCSI), based on the hail kinetic energy, was computed to estimate and compare the severity of hailstorms. Air mass properties during severe hail events were investigated to identify typical weather patterns relevant to the development of deep convection.

The most important scientific questions discussed in this thesis are:

- How are the spatial and temporal hail potentials distributed over Western Europe?
- Which dimensions and characteristics have severe hail swaths? What are the main daily and seasonal cycles and how do they depend on the specific locations?
- What are the relationships between hail frequency and orographic characteristics?
- What are the prevailing pre-convective conditions that favor the development of severe hailstorms? Which meteorological parameters best describe the occurrence of hail events?

Fundamentals of deep moist convection leading to the formation of hail within convective systems are first explained in Chapter 2 followed by an overview of weather radar principles. Chapter 3 presents the data and methods used for this study. The cell-tracking algorithm, leading to the reconstruction of past hail swaths, is described in detail together with the new RCSI derived from individual hail swaths. Chapter 4 describes the spatiotemporal variability of hail signals obtained from radar data and presents statistical analyses of hail swaths as well as their respective RCSI. Furthermore, how the estimated hail days depend on additional factors, such as orography, continentality, or local climate is investigated. The chapter concludes with a regional analysis of hailstorm occurrences. Chapter 5 assesses environments favoring hail on a large scale using reanalysis data and shows several properties of the 100 most severe hail swaths that occurred during the investigation period.

2. Theoretical concepts

Hail is formed within deep cumulus clouds that usually extend through the entire troposphere. These types of clouds develop in a convective environment where buoyancy forces arising from thermal instability drives the vertical motion. This chapter discusses theoretical fundamentals and physical concepts related to deep convection including triggering mechanisms by orographically-induced lifting. The first part focuses on the thermodynamic aspects of convection. Section 2.2 briefly overviews the different types of convective storm systems and their properties. Thunderstorms produce lightning as defined in Section 2.3. Section 2.4 discusses cloud microphysics related to the growth of hailstones. Hail observation systems available in Europe are described in Section 2.5, and Section 2.6 overviews radar basics, including hail detection approaches and radar errors.

2.1. Deep moist convection

Large hail can be produced in organized convective storms. These storms develop in an environment where the air is lifted to saturation producing positive buoyancy (Markowski and Richardson, 2010) such that the air parcel may rise to greater heights. This process is referred to as deep moist convection (DMC), and the following section discusses parcel instability leading to DMC.

2.1.1. Convection

Convection induces a vertical rise of heat associated with buoyancy within an unstable atmosphere and can be classified as free or forced convection. Free convection occurs because of temperature differences between an air parcel and the environment. Therefore, this type of convection preferably occurs during the summertime, especially throughout the afternoon, when the Earth's surface absorbs a higher amount of solar radiation. As the surface warms up during the day, the overlying air layer is also heated, which gradually becomes less dense than the surrounding air and, thus, begins to rise. The other possibility for reaching an unstable layer at low levels to enable free convection is cooling aloft by, for example, cold air advection.
In a forced convection environment, the lifting of air is caused by obstacles, such as an orographic lift or cold fronts where the warm air is forced to lift above colder air (AMS, 2000).

2.1.2. Thermodynamic fundamentals

Water is an essential constituent of the atmosphere and is the only substance available in the atmosphere as three phases: solid in the form of ice and snow, liquid as rain and cloud droplets, and gaseous water vapor. Depending on the atmospheric energy budget, the water content in the troposphere varies between 0.0% and 4%. Evaporation and condensation within the water cycle are important processes for the energy balance.
The equation of state for dry air (a mixture of ideal gases) by considering Dalton's law is

$$p_d = \rho_d R_d T \tag{2.1}$$

Equation (2.1) expresses the relationship between the pressure (p_d), the density (ρ_d), and the temperature (T) of atmospheric gases with R_d as the specific gas constant for dry air (R_d = 287.05 J kg^{-1} K^{-1}). For moist air, the total pressure is expressed as $p = p_d + p_m$, where $p_m \equiv e$ is the water vapor partial pressure. Combining the equations of state for dry and moist air yields:

$$p = (\rho_d R_d + \rho_m R_m) T \tag{2.2}$$

Adding the mixing ratio and the water vapor partial pressure gives:

$$p = \rho_d R_d (1 + \frac{r}{e}) T \tag{2.3}$$

The density ρ of the overall parcel can be deduced and added to equation (2.3):

$$p = \frac{\rho}{1+r} R_d (1 + \frac{r}{e}) T \tag{2.4}$$

As in equation (2.1), the pressure is related to density, temperature, and dry air giving the equation of state for moist air:

$$p = \rho R_d \left(\frac{1 + r/e}{1 + r} \right) T \tag{2.5}$$

or,

$$p = \rho R_d T_v \tag{2.6}$$

where T_v is the virtual temperature. The virtual temperature of a moist air parcel is the same temperature that a dry air parcel would have at equal density and pressure of the moist parcel.
The first law of thermodynamics defines the quantification of energy exchanges between an air parcel and its environment:

$$du = \delta q + \delta a \tag{2.7}$$

The variation of internal energy du is due to specific heat δq variations transferred from or out of the volume, and to work δa variations. For a compressible air volume, the latter can be expressed by:

$$\delta a = -pd\alpha \quad [2.8]$$

where $\alpha = \frac{1}{\rho}$ represents the specific volume. The rate of heat exchange δq and the rate of work δa are partial differentials and are therefore written with a δ instead of a d.

Internal energy changes are proportional to the temperature changes, $du = c_v dT$, with c_v as the specific heat capacity of a constant volume of air (c_v = 719 J kg^{-1} K^{-1}). With the enthalpy $h = u + p\alpha$, equation (2.7) can be written:

$$\delta q = dh - \alpha dp \quad [2.9]$$

The change of enthalpy is $dh = c_p dT$, where c_p = 1005 J kg^{-1} K^{-1} is the specific heat at constant pressure. For an adiabatic process that neglects heat transfer between an air parcel and its environment, $\delta q = 0$, and equation (2.9) becomes:

$$dh = c_p dT = \alpha dp \quad [2.10]$$

According to equation (2.10), a pressure variation causes a change in the temperature (assuming adiabatic processes). The hydrostatic approximation, resulting from the neglect of vertical acceleration where z is the altitude and g the gravitational acceleration, is given by:

$$\frac{\partial p}{\partial z} = -\rho g \quad [2.11]$$

With this expression, equation (2.10) becomes $c_p dT = -gdz$, thus yielding a dry adiabatic temperature gradient Γ_d representing the rate at which temperature decreases with the height for a non-saturated air parcel.

$$\frac{\partial T}{\partial z} = -\Gamma_d = -\frac{g}{c_p} = -0.0098 \text{ K m}^{-1} \quad [2.12]$$

Combining equations (2.6) and (2.10) yields Poisson's law:

$$c_p dT = R_d T d\ln p \quad [2.13]$$

Integration gives:

$$T_0 \equiv \theta = T \left(\frac{p_0}{p} \right)^{\frac{R_d}{c_p}} \quad [2.14]$$

θ is the potential temperature an unsaturated parcel of dry air would have if brought adiabatically and reversibly from its initial state to a reference pressure p_0, which is usually p_0 = 1000 hPa. θ remains constant for adiabatic vertical motions and represents the potential energy, which is proportional to the entropy. The potential temperature is conserved for dry adiabatic processes and is an important quantity to describe the stratification of an unsaturated troposphere.

In the same way, the equivalent potential temperature for moist-adiabatic conditions is defined.

When an unsaturated air parcel is lifted, the air expands and cools down and dries adiabatically. When the air is saturated, latent heat is released, which reduces the cooling of the air parcel compared to the dry adiabatic process.

When condensation is considered in equation (2.10), it yields:

$$dh = c_p dT + l_v dr_s = \alpha dp \qquad [2.15]$$

where l_v represents the evaporation rate with r_s as the saturation mixing ratio.

Thus, the change in enthalpy by lifting compared to the dry case is increased by the amount of latent heat ($l_v dr_s$).

By integrating equation (2.16), the equation of equivalent potential temperature becomes:

$$\theta_e \approx \theta \cdot e^{\left(\frac{r_s l_v}{c_p T}\right)} \qquad [2.16]$$

θ_e is the temperature a parcel of air would have if the entire water vapor were condensed, releasing latent heat and brought adiabatically to 1000 hPa. The parameter l_v represents the latent heat of evaporation. This equation is only an approximation. Bolton (1980) provided a relatively exact equation of θ_e by:

$$\theta_e = T\left(\frac{p_0}{p}\right)^{0.2854(1-0.28r)} \cdot \exp\left[r(1+0.81r)\cdot\left(\frac{3376}{T_{LCL}} - 2.54\right)\right] \qquad [2.17]$$

with T_{LCL} as the temperature at the condensation level by lifting. The dependence of c_p on the mixing ratio r is explicitly considered in this equation. The right exponential term of equation (2.17) considers latent energy due to phase transitions. For very dry conditions, for example at higher elevations, θ_e and θ are almost equal.

The moist adiabatic lapse rate Γ_m cannot be determined as easily as the dry adiabatic lapse rate because Γ_m depends on moisture content and the pressure of the air parcel.

$$-\frac{\partial T}{\partial z} = \Gamma_m = \frac{g}{c_{pl} + rc_w} + \frac{1}{c_{pl} + rc_w}\frac{l_v dr_s}{dz} \qquad [2.18]$$

where c_w and c_{pl} are heat capacities of liquid water and water vapor respectively. Further details can be found in Durran and Klemp (1982).

Moist adiabatic and dry lapse rates compared to the environmental lapse rate (γ) define an air stability that characterizes how air parcels react to an initial vertical rise initiated by external forces. When an air parcel is forced to return to its original position, the environment is stable. The rate of change of θ_e with height identifies stable and unstable conditions. If θ_e decreases with height (z),

$$\frac{\partial \theta_e}{\partial z} < 0 \qquad [2.19]$$

such that the atmosphere is unstably stratified and convection may occur. In contrast, when θ_e increases with height,

$$\frac{\partial \theta_e}{\partial z} > 0 \qquad [2.20]$$

such that stability is reached. According to Haurwitz (1941), four atmospheric states can be distinguished. For this purpose, the environmental lapse rate γ is compared to moist and dry lapse rates, respectively:

- Absolute stability: $\gamma < \Gamma_m$.

  When an external force induces a vertical air displacement from its initial position, the air parcel will return to this position. This is because the lifted air becomes colder than its surrounding leading to descent and re-establishing an equilibrium state.

- Absolute instability: $\gamma > \Gamma_d$.

  When the dry adiabatic lapse rate is lower than its environmental lapse rate, a lifted air parcel is warmer and less dense than its surroundings and will rise further due to positive buoyancy.

- Neutral condition: $\gamma = \Gamma_d$ or $\gamma = \Gamma_s$.

  When the environmental lapse rate is equal to the moist or dry adiabatic lapse rate, the height of an air parcel remains constant. Under such conditions, an air parcel displaced vertically experiences no buoyant acceleration and remains at the lifted position.

- Conditional instability: $\Gamma_d > \gamma > \Gamma_s$.

  If the environmental temperature gradient is between the dry and moist adiabatic gradient, then the layering is conditionally unstable. An air parcel rises further when becoming saturated during such conditions.

If an air parcel is too dry, then positive buoyancy does not permit the parcel to reach the level of free convection (LFC; see next paragraph) despite a conditionally unstable stratification. In contrast, an air parcel rising with high moisture contents from lower heights permits attaining the level of free convection (LFC). The air parcel temperature is then higher than its surrounding, and positive buoyancy is present, a state referred to as latent instability (Normand, 1938).
Potential instability exists if equivalent potential temperature θ_e decreases with height. Furthermore, if a moist layer is present under a dry layer and if the column of air is lifted (for example, when a cold front crosses), then condensation occurs earlier into the lower moist layer than the layer above in which air is lifted dry adiabatically over a larger distance. This increases the vertical temperature gradient as the upper layer cools faster than the lower and, thus, promotes instability. Such a configuration is referred to as potential instability.
According to Groenemeijer (2009), latent instability is the most important prerequisite for DMC development and severe thunderstorms.

2.1.3. Vertical motions

The lifted parcel theory describes vertical movements and associated changes of state (Holton, 2004) where an air parcel does not exchange any kind of matter and heat with the environment (adiabatic conditions). Further, the parcel has the same pressure as the environment. The lifting of an air parcel is initially dry adiabatic until saturation. After this level, the lifting is pseudo-adiabatic. During the ascent, all condensed water instantaneously falls out. Furthermore, freezing processes are neglected. These assumptions strongly approximate reality and are necessary for stability quantifications. However, a rising air parcel interacts with the environment leading to entrainment. Heymsfield et al. (1978) show that the rise of the central part of a cumulus nimbus cloud approximately follows saturated adiabatic conditions, and applies both to changes in temperature as well as in water vapor content. During dry adiabatic lifting, phase changes do not occur with the consequence that dry adiabatic processes are reversible. In contrast, during pseudo-adiabatic lifting, all condensation products are assumed to fall out of the parcel immediately after they have formed. Therefore, this process is strictly irreversible. The prefix "pseudo" is used because the falling precipitation carries energy away from the parcel, which transgresses the definition of a strictly adiabatic process.
During its rise through the troposphere, an air parcel follows different stages:

- In the first stage, an air parcel is lifted dry-adiabatically up to a certain height until saturation is reached. Possible causes for the uplift can be of both dynamic (fronts, orography) or thermal in nature (warming of layers near the ground). In the first case, the saturation level defines the lifting condensation level (LCL). In the second case, the level is referred to as the cumulus condensation level (CCL). During the unsaturated ascent, the potential temperature θ and mixing ratio are constant.

- After saturation occurs, the air parcel rises further pseudo-adiabatically. During this phase, latent heat of condensation is released leading to reduced cooling compared to a pure dry adiabatic process. Because the heat released by condensation partially offsets the cooling due to expansion, the parcel cools at a lesser (moist adiabatic) rate as it rises.

- The height at which the air parcel temperature exceeds that of the environment is the level of free convection (LFC). Above this level, the air parcel is vertically accelerated from the LFC because of its higher temperature leading to positive buoyancy.

- After crossing the LFC, the air parcel rises along the moist adiabat until its temperature becomes lower than the ambient temperature. The level at which the air parcel temperature is equal to the environment is called the equilibrium level (EL). For deep convection, EL is usually identical to the cloud top. Due to a strong inertia of the air parcel, the part of updraft with an important momentum may penetrate the lower stratosphere and form an overshooting top (OT) (Bedka, 2011; Punge

et al., 2014). An OT is the product of deep convective storm updraft cores of sufficient strength to rise above the storm's general equilibrium level near the tropopause region.

The buoyancy B represents a vertical pressure gradient force not balanced with gravity resulting from density differences between an air parcel and its surrounding. Positive buoyancy is defined as a statically forced part of the local non-hydrostatic upward pressure gradient (Doswell III and Markowski, 2004; Markowski and Richardson, 2010). Buoyancy results from the vertical component of the equation of motion. Neglecting frictions and the earth's rotation, this is given by:

$$\rho \frac{dw}{dt} = -\frac{\partial p}{\partial z} - \rho g \tag{2.21}$$

A horizontally homogeneous hydrostatic balance (base state, denoted by an overbar) is defined by:

$$\frac{\partial \overline{p}}{\partial z} - \overline{\rho} g = 0 \tag{2.22}$$

Then, pressure and density are decomposed into a hydrostatic basic state and a perturbation from that base state, denoted by ($'$), is:

$$\begin{aligned} p &= \overline{p}(z) + p' \\ \rho &= \overline{\rho}(z) + \rho' \end{aligned} \tag{2.23}$$

Consequently, using the previous notations and equation (2.21) Doswell III and Markowski (2004) gives:

$$\rho \frac{dw}{dt} = -\left(\frac{\partial \bar{p}}{\partial z} + \frac{\partial p'}{\partial z} \right) - \left(\bar{\rho} + \rho' \right) g \tag{2.24}$$

Subtracting (2.22) from (2.24) and rearranging yields:

$$\frac{dw}{dt} = \underbrace{-\frac{1}{\rho}\frac{\partial p'}{\partial z}}_{i} \underbrace{- \frac{\rho'}{\rho} g}_{ii} = -\frac{1}{\rho}\frac{\partial \rho'}{\partial z} + B \tag{2.25}$$

where i represents the vertical gradient of pressure perturbation and ii is the buoyancy term (Kessler, 1985).

Replacing ρ with $\overline{\rho}$ gives:

$$B = \frac{\rho'}{\overline{\rho}} g \approx \left(\frac{T_v'}{\overline{T_v}} - \frac{p'}{\overline{p}} \right) g \tag{2.26}$$

Integrating the positive buoyancy B from the LFC to EL yields the convective available potential energy (CAPE).

$$CAPE = \int_{LFC}^{EL} B dz \approx R_d \int_{LFC}^{EL} (T_v' - T_v) d\ln p \tag{2.27}$$

CAPE represents the maximum energy available during the ascendancy of an air parcel during convection. When the air parcel reaches the EL, B becomes negative and can no longer be lifted. According to Doswell III and Rasmussen (1994), ρ_m needs to be considered in the definition of CAPE. The authors

also indicate that the virtual temperatures of the air parcel T_v' and the environment T_v are physically required as well in its definition. As $T_v > T$, the values of CAPE by considering moist air are always larger than without.

When an air parcel has positive buoyancy, CAPE values are larger than zero (Moncrieff and Miller, 1976). Higher values of CAPE represent high potential for severe storms.

Table 2.1 shows typical values of CAPE in Southern Germany identified by Kunz (2007a).

Tab. 2.1.: Typical CAPE values in terms of convection severity (Kunz, 2007a).

< 500 J kg $^{-1}$	weak convective activity
500 - 1000 J kg $^{-1}$	moderate convective activity
> 1000 J kg $^{-1}$	deep convective activity

CAPE also defines the maximum thermodynamic vertical velocity. Thus, the vertical component of the equation of motion (2.21) without pressure anomalies is:

$$\frac{dw}{dt} = \frac{-\rho}{\rho} g = B \qquad [2.28]$$

Multiplied by the vertical velocity gives:

$$w\frac{dw}{dt} = B\frac{dz}{dt} \qquad [2.29]$$

and integrated over the time needed by an air parcel to rise:

$$\frac{1}{2} dw^2 = Bdz \qquad [2.30]$$

Integration of the velocity between LFC (w = 0) and EL (w = max) yields

$$\int_{LFC}^{EL} dw^2 = {w^2}_{max} = 2\int_{LFC}^{EL} Bdz = 2 \cdot CAPE \qquad [2.31]$$

or

$$w_{max} = \sqrt{2 \cdot CAPE} \qquad [2.32]$$

According to Weisman and Klemp (1984), the ratio S between the actual and the buoyancy-derived maximum velocity is defined to be equal to $\frac{w}{w_{max}}$ and varies between 0.3 and 0.6. Reasons for S < 1 include the neglect of entrainment from the environment and vertical mixing.

In the same way as for the CAPE, another convective parameter can be considered denoted as convective inhibition (CIN).

$$CIN = -\int_{h_0}^{LFC} Bdz = -R_d \int_{h_0}^{LFC} (T_v' - T_v) dlnp \qquad [2.33]$$

This quantity indicates the amount of energy that is required to lift a parcel of air from the surface h_0 to the LFC. This amount of energy is required to overcome the negative buoyant energy the environment usually exerts on an air parcel.

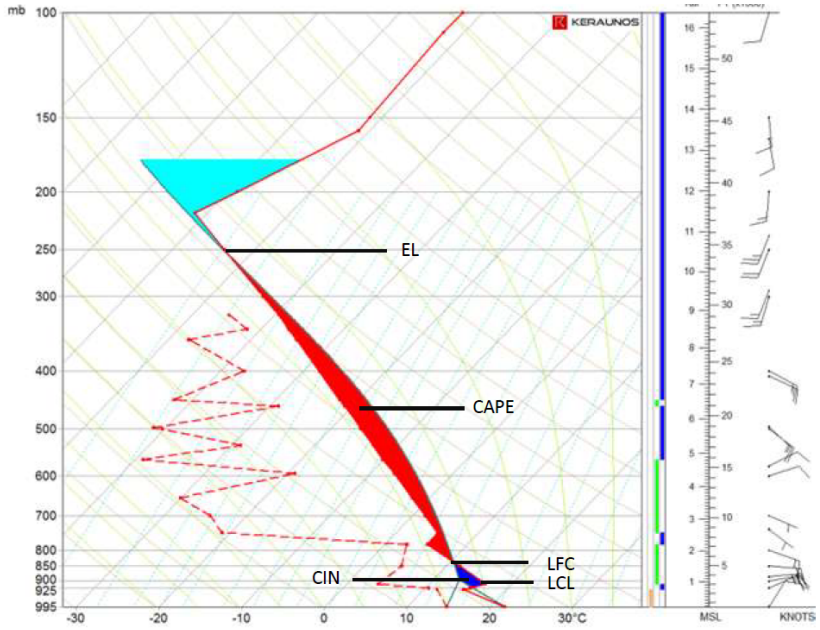

Fig. 2.1.: Skew-T log p diagram from a radiosonde in Trappes, France. Horizontal solid black lines, spaced logarithmically, represent isobars. Black solid lines sloping from the lower left to upper right with equal spacing are isotherms. Black curved solid lines sloping from the upper left to lower right are dry adiabats or lines for constant potential temperature. These indicate the rate of temperature change in a parcel of dry air moving adiabatically. Moist adiabats are the slightly curved light green solid lines sloping from the upper left to lower right. Moist adiabats represent the temperature change from a saturated parcel of air rising pseudo-adiabatically. Dark green dotted curves represent a constant saturation mixing ratio. The bright blue curve represents the parcel's trajectory, and the red curve is the measured temperature. The red area depicts the CAPE, whereas the light blue area represents the CIN. The red dotted curve indicates the measured dew point. Modified from Wesolek and Mahieu (2011).

A powerful diagram to visualize thermodynamic processes in the atmosphere is the so-called skew T-log p diagram, which represents the temperature T on the x-axis and the logarithm of the pressure p on the y-axis. The advantage of this diagram provides a better visualization of convection. Due to the logarithms of p, the area between the lifted parcel and the temperature profile of the surrounding are proportional to the CAPE. Both the CAPE and CIN can be easily visualized and quantified on a skew T-log p diagram. They are represented by the area between the environmental temperature and air parcel temperature curves (Figure 2.1).

2.1.4. Triggering of Convection

Stull (1994) defines the atmospheric boundary layer (ABL) as the part of the troposphere directly influenced by the Earth's surface that responds to surface forcing with time scales of about an hour or less. Solar heating of the surface causes thermals to rise and, thus, triggers convection with the transport of moisture, heat, and aerosols. The air parcel rises and expands adiabatically until thermodynamic equi-

librium is reached at the top of the ABL. If the air parcel rises near orography, forced convection can be initiated. Indeed, orography and rough terrain play a major role in the onset of convection (Stull, 1994; Smith, 1989) by the deviation of near-surface flows or by thermally-induced wind systems. Houze (1993) distinguishes between two main processes related to dynamic or thermal effects within the atmosphere.

Dynamic orographic flows

Dynamic flow effects are determined by the shape (height and width), orientation, and the obstacle's slopes in combination with airmass characteristics. Internal gravity waves are generated when the flow passes over or around a mountain range within a stably stratified troposphere. The frequency of these waves is used to determine air stratification. Gravity waves propagate horizontally but also vertically and can be thus relevant for mesoscale motions. Static stability of the troposphere can be assessed by the Brunt-Väisalä frequency N with

$$N = \sqrt{\frac{g}{\theta_v}\frac{\partial \overline{\theta_v}}{\partial z}} \qquad [2.34]$$

where $\frac{\partial \overline{\theta_v}}{\partial z}$ is the vertical gradient of the virtual potential temperature. With equation (2.29) and the linear form of the adiabatic equation, the following can be written:

$$\frac{dB}{dt} + N^2 w = 0 \qquad [2.35]$$

or

$$\frac{d^2 w}{dt^2} + N^2 w = 0 \qquad [2.36]$$

where the vertical motion w is dependent of the Brunt-Väisalä frequency. The initial conditions for small vertical motions with neglect of acceleration at $t = 0$, are $w(t = 0) = w_0$ and $\frac{dw}{dt}t^2 = 0$

Three possible solutions are available for equation (2.36) depending on the sign of N:

- for $N^2 < 0$: $w(t) = w_0 \cos h\,(|N|t)$: the atmosphere is unstable and w increases with time.
- for $N^2 = 0$: $w(t) = w_0$: neutral stratification; the air parcel continues to move away from the initial position with constant velocity $w = w_0$ (without acceleration).
- for $N^2 > 0$: for $w(t) = w_0 \cos(Nt)$: a harmonic oscillation of the vertical velocity with frequency N. The air volume oscillates about the reference level when the atmosphere is stable (Stull, 1994).

The Froude number is an important parameter from similarity theory to distinguish different flow regimes. The ratio of inertial to buoyancy forces or, rather, the ratio of the flow inertia to the external field is the dimensionless Froude number $F_r = \frac{U}{NH}$, where U represents the flow speed, and H is the height of the obstacle.

$Fr \gg 1$: high wind speed and/or low stability and/or small mountains, and the flow goes directly over

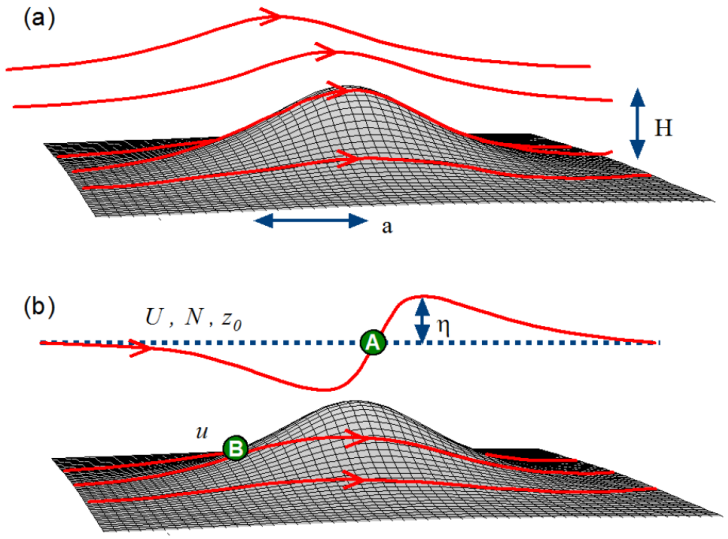

Fig. 2.2.: Flow over a mountain at high (a) and low values of the Froude number (b). Stagnation points are formed aloft the mountain (A) and upstream close to the ground on the windward side (B) described by Smith (1989) and modified by Kunz (2011).

the mountain (Case a in Figure 2.2).

$Fr < 1$: weak wind speed and/or high static stability and/or high mountains, and the flow may go around the obstacle.

During the flow-around regime, a stagnation point may form upstream (Figure 2.2, point B). Such a stagnation point is a local blocking of the flow (Smith, 1989). The flow is then divided and passes alongside the obstacle. The blocking point on the ground can initiate a dividing streamline at upper levels. This streamline separates a stable flow approaching an obstacle into two flows: a lower region, where the flow is horizontal and splits around the obstacle (i.e., the flow is partially blocked), and an upper region, where the flow is three-dimensional and goes over the hill (Snyder et al., 1985). The generated waves can have some effects over a local-scale, mesoscale, and partially large-scale:

Through the formation of waves, another blocking point can form on the leeward side of the mountain (Figure 2.2, point A), which can initiate wave breaking. This wave breaking has a significant influence on the leeward side flow with, for example, the generation of turbulent flows (Lane and Clark, 2000) that enhance downslope winds (Peltier and Clark, 1979). The large amplified baroclinic wave behind a large mountain may develop a trough leading to cyclogenesis at the leeward side (Smith, 1989).

The vertical propagation of the momentum generated by the internal gravity waves can affect the mesoscale. The associated vertical mixing of water vapor, aerosols, and chemical particles (Dörnbrack and Dürbeck, 1998) can modify the atmospheric energy budget as well as large-scale circulations. However, the effect of mountain-waves is more important for mesoscale systems than large-scale circulation because the energy generated by waves is partially absorbed in the troposphere, which reduces the transmission to higher altitudes. For a theoretical description, air flowing in an incompressible atmosphere in

a two dimensional x,z plane is assumed. The motion and adiabatic equations are linearized, neglecting the Coriolis force. According to Holton (2004), the disturbance of the vertical speed w' is given by:

$$\left(\frac{\partial^2 w'}{\partial x^2}+\frac{\partial^2 w'}{\partial z^2}\right)+\frac{N^2}{U^2}w'=0 \qquad [2.37]$$

with the vertical wave number m:

$$m^2=\frac{N^2}{U^2-k^2} \qquad [2.38]$$

where k represents the wave number of the x plane.

Two solutions are possible for $m^2 \neq 0$:

$$w'=\begin{cases} \text{for m}^2>0: w'=\hat{w}\ \exp[i(kz+mz)] \\ \text{for m}^2<0: w'=\hat{w}\ \exp ikx\ \cdot\exp[-m_i z] \end{cases} \qquad [2.39]$$

with amplitude $\hat{w}$ and imaginary vertical wave number m_i. By $m^2>0$, an undampened wave propagation occurs horizontally as well as vertically (free waves). The solution $m^2<0$ is carried out for $|Uk|<N$ and yields dampened vertical waves (Holton, 2004).

Etling (2008) defines the induced topographic stationary wave by:

$$L=\frac{2\pi\cdot U}{N} \qquad [2.40]$$

These leeward waves are visible, for example, in the form of clouds of the genus Altocumulus lenticularis (Aclen) when vapor condenses by adiabatic cooling in the ascending branch of the wave movement.

Using a 2D model, Chu and Lin (2000) identified different regimes with a potentially unstable flow over the mountain. For very small Froude numbers, convective cells are triggered on the windward side

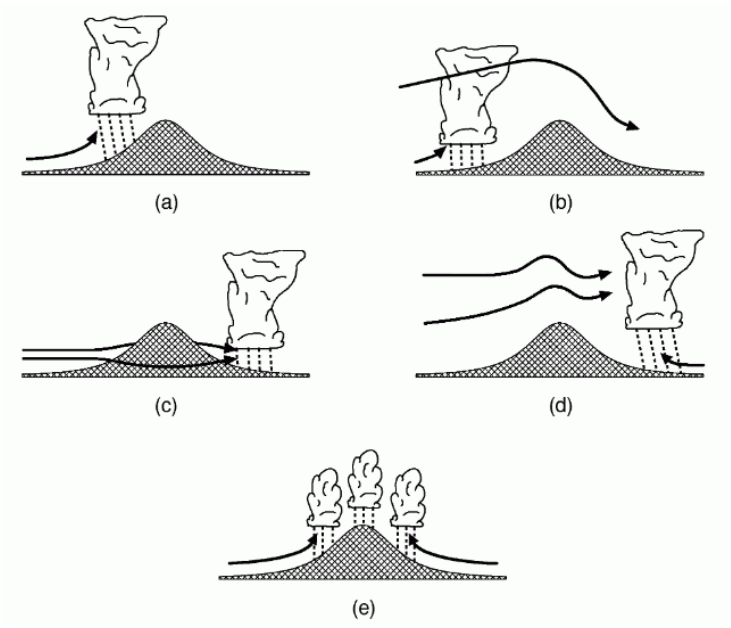

Fig. 2.3.: Triggering of convection depending on the flow regimes. From Houze (1993), modified by Kunz (2003).

of the mountain because of deceleration and the resulting uplift (Figure 2.3). In such a regime, the initiation of convection is situated further upstream because of gravity waves forming aloft. Convective cells can also form downstream with the development of flow convergence on the leeward side (Durran and Klemp, 1987, Pierrehumbert and Wyman, 1985). In subsequent work, Chen and Liu (2005) used a 3D model configuration to study flow effects evolving over an isolated mountain. Qualitatively, the results agree with the 2D simulations where the flow around regime appears because of flow convergence developed on the leeward side. The associated frequent development of convective cells on the leeward side was also shown by Kunz and Puskeiler (2010) and Puskeiler (2013) where a maximum of hailstorms occurred during southwesterly flow downstream of the Black Forest mountains in Germany.

Thermal orographic flows

Convergence resulting from thermal flows may influence the triggering of deep convection at a regional or local scale, such as near mountain crests (e.g., Cotton et al., 1983; Banta, 1990; Banta and Barker Schaaf, 1987). Moreover, Banta (1990) speculated that convergence can be initiated at a larger scale (for example, an entire mountain range). Thermally-driven flows occur at multiple scales, such as an entire mountain, in single valleys or on single slopes (Wagner, 1932). At meso-alpha scale, 200 - 2000 km (Orlanski et al., 1985), large-scale circulation occurs between adjacent plains and elevated terrain (Tang and Reiter, 1984). At the scale 20 - 200 km (meso-beta), thermally plain mountain flows originating from differential heating and leading to pressure gradients (Egger, 1990), were observed, for example, in the Alps (Weisman et al., 1988; Lugauer and Winkler, 2005, Haiden, T., Kann, A ., Wittmann, C ., Pistotnik, G., Bica, B ., and Gruber, C., 2011). At smaller scales, for example, in a single valley (2 - 20 km; meso-gamma) differential heating led to local wind systems. During the day, the same amount of energy is provided to a plain as well as a valley atmosphere. As the volume of air in a valley is confined, the heating of the air is more important in a valley compared to larger scales over the plain (Steinacker, 1984; Whiteman and Doran, 1993).

The diurnal cycle of temperature and solar heating influences the along-valley wind. Observations during summertime over the Alps show that the upvalley wind is established in the morning (Langhans et al., 2013) and can amplify until 1300 UTC before returning to the valley (Langhans et al., 2013). Defant (1951) described the diurnal cycle of wind systems in valleys as the following. The sunrise triggers the first upslope winds, initiated by the heating of the side wall exposed to the sun. During the morning, pressure gradients are intensified between the valley and the mountain crest leading to slope wind (Langhans et al., 2013). In the early afternoon, the intensity of the slope wind decreases, and a mean wind flow develops in the valley. As the mountain crest is warmer during the evening, downwind flow is initiated and blows from the mountain towards the valley, so that the dense air at higher elevations is carried by gravitational force. This feature persists over the night (Langhans et al., 2013) until the morning when sunrise occurs. A capping inversion appears during the night in the valley, and its strength controls the

wind velocity through the valley during the nighttime (Doran et al., 1989).

2.2. Convective weather systems

Convective weather systems can be classified according to their physical characteristics, organization, and preferred location of occurrence. There are four main types of thunderstorms: single-cells, multicells (inline or clusters) and supercells. Mesoscale convective systems (MCS) are, according to the American Meteorological Society's Glossary of Meteorology (2000), an ensemble of thunderstorms producing a contiguous precipitation area of 100 km or more in horizontal scale in at least one direction. Most MCSs can be regarded as multicellular convection because new cells are repeatedly triggered by a gust front to maintain a system of cells existing longer than individual cells.

Vertical wind shear is a predominant parameter to classify thunderstorms (Markowski and Dotzek, 2011) as it influences the lifetime and the helicity of a cloud. Most relevant for the organization of convective systems is the vertical shear of the horizontal wind between the surface and 6 km, which is quantified as the wind vector difference. Wind shear is referred to as the difference in wind speed and direction with the height (AMS, 2000). A shear above 20 m s^{-1} is considered strong and promotes the development of supercells, whereas values below 10 m s^{-1} indicate weak wind shear where single cells usually develop.

2.2.1. Single cell thunderstorms

Single-cells are non-rotating, isolated cells with diameters between 2 and 10 km, and a short lifetime of about 30 minutes to one hour. A single updraft and one downdraft characterize them. As the wind shear is mostly below 10 m s^{-1} (Markowski and Richardson, 2010), the gust front is not able to initiate new cells.

These thunderstorms evolve into three stages: cumulus, mature, and the dissipation phase. At first, a cumulus cloud forms in an unstable environment with weak shear, preferably during the daytime and early evening. During the lifting process, condensation takes place when the dew point within the air parcel is reached. The cloud shape and size increase during its ascension and an anvil shape can form at the top of the cloud. As the air parcel passes above the freezing level, precipitation starts to develop via the Bergeron-Findeisen process that describes ice crystal growth in mixed-phase clouds (containing a mixture of supercooled water and ice). The mature stage is reached when precipitation falls, triggering a cool downdraft (e.g., Knupp and Cotton, 1985; Markowski and Dotzek, 2011; Houze, 2004). When the downdraft becomes stronger than the updraft that does not provide enough heat into the system to continue to rise and develop, the dissipating stage is reached. This phase provokes the highest precipitation intensities of the entire cloud lifecycle. The cloud begins to dissolve from the base up to the top (Figure 2.4).

The collapse of the updraft by an evolving downdraft can be estimated according to Markowski and Richardson (2010) as:

$$\tau \approx \frac{H}{w_0} + \frac{H}{v_t} \qquad [2.41]$$

where τ is the cell lifetime, H is the height of the atmosphere, w_0 is the average updraft speed, and v_t represents the mean terminal fall speed of precipitation. For typical values of $H = 10$ km, $w_0 \approx 5$–10 m s^{-1}, and $v_t \approx 5$–10 m s^{-1}, τ is comprises between 30 and 60 minutes.

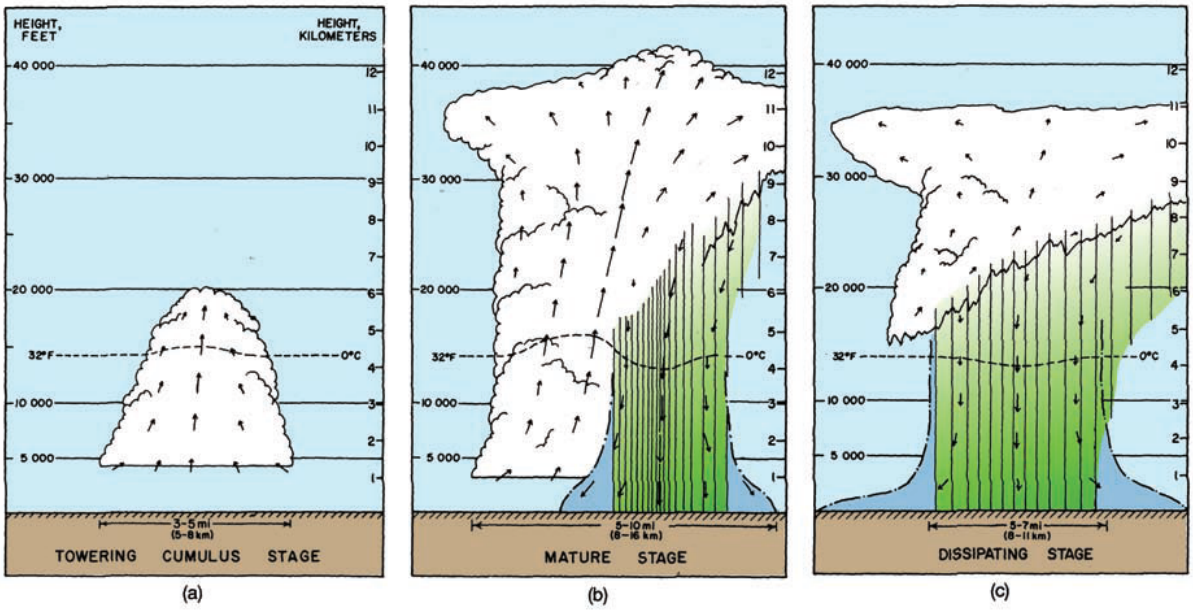

Fig. 2.4.: Three stages of a single cell: (a) towering cumulus stage, (b) mature stage, and (c) dissipating stage; adapted from Byers and Braham (1949) and Doswell (1985).

2.2.2. Multicell thunderstorms

Multicellular convection is very common in midlatitudes. In contrast to single-cells, multicells are characterized by the repeated triggering of new cells that permit the dynamic development of the system. New cells can be regarded as individual cells that persist for only 30 to 60 minutes, while severe multicells may last several hours. The movement of a multicell is usually not parallel to the mean horizontal wind but is determined of the vector sum of the horizontal wind and the vector of the new cell formation. At the ground, the interaction between vorticity related to the gust front and the wind shear (which is usually in the range 10–20 m s^{-1} according to Markowski and Richardson (2010)) allows the rising of air mass and, thus, the triggering of new cells at the location where the two vorticities interact, i.e., downshear of the cold pool. The gust front is a strong wind field on the surface that separates the boundary between the outflow of cool air (cold pool) and the surroundings with different physical properties. Towards the shear vector $\vec{S} = \frac{\partial \vec{v}}{\partial z}$, the vorticity of the gust front is opposite to that of the environment. The

uplift is increased where cold air meets warmer and moist air, which permits warm air to reach the LFC and, thus, new cells may form.

There are various stages of development of multicells (see Figure 2.5). New cells form at the flank of the cluster (cell 4 in the first section of Figure 2.5), mature cells (cell 2) are situated in the center of the storm, and dissipating cells (cell 1) associated with downdrafts are located at the rear of the storm. Each cell undergoes the lifecycle of individual single cells (e.g., cell 2 in the mature stadium in the top panel dissociates in the bottom panel). The presence of sufficient vertical wind shear is important for this development (Marwitz, 1972b), which separates updraft and downdraft.

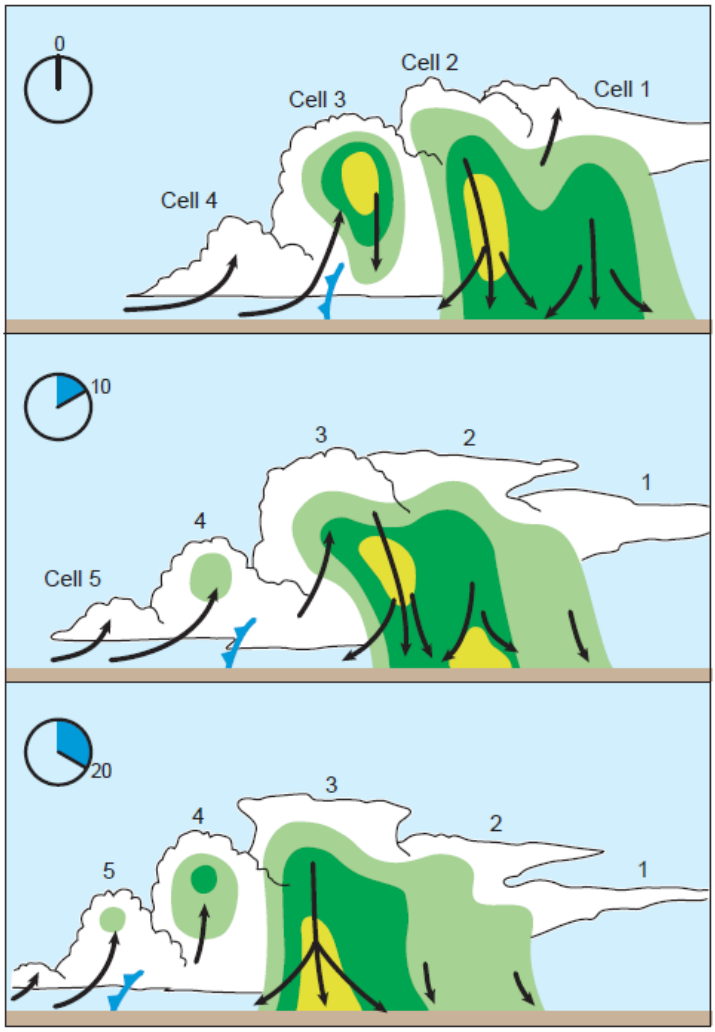

Fig. 2.5.: Vertical cross-section of a typical temporal evolution of multicellular convection. Colors represent radar reflectivity: low reflectivity values (green) evolve into high values (yellow) with updraft strength. The top panel represents a snapshot of multicellular convection. The second and third panels show the evolution after 10 and 20 minutes time-lapses. Individual cells are numbered from 1 to 5. See text for more details. Markowski and Richardson, 2010, adapted from Doswell, 1985.

2.2.3. Supercells

The most impressive kind of organized thunderstorms are supercells with the first conceptual model given by Browning and Ludlam (1962). The intense activity can cover several hours up to an entire day and produces, in almost all cases, large hail, torrential rainfalls, extreme winds, and sometimes a tornado. Approximately 20% of all supercells observed by radar in the USA led to tornado formation (Burgess, 1997). Supercells are characterized by an intense single updraft flanked by two downdrafts (Lemon and Doswell III, 1979). The first downdraft is situated at the rear of the storm, called rear-flank downdraft (RFD). The RFD forms when dry mid-level winds encounter the updraft leading to particles mixing at the backside of the updraft that evaporates producing negative buoyancy and inducing a downdraft. Another region with downdraft, generally the principal core of precipitation in a supercell is situated on the forward-flank of the updraft, called forward-flank downdraft (FFD). Evaporative cooling, melting, and sublimation of ice lead to the development of negative buoyancy triggering the FFD. A supercell has a motion that deviates significantly from the mean wind due to cyclonal (or anti-cyclonal) rotation. A typical feature of supercells is the cell splitting where a central pressure deviation forms to separate the cyclonal and anti-cyclonal cores of the updraft. After splitting, the cells propagating to the left and right sides of the mean wind are the so-called left- or right-movers, respectively. Usually, right-movers are more severe and have a longer lifetime (Wesolek and Mahieu, 2011). An essential characteristic of a supercell is the rotation of the updraft and the entire cell due to wind shear in excesses of 20 m s^{-1}. The strong rotation leads to a pressure minimum at the center (mesocyclone within the updraft) with a typical width between 3 and 8 km (Markowski and Richardson, 2010). Environmental directional shear leads to a rotating updraft as the horizontal vorticity is tilted and stretched (expanded) in the updraft as shown in Figure 2.6. By the tilting, horizontal vorticity is transferred into vertical vorticity.
(Lemon and Doswell III, 1979).

The origin of the mesocyclone can be calculated by starting with the relative vorticity equation:

$$\frac{\partial \zeta}{\partial t} = -\vec{v} \cdot \nabla \zeta + \vec{\omega} \cdot \nabla w \qquad [2.42]$$

$$\frac{\partial \zeta}{\partial t} = -u\frac{\partial \zeta}{\partial x} - v\frac{\partial \zeta}{\partial y} - w\frac{\partial \zeta}{\partial z} + \xi\frac{\partial w}{\partial x} + \nu\frac{\partial w}{\partial y} + \zeta\frac{\partial w}{\partial z} \qquad [2.43]$$

where $\omega = (\xi, \nu, \zeta)$ is the three-dimensional relative vorticity vector. The Coriolis force is neglected.

The linearized vertical vorticity equation is sufficient to describe the mesocyclogenesis. With $u = \bar{u}(z) + u'$; $v = \bar{v}(z) + v'$, $w = w'$, and $\zeta = \zeta'$ in equation (2.43) it follows that:

$$\frac{\partial \zeta'}{\partial t} = \underbrace{-\bar{u}\frac{\partial \zeta'}{\partial x} - \bar{v}\frac{\partial \zeta'}{\partial y}}_{j} + \underbrace{\frac{\partial \bar{u}}{\partial z}\frac{\partial w'}{\partial y} - \frac{\partial \bar{v}}{\partial z}\frac{\partial w'}{\partial x}}_{jj} \qquad [2.44]$$

where j is the advection term, and jj represents the tilting term. The advection term represents the advection of ζ' by the storm-relative wind. This term determines the horizontal shift of the ζ' field in the

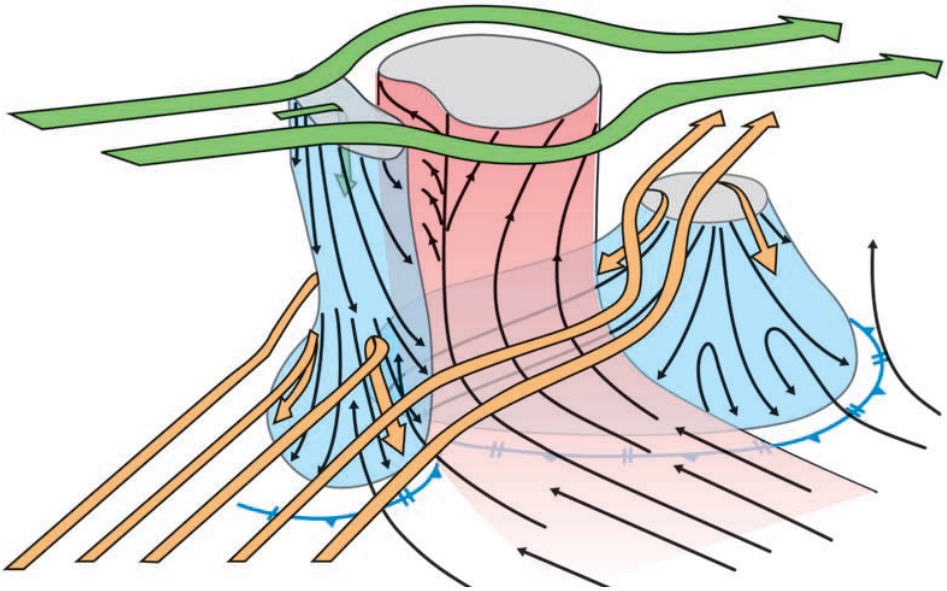

Fig. 2.6.: Three-dimensional representation of a supercell in its mature stage. Colored arrows represent the mean wind flow at 4 km (orange) and 9 km (green), and black arrows represent streamlines of inflows and of the two downdrafts. From Markowski and Richardson (2010), based on Lemon and Doswell (1979).

updraft. Note that only the tilting term can lead to an increase of ζ'. The vorticity tilted into the vertical is amplified by stretching because of conservation of angular momentum.

Davies-Jones (1984) pointed out the importance of ambient streamwise vorticity for the development of the rotating updraft. The streamwise vorticity is tilted with the conversion of horizontal to vertical vorticity. The rate at which streamwise vorticity enters the updraft of a storm can be quantified by the storm relative helicity (SRH), which is integrated over the entire layer that constitutes the inflow to the storm, often from the earth's surface to a few kilometers above ground level:

$$SRH = -\int_{z_0}^{z} \left((\vec{v}_h - \vec{c}) \cdot \vec{k} \times (\frac{\partial \vec{v}_h}{\partial z}) \right) dz \qquad [2.45]$$

with $\vec{c}$ as the storm velocity. High values of SRH, 0-3 km (> 250 m^2 s^{-2}), integrated from the lowest to 3 km layers above ground level suggest an increased potential for supercell development, since a supercell converts the SRH into its rotating updraft. Once the updraft becomes helical, the stretching of the tilted streamwise vorticity amplifies the vertical vorticity of the storm.

In a radar image, a supercell is often visible by the presence of a hook echo (reflectivity minimum) usually on the southeastern flank of the storm (Figure 2.7) due to the presence of a strong updraft. This minimum reflectivity region is called the bounded weak echo region (BWER) because the velocities are too high for precipitation formation, which leads to low reflectivity in that region.

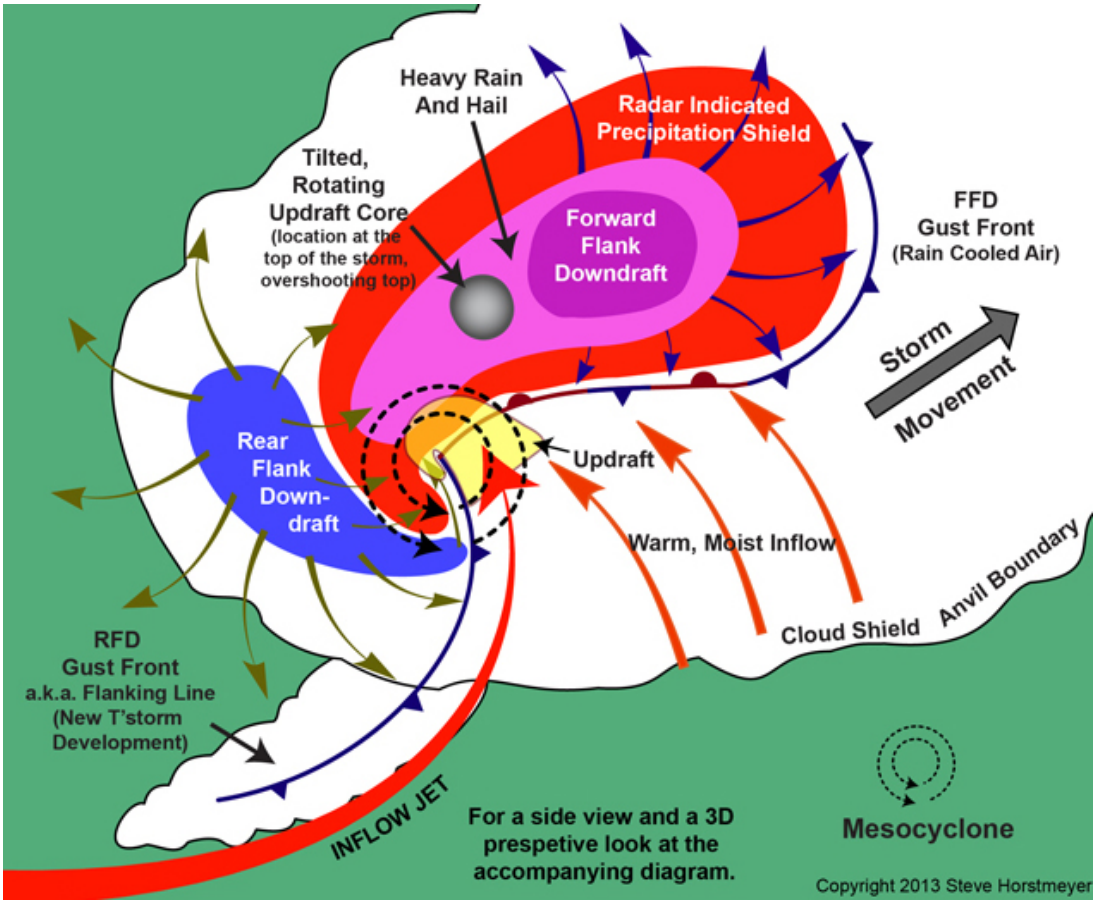

Fig. 2.7.: Horizontal cross-section of low-level radar structure and cloud features of a supercell. The red and blue colored areas represent the precipitation regions as viewed by radar with weak (red, blue), moderate (light purple), and high (dark purple) reflectivity values. The outflow boundary is indicated by the barbed contour. A few storm-relative streamlines are drawn. (Horstmeyer, 2013).

There are three types of supercells: classic (CL) supercell, high precipitation (HP) supercell, and low precipitation (LP) supercell. CL supercells have most of their precipitation on the forward flank, whereas LP supercells have rainfalls displaced at some distance away from the updraft on the forward part of the storm. HP supercells have large amounts of rain around the hook echo and on the backside of the storm (Wesolek and Mahieu, 2011). A typical radar signature of a CL is shown in Figure 2.7. The three types of supercells can be separated according to the upper-level storm-relative winds. LPs occur with strong upper-level storm-relative winds (> 28 m s $^{-1}$) with hydrometeors falling far from the updraft where they partially evaporate. When upper-level winds are weaker (< 18 m s $^{-1}$), HP can form with hydrometeors falling near the updraft and leading to large amounts of rain (Markowski and Richardson, 2010). With upper-level wind between 18 and 28 m s $^{-1}$, a CL preferably occurs (Wesolek and Mahieu, 2011).

2.2.4. Mesoscale Convective Systems

Mesoscale Convective Systems (MCS) persist during several hours (> 12 hours) and over large areas (see Table 2.2). Houze (1993) defines an MCS as a large precipitation system with embedded convection and with stratiform rainfall areas over at least 100 km. An MCS is triggered by strong and large uplift along a front or a low-pressure system (Markowski and Richardson, 2010), and controlled by large-scale lifting. They often form upstream of a trough.
Vertical velocity w is related to specific dynamic and thermodynamic conditions in the troposphere. When the quasi-geostrophic vorticity equation is related to the first law of thermodynamics, in a system where the pressure p is the vertical coordinate, the ω equation can be written as:

$$\left(\sigma\nabla^2 + f^2{}_0\frac{\partial^2}{\partial p^2}\right)\omega = -f_0\frac{\partial}{\partial p}\left(-\vec{v}_g\cdot\nabla_p(\zeta_g+f)\right) - \frac{R}{p}\nabla^2(-\vec{v}_g\cdot\nabla_p T) - \frac{R}{c_p p}\nabla^2 H \qquad [2.46]$$

σ is a stability parameter so that the left term is proportional to ω, which is the vertical velocity in the p-system. f_0 is the (constant) Coriolis parameter, $\vec{v}_g$ is the geostrophic wind, ζ_g is the relative vorticity of the geostrophic wind, and H is the diabatic heat transitions. With positive vorticity advection (PVA), which increases with height, the maximum warm advection and maximum diabatic heat transfers due to condensation causing large-scale uplift (Houze, 1993).
MCS development can be compared to the development of single cells, where convection of the system decreases with time, while the stratiform precipitation area further increases. Initially, there is a system of isolated cells that then merge and interact together. During the first stage, MCSs preferably evolve during the night from the outflows of single isolated convective cells, which are usually formed in the late afternoon (Stensrud, 1996). MCSs usually propagate along the mean wind with high velocity permitting it to move across large areas.

MCSs include two types of systems: Mesoscale Convective Complex (MCC) and Squall-lines. Like MCS, MCCs are accompanied with strong winds, heavy rain, and sometimes hail. An MCC is defined by specific characteristics observed by infrared satellite imagery according to the Maddox criteria (Maddox, 1980):

- Presence of a convective area of at least 100,000 km^2 with temperature lower than -32°C.

- Presence of a convective area of at least 50,000 km^2 for the inner (central) cloud region with a temperature lower than -52°C.

- Eccentricity (ratio of the dimensions of the major and minor axes) greater than 0.7.

- Lifetime of at least 6 h, where the criteria mentioned above prevail.

The vertical structure of an MCC can be separated into three sub-regions. Near the surface, cold air generates the outgoing thunderstorm gust front and creates a mesoscale anticyclone on the outer edge of the complex. In the mid-levels of the troposphere, a low-pressure cyclonic circulation develops where the air is warmer than outside the complex. At the tropopause, the air is cooler than the environment.

Squall-lines consist of convective cells forming a nearly linear arrangement over several hundred kilometers, often occurring in conjunction with a cold front. Squall-lines develop preferably ahead of and parallel to a cold front or dry line boundary. The width is relatively small, and less than 10 km according to Bluestein et al. (1987). Thunderstorms in squall-lines have common lifting mechanisms that include, for example, cross-circulations at fronts, large outflow boundaries, or gravity waves. Squall-lines evolve in a low-level shear environment. The low-level inflow approaching the squall line from the front is lifted to its LFC by the gust front and retains much of its front-to-rear momentum as it ascends through the leading convective updraft. After the leading updraft, the front-to-rear air sometimes descends within a transition region before ascending once again. During the mature stage, a rear-inflow jet develops at the edge of the storm in response to the upshear-tilting as horizontal buoyancy gradients are present along the rear of the storm. The rear-inflow jet supplies relatively cold and dry air from mid-levels into the system aiding in the production of a strong downdraft that may lead to a strong cold pool, which allows the system to move rapidly and affect large areas.
A bow echo is an arched outline of a squall-line (Figure 2.8) or another type of cluster storms. They are accompanied by strong damaging downburst winds that are the cause of line echo bowing (Fujita, 1973). Bow echoes evolve in three stages: Tall echoes, bow echoes, and comma echoes (Fujita et al., 1979; Przybylinski, 1995). During the first stage, intense downbursts on the rear flank result in a distortion of the line segment. During the second stage, the center forms a spearhead with anticyclonic and cyclonic rotation at the edge of the bow. With strong winds, the last stage evolves into a comma-echo with a rotation head at the upper end of the bow.
According to Johns and Hirt (1987), severe wind damage or convective gusts exceeding 26 m s^{-1} are criteria for the formation of a derecho, which is a large complex of thunderstorms moving with straight-line winds.

To summarize, Table 2.2 lists the types of thunderstorm organization with the respective characteristics. Adapted from Maddox (1980) and Weisman and Klemp (1982).

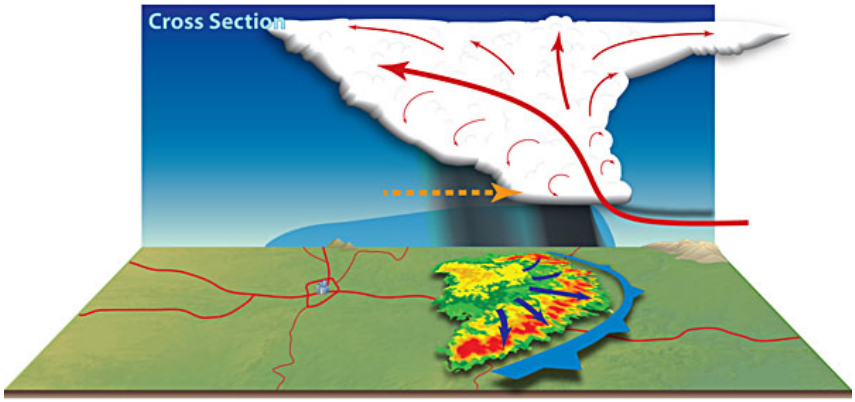

Fig. 2.8.: Cross-section of a bow echo. Red arrows represent updrafts and the blue braded contour marks the location of the gust front. The colored surface on the ground is the radar signature of a bow echo with reflectivity values. Yellow depicts low reflectivity values towards red representing high values (NWS, 2000).

Tab. 2.2.: Physical characteristics of thunderstorm systems.

Organization	Horizontal spatial extension	Lifetime	Hazard potential
Single-cell	1-10 km	30 min	low
Multicell	up to 50 km	few hours	modest-high
Supercell	$\sim$ 50 km	several hours	highest
MCS (MCC)	> 100 km	$\sim$ 24h	very high
Squall-line (MCS)	> 100 km	$\sim$ 24h	very high

2.3. Lightning

2.3.1. Lightning definition

Lightning is a sudden electrical discharge that occurs during a thunderstorm between differently charged regions within a cloud (called intra-cloud lightning or IC), between two clouds (CC lightning), or between a cloud and the ground (CG lightning). IC lightning is the most frequently occurring type (Soula et al., 1998) between the upper anvil portion and lower regions of a thunderstorm (Houze, 1993). Since the base of a thunderstorm is usually negatively charged, this is where most CG lightning originates (Pruppacher and Klett, 1997), and this region is typically at an elevation where freezing occurs within the cloud. Freezing, combined with collisions between ice and water, appears to be a critical part of the initial charge development and separation process (Soula et al., 1998). During wind-driven collisions, small ice crystals tend to develop a positive charge, while larger particles, such as graupel, develop a negative charge (microphysical charge separation) (Houze, 1993). Updrafts within a cloud separate the lighter ice crystals from the heavier graupel (macrophysical charge separation) causing the top region

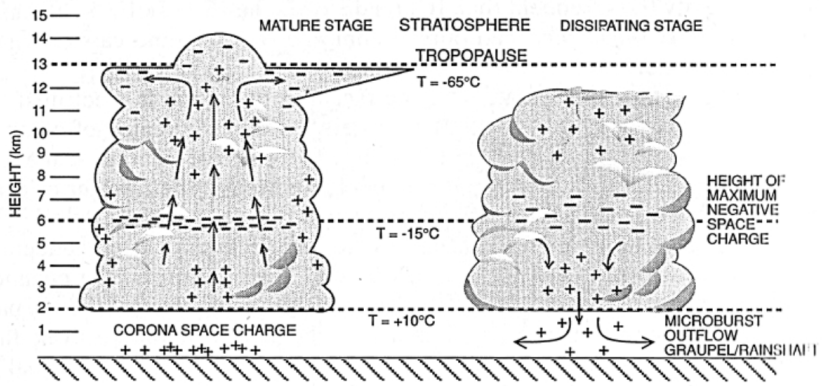

Fig. 2.9.: Polarity structure of thunderclouds during mature (left) and dissipating (right) stages (Houze, 1993).

of the cloud to accumulate positive charges, while the lower level accumulates a negative area charge (Beard and Ochs, 1984). The charge transfer is dependent on the temperature range in the cloud (Houze, 1993). In addition, charge separations can occur during phase transitions (Tobin, 1974). Because of these previous processes, a tripole structure often forms within a thunderstorm (Figure 2.9).

2.3.2. Lightning formation

Few stages are necessary to produce a CG lightning, described for the first time by Kasemir (1960). At first, the concentrated charge within the cloud must exceed the insulating properties of air. Then, a channel of ionized air, called a "leader," is initiated from a charged region in the thundercloud. Leaders are electrically conductive channels of partially ionized gas that travel away from a region of dense charge. Negative leaders propagate away from densely charged regions of negative charges, and positive leaders propagate from positively charged regions. When a stepped leader approaches the ground, the presence of opposite charges on the ground enhances the strength of an electric field. The electric field is stronger on grounded objects, such as trees and tall buildings (Soula et al., 1998). Once a conductive channel bridges the air gap between negative charge excess in the cloud and the positive surface charge excess below, a massive electric discharge follows. This is the return stroke, which is the most luminous and noticeable part of the lightning discharge. The electrical activity of a channel can lead to multiple strokes. Several strokes represent lightning or flash.

2.4. Hail formation and microphysics

2.4.1. Definition of hail and characteristics

Hail is a type of precipitation formed by a solid ice core and small air envelopes with a total diameter exceeding 5 mm (the standard by WMO). Below this diameter, the pellet is called graupel composed of

snow crystals and rimed droplets with a soft consistency. Different hail sizes can be compared to circular objects together with typical terminal velocities, such as those listed in Table 2.3.

Tab. 2.3.: Hailstones of different sizes and analogous objects, adapted from the French association Anelfa (Association nationale d'études et de lutte contre les fléaux atmosphériques).

Size of hailstones	Diameter	Analogous object	Average velocity (km h^{-1})
Small	0.5 - 1 cm	Pea	42
Small - medium	1 - 2 cm	Grape seed	60
Medium	2 - 3.5 cm	Nut	86
Large	3.5 - 5 cm	Golf ball	99
Severe	5 - 7 cm	Egg / Tennis ball	121
Extreme	7 - 10 cm	Bocce ball	131
Giant	> 10 cm	Grapefruit	> 135

Giant hailstones with diameters larger than 10 cm are rare but can occur during intense hailstorms. For example, M. Kaschuba collected a hailstone of 14.1 cm diameter with a weight of 360 g from a severe supercell near Undingen in Southern Germany on 28 July 2013 (ESWD, 2013) representing the largest documented hailstone in Germany. The largest hailstone worldwide, with a diameter of 20 cm, was collected during a supercell in Vivian, South Dakota, USA on 23 July 2010 weighing 880 g. The heaviest hailstone at approximately 1 kg was found in Gopalganj District, Bangladesh on 14 April 1986 (Monfredo, 2011).

Hail is produced by various processes and mechanisms on different spatial and temporal scales in organized thunderstorms cells, such as multicells, supercells or MCSs. The long persistence of hailstones within clouds is responsible for the accumulation of layers of ice or water around the main core. The hailstones density varies from $\rho \approx 0.7$ - 0.9 g cm^{-3} according to Pruppacher and Klett (1997). The weight of a hailstone and its composition (ice, water) determine the terminal fall velocity V_t, (Gunn and Kinzer, 1949). The terminal velocity results from the equilibrium between drag, buoyancy, and gravity forces (Gunn and Kinzer, 1949). The drag force is a type of fluid friction exerted opposite of gravity. The drag force (Stokes friction) is proportional to the squared velocity for a turbulent flow (Castellano et al., 1994):

$$F_D = \frac{1}{2}\rho {V_t}^2 C_D A \qquad [2.47]$$

In equation (2.47), F_D is the drag force, ρ is the density of the air, A is the cross-sectional area, and C_D is the drag coefficient.

The drag coefficient depends on the shape of the object and on the Reynolds number R_e defined by the ratio of inertial to viscous forces:

$$R_e = \frac{vD}{\nu} \quad [2.48]$$

D represents the diameter of the hailstone and ν is the kinematic viscosity of the fluid. R_e is a dimensionless number depending on the type of the flow regime. R_e is low (R_e < 2,000) for laminar flows, between 2,000 and 4,000 for transitional flows, and high (> 4,000) for turbulent flows (Reynolds, 1883). With increasing Re or diameter D, C_d decreases by almost an order of magnitude yielding an increase of V_t by about a factor of 3 rather than remaining constant (Heymsfield and Kajikawa, 1987).

If the gravitational force is equal to the Stokes equation friction (according to equation (2.47)), then the terminal fall velocity can be written as:

$$V_t = \left(\frac{2mg}{\rho C_d A}\right)^{0.5} \quad [2.49]$$

As C_D is difficult to calculate, several authors proposed a simplified equation relating V_t to the hailstone diameter. For example, for D < 8 cm at 800 hPa and for 0°C, Auer (1972) proposed:

$$V_t = 9\left(\frac{\mathrm{D}}{\mathrm{cm}}\right)^{0.8} \mathrm{m\ s^{-1}} \quad [2.50]$$

From hail observations in Canada, Lozowski and Beattie (1979) concluded:

$$V_t = 12.43\left(\frac{\mathrm{D}}{\mathrm{cm}}\right)^{0.5} \mathrm{m\ s^{-1}} \quad [2.51]$$

For dry and smaller hailstones (D < 2 cm), Knight and Heymsfield (1983) proposed:

$$V_t = 8.445\left(\frac{\mathrm{D}}{\mathrm{cm}}\right)^{0.553} \mathrm{m\ s^{-1}} \quad [2.52]$$

2.4.2. Hailstones growth

Hail is created from the interaction between diverse processes and mechanisms on different scales. Ice particles, such as graupel and hail, form in cumulus clouds where a sufficient concentration of ice crystals and supercooled droplets prevail (AMS, 2000). Various particles can be present in a cold convective cloud (temperature below 0°C), including ice crystals, snow, supercooled droplets, frozen drops, graupel, and hail. Two primary mechanisms of ice nucleation exist through which ice nuclei can form larger ice particles (Heymsfield and Kajikawa, 1987).

Nucleation

The beginning of hail development is the formation of small droplets or ice crystals, named nucleation. Two types of nucleation must be differentiated: Homogeneous nucleation, where the formation of hydrometeors from a pure water vapor phase, and heterogeneous nucleation, where an aerosol with specific

conditions is involved (Matsumoto et al., 2002).
The surface tension of small cloud droplets is high due to an unfavorable ratio of surface to volume. Thus, supersaturation between 100 and 300% are needed for homogeneous water nucleation (Vali, 1971). In the case of ice nucleation, the random coincidence of water molecules is transferred into a solid configuration of the ice crystal. The release of heat due to freezing leads to an unstable configuration of the ice particle due to thermal molecular motion (Heymsfield, 1978). The lower the temperature, the lower the molecular motion and the more stable the configuration: homogeneous freezing may occur only at temperatures below -38°C. For higher temperatures, homogeneously nucleated hydrometeors remain in the liquid state, referred to as supercooled droplets (Vali, 1971).

Heterogeneous liquid water nucleation (condensation) requires either a wetting aerosol with a given initial radius or a water-soluble aerosol in solution (Heymsfield and Kajikawa, 1987), which substantially reduces the supersaturation. Aerosols involved therein are referred to as Cloud Condensation Nuclei (CCN) (Twomey, 1959).
For heterogeneous ice nucleation (deposition), a special aerosol (ice nucleus or ice forming nuclei, IN) is required with a similar grid structure compared to the ice (Dymarska et al., 2006). The lattice structure of ice is elastically deformed when the two grids of the ice and IN are slightly different. Thereby, the surface tension increases at the interface. With different lattices, the interface can be moved with some molecules remaining unbounded (Burton and Oliver, 1935). This increases the enthalpy of the interface, depending on the are temperature: the higher the temperature, the higher the surface tension and, thus, the lower the ice nucleation efficiency (Fletcher, 1958).
Heterogeneous ice nucleation can be realized through four fundamentals modes according to Cooper (1986): (1) deposition nucleation, describing ice formation on IN directly from the water vapor phase due to supersaturation compared to the ice phase, (2) condensation nucleation on IN in droplets that initiate ice formation, (3) contact nucleation where freezing of a supercooled droplet occurs after contact with an IN, and (4) immersion freezing with aerosols functioning as an IN for one or, in the best-case scenario, all heterogeneous ice nucleation modes.

Aerosols can be effective as IN under a few conditions according to Pruppacher and Klett (1997). They need to be highly water-insoluble, and they must have a minimum size, comparable to those of the ice embryos or nuclei ($D > 0.1\ \mu m$). Therefore, the critical size is dependent on the chemical properties and the nucleation mode. Because of these different requirements, only a few aerosols are appropriate as IN (Heymsfield and Kajikawa, 1987). The low number of IN available in the atmosphere results in a high concentration of supercooled droplets in deep convective clouds. Increasing the concentration would lead to instant freezing of the supercooled droplets. This is the proposed principle of cloud seeding with, for example, silver iodide released from aircraft or ground generators (Dessens, 1986), which, however, is highly controversial (Schmid et al., 1997; Gertzman and Atlas, 1977).
The droplets originating from nucleation grow through water vapor diffusion or coagulate into larger

droplets. Frozen drops can develop at low temperatures or by the previously discussed freezing process. On the other hand, the diffusion of water vapor (deposition) leads to the growth of ice crystals (Dymarska et al., 2006). Depending on temperature and humidity, ice plates, prisms, dendrites (hexagonal form) or needles may form. Ice crystals can form larger arrangements by aggregation (snow).

Hail growth in cold clouds

The formation of hail can be differentiated in two stages: the formation of a hail embryo and the further growth into a hailstone. Almost all hailstones initiate as a hail embryo in the form of a graupel particle or large frozen drop as the central growth unit (Knight and Knight, 1970). Graupel forms from ice crystals or frozen drops through the further deposition of water vapor and, most important, by impinging of supercooled droplets and the resulting spontaneous freezing (Heymsfield and Kajikawa, 1987). This process is denoted as riming, whereas the process itself is called accretion. For this process, ice particles must grow to sufficient size before they can grow further via riming (Heymsfield and Kajikawa, 1987). Columns and double plates are especially good rimmers for sizes above 50 μm. The process is most efficient for temperatures between 0 and -5°C because of the high concentration of liquid water present at these temperatures. Graupel has a density of 0.05 and 0.89 g cm $^{-3}$ depending on the temperature and the motion of supercooled droplets occurring on ice particles (Rasmussen and Heymsfield, 1985).
The further growth from graupel to hail takes place by additional accretion and diffusion at temperatures ideally between -10 and -20°C. As the number of ice particles in this temperature range is low, their mass change rate can be estimated with the supercooled droplets assuming continuous growth. Pruppacher and Klett (1997), for example, related the mass change rate of accretion and diffusion and found that the latter can be neglected. This allows for the easy identification of the conditions for rapid growth of large hail: (1) a long-lived storm, (2) high updraft velocity that increases the difference between the fall velocity of hailstones and cloud drops (Ludlam, 1958;Cheng and English, 1983; Browning and Foote, 1976; Musil et al., 1991), and (3) high liquid water content. As this content is also dependent on the temperature, hail grows most efficiently between -10 and -20°C.

Growth modes: dry and wet growth

Hailstones are usually composed of alternating transparent and opaque layers due to a different type of growth regime depending on the surface temperature of the hailstone. Dry growth occurs at a temperature below 0°C. Due to nearly instantaneous freezing, several air bubbles are enclosed. The amount of these air inclusions is proportional to the freezing rate (Vali, 1971). The higher the freezing rate, the higher the proportion of air inclusions and the more opaque the layer. Thus, the opaque layer density is lower than the transparent layer. In contrast, wet freezing takes place at a surface temperature of 0°C. Consequently, liquid water can penetrate into hail pores and form translucent layers having a density between 0.8 and 0.9 g cm^{-3}.
To determine whether dry or wet growth occurs, a heat-budget balance is determined for a hailstone

(Pruppacher and Klett, 1997). This includes heating by conduction, vapor deposition, accretion, and aggregated cloud water (Straka, 2009):

$$\frac{dq_{cond}}{dt} + \frac{dq_{diff}}{dt} + \frac{dq_{rime}}{dt} + \frac{dq_{ice}}{dt} = 0 \quad [2.53]$$

The heating conduction is the first term of equation (2.53) and can be written as:

$$\frac{dq_{cond}}{dt} = 2\pi DK(T_{ice} - T)f_h \quad [2.54]$$

where T_{ice} is the surface temperature of hail, T is the temperature of the environment, K is the thermal conductivity, and f_h is the heat ventilation coefficient.

Deposition and sublimation represented by the second term are given by (Straka, 2009):

$$\frac{dq_{diff}}{dt} = 2\pi DL_s \upsilon \rho (q_v - q_{s0})f_v \quad [2.55]$$

with q_v representing the vapor mixing ratio of air, q_{s0} is the saturation mixing ratio at 0°C, L_s is the enthalpy of sublimation, f_v is the vapor ventilation coefficient, and υ is the water vapor diffusivity.

The riming term can be determined by:

$$\frac{dq_{rime}}{dt} = \frac{dM_{liquid}}{dt}(F_f L_f + c_L[T - T_{ice}]) \quad [2.56]$$

where c_L is the specific heat of the liquid, L_f is the enthalpy of freezing, M_{liquid} defines the liquid water content, and F_f is the fraction of frozen liquid. This term must be modified if liquid is retained inside the hailstone or if some of the liquid accreted by the hailstone is shed. In the latter case, an additional term, $E_{shed}\ c_L\ (T_L\text{-}T_0)$, with E_{shed} as the fraction shed, must be added to the previous equation.

The last term of the heat-budget equation considers when the heat changes due to collisions with ice of different temperatures and sticking (Straka, 2009):

$$\frac{dq_{ice}}{dt} = \frac{dM_{ice}}{dt}(c_i[T - T_{ice}]) \quad [2.57]$$

where c_i is a constant and M_{ice} is the ice content. The surface temperature of hail, T_{ice}, assuming no heat storage, can be derived and simplified from the above equations using Nelson's procedure (Nelson, 1983):

$$T_{ice} = \frac{(c_1 + c_2 T)\upsilon_{ice} + c_3 T}{c_4 + c_5 \upsilon_{ice}} \quad [2.58]$$

where c_1 to c_5 are constants and υ_{ice} is the growth rate changing with accretion. To simplify, T_{ice} depends on the temperature of the environment and on the growth rate of accretion, which in turn depends on the density of supercooled droplets.

Macroscopic hail formation in thunderstorms

When the surface temperature of a hailstone reaches 0°C, a water film or an ice-water mixture is produced around the surface. Thus, a hailstone is not always compact and solid but can be spongy (spongy

ice). Decisive factors for the growth of large hail include a long residence time in the cloud, a high vertical velocity, and a high amount of liquid water content. Thus, large hail is present only in organized thunderstorms, such as in multicells or supercells (Markowski and Richardson, 2010). In multicells consisting of various single-cells as described in Section 2.2, hydrometeors can be transported among the different single-cells during their different stages. The process begins with condensation on the downshear flank of the system. Subsequently, liquid water is transported vertically, forming an ice crystal or a bigger ice particle by aggregation. If it reaches cell 2 or cell 3 in Figure 2.5 (top panel), entailing a high amount of supercooled water droplets, then the particle continues to grow in that region until it falls to the ground from cell n-1 due to its weight (Markowski and Richardson, 2010). In total, the residence time of hydrometeors in the cloud complex is long enough to form hail.
The growth of hail is different in a supercell (Browning and Foote, 1976). A high amount of hail embryos prevails on the backside and in the upper part of the updraft. In contrast, a high concentration of supercooled water droplets is present in the middle part of the updraft. Thus, hail embryos and supercooled drops are mixed towards a strong updraft, and large hailstones can form rapidly by accretion (Heymsfield et al., 1978). Finally, hailstones are transported to the forefront of the updraft because of wind shear, where they fall on the ground when the updraft is no longer able to maintain the hailstone in the cloud.
If the hail embryos grow in the rotating updraft of the supercell, then they are slowly transported on spiral paths to the top of the cloud (Markowski and Richardson, 2010). On the long path, a high number of supercooled droplets can accumulate so that large hailstones may occur, which fall directly on the front part of the upwind region.

2.5. Hail observation systems

The local area affected by hail, termed hail streaks, makes it difficult to catch single hail events properly. As the diameter of hailstones is not recorded by remote-sensing data (weather radar, satellite data), the severity of hail events is difficult to estimate. Hail observations from eyewitness recorded in the ESWD increased in the last years, but some limitations exist.

Hail sensors measure different physical parameters of hail, such as hailstone diameters (Long, 1987), momentum, and kinetic energy, and different regions operate a hail pad network (for example, Admirat, 1973; Morgan Jr and Towery, 1975; Mezeix et al., 1976; Changnon, 1977; Berthet et al., 2011; Sánchez et al., 2008). Over the past decades, various kinds of instruments were introduced to record the physical characteristics of hailstones. Morgan Jr and Towery (1976), for example, listed the hailcube, the hail-wind detector (providing wind direction), and a recorded hailgauge to determine the duration of the storm.

To cover a larger geographic area, simple hail pads have been installed and are in operation in several regions. The hail pad is a simple and cheap device developed by Canadian researchers (Schleusener, 1960) to record the trace of hailstones reaching the ground. It consists of a metal pole at a height of 1.50 m holding a horizontal plate (Berthet et al., 2011; Palencia et al., 2009 of extruded polystyrene with a size of 30 cm x 40 cm^2. After the storm, the plate retains deformations caused by hailstone impacts. In laboratories, these impacts are made visible by black ink covering the plate with a printing roll (Berthet et al., 2011). A scanner performs the post-storm counting to determine the diameter of each hailstone causing an impact (Berthet et al., 2011). From this, distinctive parameters can be determined, such as the total number of hailstones, the intensity, the corresponding mass, and its kinetic energy (Dessens and Fraile, 1994). The long-term measurements and a large number of sensors of the hail pad network in France allow for climatological studies and trend analysis (Dessens et al., 2015). More recently, a pilot project with the installation of a hail sensors network was conducted in Southwest Germany to account for the lack of measurements in a region highly affected by hailstorms (Puskeiler, 2013). The automatic hail sensors detect the momentum and kinetic energy of the hailstones and provide a size spectrum. Two sensitive microphones record momentum and energy signals of the hailstones, which are converted to diameter.

2.6. Radar basics

This section describes the background and operating modes of weather radars. A definition and description of the radar hardware are provided first. Then, equations for distributed targets are established, and possibilities to identify hail are discussed along with limitations and radar artifacts.

2.6.1. Weather radar and hardware

Radar is the acronym for "Radio Detection And Ranging," which emits radio waves to detect targets, such as aircraft, ships, motor vehicles or hydrometeors. The development and use of radar began before and during World War II (Marshall et al., 1955; Batt, 1991).

A radar includes four main components (Figure 2.10) of a transmitter, antenna, receiver, and display (Skolnik, 1962; Rinehart, 1991). First, the transmitter generates an electromagnetic wave (pulse of energy), which is emitted by the antenna in predefined directions until reaching a target that reflects or scatters the signal in many directions (Levanon and Mozeson, 2004). The signal is especially well reflected by targets possessing a high electrical conductivity, such as metal (in the case of aircraft) or wet targets. The backscattered signal reaches the antenna and is amplified by the receiver because the signal is substantially weaker than the emitted (Hughes, 1983). Because of multiple scans, the antenna usually rotates about a vertical axis, scanning the horizon in all directions. Radar waves scatter in different ways

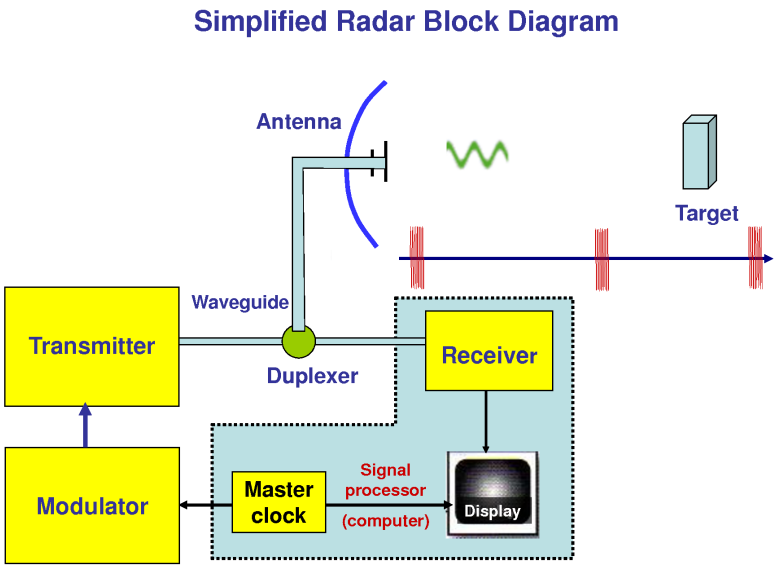

Fig. 2.10.: Block diagram of a weather radar (Modified from (Doviak and Zrnic, 2014)).

depending on the wavelength (Calderbank et al., 2009) and the target shape. Radar frequency bands are subdivided into several ranges. According to AMS (2000), principal radio bands used for precipitation detection and clouds include the following: The frequency range of L-band radars is between 1 and 2 GHz (corresponding to a wavelength range of 15 to 30 cm), whereas S-band radars emit frequencies from 2 to 4 GHz (7.5-15 cm). For C-band radars, the frequency range is situated between 4 and 8 GHz (3.75-7.5 cm), and for X-band radars, it is between 8 and 12 GHz (or 2.5-3.75 cm). Radars operating in these four frequency bands (L, S, C , and X) are used in this study. Further, higher bands exist, such as K-, Ka-, Ku-, V- or W- bands, but they can suffer from high attenuation by atmospheric gases, cloud particles or precipitation. Therefore, they are often employed for special observations only.

Dual-polarized radar

A more recent method of detecting the type of precipitation and, thus, separating raindrops from hail (Bringi et al., 1982), is the dual polarization. A weather radar alternately transmits two beams with orthogonal polarization. Some modern polarimetric radar, such as METEOR 1500 Germatronik, can emit both beams simultaneously (Meischner, 2005). Reflectivity in horizontal (Z_H) and vertical polarizations (Z_V) are similar for spherical hailstones (Waldvogel et al., 1979). The differential reflectivity (Z_{DR}) aims to detect the presence of hail. Low differential reflectivity values represent a hail signature.

2.6.2. Radar equations for distributed targets

Radar reflectivity

The radar reflectivity is a parameter that is related to the total backscattering signal of a radar target. It is proportional to the energy of all particles that scatter energy back to the antenna (Wexler and Atlas,

1963). The received energy depends on many factors, including the distance to the radar, the wavelength, the antenna shape, and the emitted energy. For meteorological purposes, the radar reflectivity is determined as a function of the properties of the scattering targets (Barton, 1988). The relation between radar reflectivity and various specific radar parameters is provided by the radar equation, which describes the connection between the radiated power P_t and the received power P_r (Sauvageot, 1992):

$$P_r = \frac{P_t G^2 \lambda^2 L^2}{64\pi^3} \frac{c\tau}{2} \frac{\eta}{r^2} \int_{\Omega}^{max} f^4(\theta,\Phi)\, d\Omega \qquad [2.59]$$

G is the antenna gain (Klein and Degnan, 1974), which is the ratio of the radiation intensity by combining the antenna relative to isotropic radiation, λ is the wavelength, L is a term to account for all losses applying to the signal, r is the distance of the signal to the radar, c is the speed of light, τ is the pulse duration, η is the radar reflectivity, which will be further detailed in equation (2.63), and f(θ, Φ) is the antenna-specific intensity distribution under the azimuth angle θ and the elevation angle Φ (Rinehart, 1991). For a parabolic antenna, these two quantities are equal (Soumekh, 1999). The integration is carried out over the solid angle of the pulse volume Ω, where a homogeneous distribution of the scattering particles is assumed. Since the backscattering particles are small compared to the wavelength (which is mostly the case for meteorological radars), the Rayleigh approximation can be used (Jones, 1979). For hail, this Rayleigh relation has inaccuracies because of the large diameter of the backscattering body. A more accurate method for large scattering bodies, such as hail, is the use of the Mie relation (Chỳlek, 1976), a solution of Maxwell's equations. Due to the relatively large diameter of the scattered body compared to the wavelength, the angle between the incident and backscattered radiation and the shape of the scattering body must be considered. Since this information is not available for meteorological targets, the Rayleigh approximation is still usually applied (Jones, 1979).
The backscattering cross-section σ for the Rayleigh approximation is given by:

$$\sigma = \frac{\pi^5 |K_i|^2 D_i^6}{\lambda^4} \qquad [2.60]$$

where the subscript i refers to the mixture of the targets and $|K_i|$ is the magnitude of the parameter related to the complex index of refraction m given by:

$$K = \frac{m-1}{m+2} \qquad [2.61]$$

The complex refraction index is $m = n \pm ik$ where n is the absolute refractive index of a sphere, $i = \sqrt{-1}$, and k is the absorption coefficient of the sphere. The value of $|K|^2$ depends on the material, temperature, and wavelength of the radar. Battan (1973) gives appropriate values of $|K|^2$ for ice and water at various temperatures and wavelengths, but usually $|K|^2 = 0.93$ for water and $|K|^2 = 0.197$ for ice is used (Sauvageot, 1992).

Considering an ensemble of many hydrometeors with a spectral density distribution $n(D)dD$, the total number is equal to the moment of zeroth number:

$$N_T = \int_0^\infty n(D)\, dD \qquad [2.62]$$

The radar reflectivity η results from the sum of the backscattered signal of individual hydrometeors per unit volume as:

$$\eta = \int_0^\infty \sigma(D) n(D)\, dD \qquad [2.63]$$

Assuming the Rayleigh approximation for small particles, it follows:

$$\eta = \frac{\pi^5}{\lambda^4}|K|^2 \int_0^\infty D^6 n(D)\, dD = \frac{\pi^5 |K|^2}{\lambda^4} Z \qquad [2.64]$$

In the previous equation, z represents the radar reflectivity factor, which is proportional to the number of drops per unit volume and the sixth power of the drops diameter (in mm ^{6} per m $^{-3}$).

$$Z = \int_0^\infty n(D) D^6\, dD \qquad [2.65]$$

The unit of Z is in mm ^{6} m $^{-3}$, which is not convenient. Thus, Z is often given in a logarithmic unit, with Z in decibels (dBZ).

$$Z(\mathrm{dBZ}) = 10\, \log[z(\mathrm{mm^6 m^{-3}})] \qquad [2.66]$$

For example, $Z = 1$ mm^{6}m$^{-3} = 0$ dBZ. For moderate rain, $Z = 1000$ mm^{6}m$^{-3} = 30$ dBZ, for extreme heavy rain or hail, $Z = 10^6$ mm^{6}m$^{-3} = 60$ dBZ (Sauvageot, 1992).

Reflectivity: rainfall rate relationships

The precipitation rate R is often used for meteorological purposes to estimate rainfall amounts:

$$R = \frac{\pi}{6} \int_0^\infty D^3 V_f(D) n(D)\, dD \qquad [2.67]$$

where V_f is the terminal velocity of a precipitation particle.

A Marshall and Palmer (1948) distribution is often used, to relate the size distribution of raindrops to the rainfall rate.

$$n(D) = N_0 \exp^{-\Lambda D} \qquad [2.68]$$

where the parameter $\Lambda = aR^b$ depends on the rainfall rate R. N_0 as well as a and b given from Marshall and Palmer (1948) are $N_0 = 8000$ mm^{-1}m^{-3} and $\Lambda = 4.1\mathrm{mm}^{-1}(R/\mathrm{mmh}^{-1})^{-0.21}$.

The insertion of a and b values given by Marshall and Palmer (1948) yields the so-called $Z-R$ relation:

$$Z(\mathrm{mm^6 m^{-3}}) = 296\, R^{1.47}\ [\mathrm{mm\ h^{-1}}] \qquad [2.69]$$

Adapted to stratiform precipitation yields (Battan, 1973):

$$Z(\mathrm{mm^6 m^{-3}}) = 200\,R^{1.6}\ [\mathrm{mm\ h^{-1}}] \qquad [2.70]$$

whereas for convective systems, Sekhon and Srivastava (1970) gives a relation of

$$Z(\mathrm{mm^6 m^{-3}}) = 300\,R^{1.35}\ [\mathrm{mm\ h^{-1}}] \qquad [2.71]$$

Today, the National Weather Service uses $Z = 300R^{1.4}$ as the primary default $Z - R$ relation of the WSR-88D radar network in the USA.

2.6.3. Hail identification by radar

Numerous approaches exist to identify hail from 2D or 3D radar data (Puskeiler, 2013). For example, Kunz and Kugel (2015) tested several hail criteria based on radar data and determined their respective skill, in comparison to insurance damage data.

Hail identification by radar

Two-dimensional (2D) radar data are used for the Mason criterion (Mason, 1971). For this purpose, the MaxCappi (Maximum Constant Altitude Plan Position Indicator) is used representing the maximum of radar reflectivity and what is projected on a surface. According to the Mason criterion

$$Z \geq 55\ \mathrm{dBZ} \qquad [2.72]$$

hail is highly probable. This criterion is a hail proxy and not a direct proof of hail presence on the ground. The reflectivity can also be achieved even with very large raindrops, such as in typical thunderstorms, due to the proportionality of the sixth power of the hydrometeor diameter (Mason, 1971).

In a case study from Eastern Australia, Schuster et al. (2005) found the 55 dBZ to be a good approximation of a hail swath causing significant damage to buildings. Puskeiler et al. (2016) also found this threshold is a good approximation for hail presence in 2D radar data. Using conventional single-polarization radars between 2005 and 2011, the authors evaluated radar-derived hail days with loss data from an insurance company and confirmed the reliability of the reflectivity values and insurance data expressed by a Heidke Skill Score HSS of 0.61 for 56 dBZ, even though they found the Waldvogel criterion band on 3D reflectivities to be a better hail proxy.

Hail identification by 3D radar

Hail can also be identified from three-dimensional (3D) radar reflectivity by using, for example, the widely-used criterion of the probability of hail (POH) (Waldvogel et al. 1979), which predicts the probability of hail of any size. The criterion relies on the vertical distance between the freezing level and a certain upper-level reflectivity (echotop), originally the 45 dBZ reflectivity, as a proxy for hail. It is

assumed that this column represents the hail growth zone in a thunderstorm cloud. The larger the vertical extent, the higher the probability for hail to occur. This approach was successfully applied in many studies on hail identification (e.g., Waldvogel et al., 1979; Auer, 1972; Witt and Nelson, 1991 and Holleman, 2001). According to Waldvogel et al. (1979), hail may be expected for a distance of 1.4 km between the echotop H_{45dBZ} and the height of the freezing level H_{0C}:

$$H_{45dBZ} - H_{0C} \geq 1.4 \text{ km} \quad [2.73]$$

The Waldvogel criterion was also used by Holleman (2001), who employed 1.76 km between the echotop of 45 dBZ and the height of the freezing level. This slight difference compared to the 1.4 km found by Waldvogel et al. (1979) can simply be due to different devices used to calculate the height of the freezing level. A quantity denoted to as probability of hail (POH) and expressed in % was given by Holleman (2001):

$$POH = 0.133\,(H_{45dBZ} - H_{0C}) + 0.39 \quad [2.74]$$

The higher the POH, the higher estimated probability of hail.

In the works of Makitov (1999), Schuster et al. (2005) and Saltikoff et al. (2010) hail occurrence related to POH was also studied in Australia, Argentina, and Finland. In these studies, the hail criterion by Waldvogel et al. (1979) was also slightly transformed.

Auer and August (1994) combined radar reflectivity at low altitudes and cloud top temperatures (T_B) provided by the infrared radiance of satellites (for example Météosat) in New Zealand. If

$$2.6\,Z_{2km} + T_B \geq 85 \quad [2.75]$$

where Z_{2km} is the reflectivity at a 2 km height, then hail occurs with a high probability.

Hail detection algorithm (HDA)

The National Severe Storms Laboratory (NSSL) developed an algorithm for the detection of severe hail (D $\geq$ 19 mm), including the prediction of maximum expected hail size (Witt and Nelson, 1991). This hail detection algorithm (HDA) is based on a previous radar algorithm (SCIT), which could only determine the absence or presence of hail in a storm. HDA additionally estimates the probability of hail, the probability of severe hail (Diameter $\geq$ 19 mm), and the maximum expected size of each storm cell. To estimate the probability of severe hail, a severe hail index (SHI) was developed. SHI is derived from the vertical reflectivity and temperature profiles from the melting level to the top of a storm, neglecting reflectivity values below 40 dBZ and thereby expecting only ice content. Reflectivity values are first converted to a hail kinetic energy flux expressed in J m^2 s^{-1} given by Waldvogel et al. (1979):

$$\dot{E} = 5 \cdot 10^{-6} \cdot Z^{0.84} W(Z) \;\; [\text{J m}^2\text{s}^{-1}] \quad [2.76]$$

This equation has three solutions for the weighted function to find a transition between rain and hail $W(Z) : W(Z) = 0$ for $Z \leq Z_L$, $W(Z) = \frac{Z-Z_L}{Z_U-Z_L}$ for $Z_L < Z < Z_U$ and $W(Z) = 1$for Z$\geq Z_U$ where Z_L = 40 dBZ and Z_U= 60 dBZ.

After computing SHI, a probability function of hail is estimated by Witt et al. (1998) from which the probability of severe hail (POSH), expressed in %, can be determined. SHI is related to POSH by:

$$POSH = 29 \times ln\left(\frac{SHI(\text{J m}^{-1}\text{s}^{-1})}{WT(\text{J m}^{-1}\text{s}^{-1})}\right) + 50 \ \ [\%] \qquad [2.77]$$

The maximum expected hail size (MEHS) is also derived from the SHI using a simple empirical relationship:

$$MEHS = 2.54(SHI)^{0.5} \ \ [\text{mm}] \qquad [2.78]$$

The maximum size in MEHS represents the maximum diameter of a hailstone in mm. The relation between SHI and MEHS was determined by comparing SHI with observed hail sizes for 147 hail reports on 9 days with hail (Witt et al., 1998). The resulting curve between SHI and the observed hail sizes is the MEHS prediction in the HDA algorithm.

Vertically integrated liquid water

Another indicator of hail is the vertically integrated liquid water (VIL) introduced by Greene and Clark (1972). The VIL assess the amount of liquid water in the troposphere. The Z-R relation permits to convert radar reflectivity into liquid water content, derived from rainfall rates. VIL does have limitations. For example, VIL is underestimated for tilted updrafts where hail cores are difficult to sample (Amburn and Wolf, 1997). Non-precipitation echoes can alter VIL, and the relation between VIL values and hail size depends on numerous factors, such as synoptic environment, season, storm speed, and structure or elevation. To improve VIL quantification, Amburn and Wolf (1997), decided to normalize the parameter by dividing it by the height of the cloud top, determined by 3D radar data. Nevertheless, no agreement exists yet for the best threshold of hail detection using the normalized VIL.

2.6.4. Limitations and radar artifacts

Numerous artifacts exist in radar data, and the following summarizes the most important types.

Ground clutter

Ground clutter is an echo occurring when the radar beam reaches a fixed obstacle, such as mountains or buildings. Ground clutter occurs at low elevations and causes higher reflectivity values in the radar display (especially close to the antenna where the beam is near the ground), and can thus lead to a misinterpretation of data, for example, by confusion of ground clutter echoes with rainfalls or convective

cells (Billingsley, 1993). A useful method to avoid ground clutter is the use of a Doppler filter, which separates storms in motion from fixed objects by determining the radial velocity of the targets. Thus, ground clutter can be identified and filtered on or near a velocity equal to 0 (Sauvageot, 1992).

Moving targets

Birds or insects can appear as rings or dots of high reflectivity values on a radar display near the ground as well as on layers above the ground. These echoes can be attributed to birds or insects by analyzing the motion and directions of the targets. Signals returned from moving targets are usually single points with no repeating patterns so that these echoes can be quickly identified and suppressed.

Anaprop

Another type of ground clutter is anomalous propagation echoes (anaprop) that appear when the beam in a stable atmosphere is bent toward the surface. In the standard atmosphere, the radar beam spreads from the Earth's surface with a radius of curvature equal to 4/3 of the Earth's radius. The beam propagation is determined by the vertical profile of air temperature and water vapor pressure. For particular weather conditions (e.g., temperature inversion during a sea breeze or in the early night or morning), the beam refraction is increased and bent toward the surface where the clutter occurs. Anaprop may enable ground clutters to appear at greater elevations, which is problematic in mountainous terrains. These echoes can vary considerably according to prevailing tropospheric conditions and can be confused with precipitation. Amorati et al. (2000) assess these methods and indicates that an eventual correction of anaprop is only possible when anaprop or precipitation exist, but not when they appear together.

Bright band

Hooper and Kippax (1950) defined the bright band as a layer of high radar reflectivity within clouds. On a vertical profile of reflectivity, the bright band is characterized by high reflectivity values in the cloud at the height of the melting level. When snow and ice particles pass through the melting level, they begin to melt. The surface of an ice particle, in this case, is enclosed by a water film. Because liquid water has a much higher dielectric factor compared to ice ($K_{water} = 0.93$ and $K_{ice} = 0.197$) and since ice particles are larger than raindrops, reflectivity substantially increases due to the proportionality of the 6th power in diameter. Bright bands occur, however, mostly in stratiform clouds, whereas vertical mixing in convective clouds reduces this effect. Several studies considered the detection and the correction of this effect (for example, Huggel et al., 1996; Sánchez-Diezma et al., 2000).

Echo from lightning

When a radar beam hits lightning during a storm, extended echoes of several kilometers with high reflectivity can appear on a radar display (Ligda, 1956; Caylor and Chandrasekar, 1996). The ionized lightning combined with high temperatures lead to a specific reflection of the transmitted radar beam to

the antenna. In Linear Depolarization Mode (LDR), which is the ratio of power between an orthogonal received signal and a horizontal signal, lightning can be recognized by a low LDR.

Attenuation

The radar signal can be attenuated by precipitation and several gases in the troposphere, such as nitrogen, oxygen, and water vapor. Bean and Dutton (1966) estimated the attenuation from oxygen and water vapor as a function of frequency and showed that this attenuation remains below 10 GHz. Increasing reflectivity may correct atmospheric attenuation as a function of range and elevation angle. Attenuation by clouds is variable due to the high diversity of clouds including different amounts of water or ice droplets (Collin, 1985). For ice clouds, attenuation can be neglected. Attenuation by rain is more important than clouds, especially for shorter wavelengths, such as X-band radar, where significant attenuation occurs in almost all rain situations. Low reflectivities appear, especially, behind a convective storm. Using recursive correction formulas, correction can be made. As Blahak (2005) showed, an extinction correction is operationally not possible due to the high temporal and spatial variability of rainfall areas, particularly in convective cells.
A water film on the radome also attenuates the radar signal. The higher the rainfall intensity at the radar site, the greater the attenuation.

Beam blocking and shielding

In the vicinity of mountains, beam blocking and shielding can occur, leading to low or a gap of reflectivity values. Quantifying and correcting this effect is important particularly for precipitation estimations in mountainous areas (Young and León, 2009). Mountains can entirely block the radar beam so that the area behind mountains remains unseen on a radar composite (for example, Schmid Schmidt et al., 2008). In case of shielding, a weaker transmitted signal reaches the precipitation area leading to a weaker backscattered signal. Several authors attempted to correct for this effect, and one solution is to extrapolate reflectivity from higher to lower altitudes. Another example Fulton et al. (1998) used a beam correction scheme on NEXRAD precipitation processing system, which consists of modifying equivalent reflectivity factor measurements by adding 1 to 4 dBZ depending on the degree of occultation.

Beam height effects

When a cloud moves at a far distance from a radar station, the radar beam propagates toward the higher parts of the cloud. Thus, only the upper part of the cloud can be captured, and signals from the entire cloud or at lower layers, which contain most of the hydrometeors, are missing. As a result, the backscattered signal appears weaker than a nearer cloud. In the opposite case, the backscattered signal can appear strengthened for clouds situated near the radar station (Rinehart, 1991). An accurate determination of cloud height or the melting layer is therefore difficult. To properly calculate a target height, Raghavan (2013) proposed considering the beam curvature by combining several factors, such as the distance

target-radar station, the beam elevation angle, the refraction of electromagnetic waves in the atmosphere (pressure, humidity, temperature changes with height, and transmitted wavelength), and the refraction depending on the atmosphere.

3. Data and Methods

The spatial resolution of conventional observation data, such as measurements at weather stations, is not sufficient to capture local-scale hail events in their entire extent and intensity. Moreover, neither Germany, Belgium nor Luxembourg possesses a measurement system that detects the presence and diameter of hailstones. For this reason, various suitable methods are developed in this work combining meteorological records and remote-sensing data to deduce hail signals. Overall, radar data play a crucial role as they provide a high spatial-temporal accuracy about the location, duration, and intensity of convective systems. Section 3.1 describes the radar networks of the countries considered. The following section 3.2 explains the applied methods and corrections to reconstruct past and historical hail swaths.

3.1. Remote-sensing, hail reports, and reanalyses data

Radar data from Germany, France, Belgium, and Luxembourg are considered in this study. The radar products used are composites of MaxCAPPI, where a composite is an assembly of all local radar stations in a unique image at every time step. In this study, composites are available every five minutes. Two-dimensional radar is used in this study, as it is available for a long period. Of course, the vertical information contained in 3D radar products of single radars would allow for better identification of hail signals (for example, Delobbe and Holleman, 2006). However, the time-period for 3D data is shorter than for 2D products and would limit statistical analysis. Furthermore, the data volume (> 100 TB) is very large, and data transfer and storage could not fit with the available resources. Finally, the 3D data format of the French radar data is solely readable with specific software.

3.1.1. French radar network

The conception of the French radar network, named Aramis (Application Radar A la Météorologie Infra-Synoptique), started in the mid-1980s (Parent du Châtelet et al., 2005) and extended rapidly to 13 stations in 1995, principally equipped with C-band radars (λ = 5 cm). Their scan level initially only reached 1° above the horizon because the goal was to create a hydrologic network and to quantify precipitation near the ground. From 1996 to 2001, the program named Arc Méditerranéen (for Mediterranean bow) permitted the installation of an additional five S-band radars (λ = 10 cm) situated along the southern coastlines and Corsica in the southeastern part of France. The objective was to cover and identify regions affected by severe rainfall events (e.g., floods in Nîmes in 1988 or Vaison-La-Romaine in the Vaucluse in 1992, which claimed more than 50 victims). Severe flash-floods occurred almost every year in these

regions and required an adapted scanning strategy. By 2006, 27 radars were in operation (Gourley et al., 2006). New technologies, such as dual-polarization, have been implemented (22 radars of 24 were dual-polarized in 2010), which allow improved correction of echoes and attenuation and to identify the type of precipitation. All installed radars are Doppler radars to estimate radial velocities to obtain wind fields around the radar stations. Finally, the large area covered by radar devices with high resolution fulfill the requirements of data assimilation into modern numerical weather prediction models.
Until 2010, the Alpine regions remained as a gap in the radar network. For this reason, additional five X-band radars were installed, each covering a domain with a 50 km radius. The radar station at Mont Maurel was the first to operate in 2010 with a second radar added at Mount Colombis in 2012. Another radar was installed in Vars in 2013, and a new radar in Moucherotte is part of the network since the summer of 2015. The most recent X-band radar was installed at the airport of Nice in 2015 for a better investigation of wind fields aloft rainfall events. The radar station La Dôle covers the northern part of the French Alps, operated by MeteoSwiss since 1995 (Germann et al., 2006).

The French radar network today includes 29 radar stations with 19 C-band radars, 5 S-band (coverage up to 200 km), and 5 X-band radars (Figure 3.1). The C-band radars are situated along the Atlantic coast, in the center, and in the Northeast part of France. These regions belong to the flatlands of France. Hence almost no shielding effects perturb the emitted signals. The radar coverage provided by the stations Avesnois (current region Nord-Pas-de-Calais-Picardie) and Réhicourt-la-petite (Alsace-Champagne-Lorraine) permits to integrate Luxembourg completely and an important part of Belgium into the French composite.
Concerning the scanning strategy, there are 18 rounds per cycle of 15 minutes for both S- and C-band radars (Tabary et al., 2007). The elevations scanned during the cycle depend on the radar location (for example, going from 0.4° to 9.5° for the radar of Trappes near Paris). The resolution of differential reflectivity is 0.5°/240 m in polar coordinates and 1 km^2 in the Cartesian coordinate system. Differential reflectivity is the difference (in dB) between horizontal and vertical reflectivity as shown in Tabary et al. (2007), which, however, is not considered in this study due to the limited period when data are available. In the future, additional radars will be added to the ARAMIS network with implementations of new radar devices on the western side of Corsica, in the Morbihan and the Alps (Tabary, 2007).

French national composite

This study uses the composites of the French national mosaic representing instantaneous rainfall with a resolution of 1×1 km^2 every 5 minutes, computed in the national meteorological service center of Toulouse. Rainfall intensity is denoted as 'levels' in the raw data.
The national composites were stored for the period from 1999 to 2014 in GeoTIFF format, i.e., georeferenced TIFF images. The resolution is 2×2 km^2 from 1999 until mid-June 2009, and a finer resolution of 1 km^2 is available from the end of July 2009 to 2014. The first dataset is a stereographic polar projection

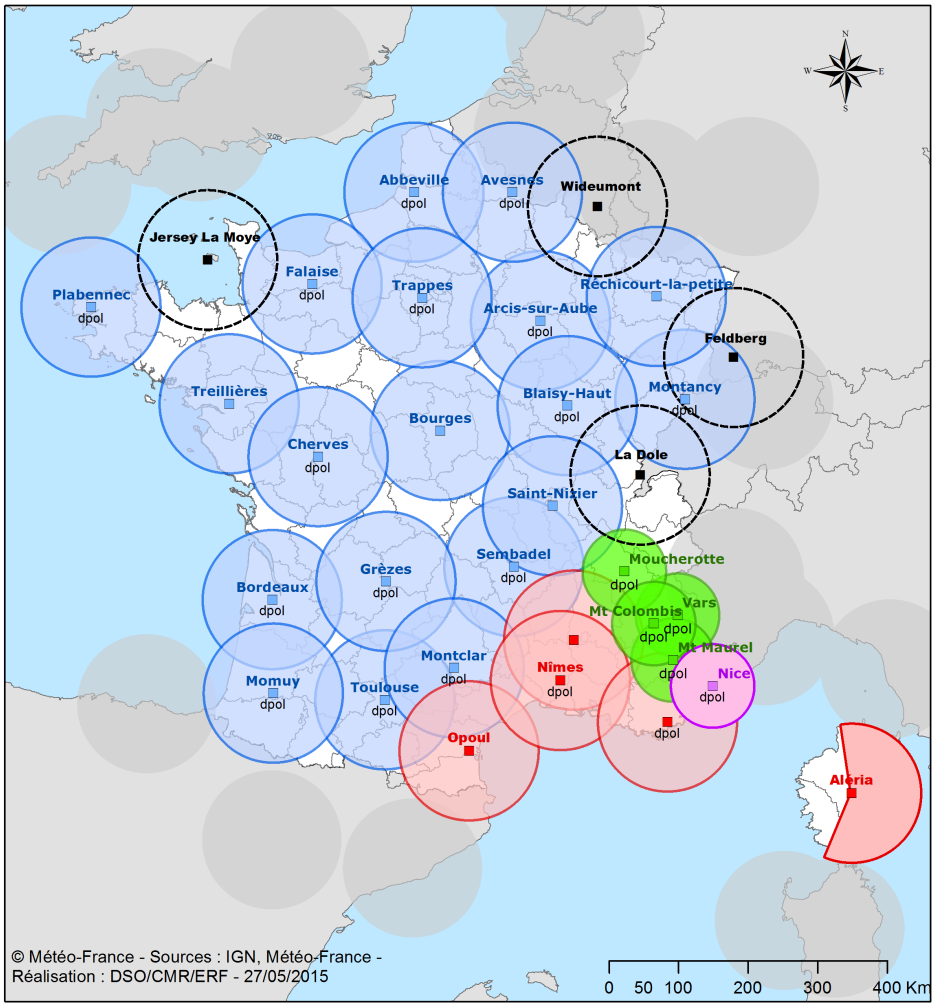

Fig. 3.1.: French radar network in 2015. Grey shaded circles represent radar ranges in foreign countries. Circles of S-band radars and C-band radars have a radius of 100 km, X-band radars have 60 km. A total diameter of 256 km is considered for S-band and C-band radars to cover the entirety of France and Belgium. Luxembourg is included in the Wideumont radar range (Météo-France, Pers. Comm).

with spherical earth of a radius of 6,370.997 km. The second dataset, extending from July 2009 to 2014, which also has a stereographic polar projection, but is based on an elliptical reference ellipsoid computed from WGS84. Additional information in the GeoTIFF format includes details about the projection, the four corner coordinates of the mosaic in the given projection, and the spatial resolution.

A first step was to compute the coordinates of longitude and latitude at each grid point in the respective

projection. Then, for data homogenization, each of the 2 × 2 km^2 composite was interpolated from 1999 to July 2009 to the finer grid of 1 × 1 km^2. This was performed by a linear interpolation of the coordinates between the two grids. The final size of each composite image is 1536 × 1536 grid points. The last step was to convert the 'levels' to radar reflectivity (dBZ). This was simply done by considering the relation between levels, reflectivities, and rainfall rate from Météo-France (Figure 3.2).

Niveau Radar (sans unité)	Réflectivité (dBz)	Intensité (mm/h)
0	inf. à 8 dBz	inf. à 0.2 mm/h
1	8 <= R < 16	0.2 <= I < 0.4
2	16 <= R < 20	0.4 <= I < 0.6
3	20 <= R < 21	0.6 <= I < 0.7
4	21 <= R < 22	0.7 <= I < 0.9
5	22 <= R < 23	0.9 <= I < 1.0
6	23 <= R < 24	1.0 <= I < 1.2
7	24 <= R < 25	1.2 <= I < 1.3
8	25 <= R < 26	1.3 <= I < 1.5
9	26 <= R < 27	1.5 <= I < 1.8
10	27 <= R < 28	1.8 <= I < 2.1
11	28 <= R < 29	2.1 <= I < 2.4
12	29 <= R < 30	2.4 <= I < 2.7
13	30 <= R < 31	2.7 <= I < 3.2
14	31 <= R < 32	3.2 <= I < 3.6
15	32 <= R < 33	3.6 <= I < 4.2
16	33 <= R < 34	4.2 <= I < 4.9
17	34 <= R < 35	4.9 <= I < 5.6
18	35 <= R < 36	5.6 <= I < 6.5
19	36 <= R < 37	6.5 <= I < 7.5
20	37 <= R < 38	7.5 <= I < 8.6
21	38 <= R < 39	8.6 <= I < 10.0
22	39 <= R < 40	10.0 <= I < 11.5
23	40 <= R < 41	11.5 <= I < 13.3
24	41 <= R < 42	13.3 <= I < 15.4
25	42 <= R < 43	15.4 <= I < 17.8
26	43 <= R < 44	17.8 <= I < 20.5
27	44 <= R < 45	20.5 <= I < 23.7
28	45 <= R < 46	23.7 <= I < 27.3
29	46 <= R < 47	27.3 <= I < 31.6

Niveau Radar (sans unité)	Réflectivité (dBz)	Intensité (mm/h)
30	47 <= R < 48	31.6 <= I < 36.5
31	48 <= R < 49	36.5 <= I < 42.1
32	49 <= R < 50	42.1 <= I < 48.6
33	50 <= R < 51	48.6 <= I < 56.2
34	51 <= R < 52	56.2 <= I < 64.8
35	52 <= R < 53	64.8 <= I < 74.9
36	53 <= R < 54	74.9 <= I < 86.5
37	54 <= R < 55	86.5 <= I < 99.9
38	55 <= R < 56	99.9 <= I < 115.3
39	56 <= R < 57	115.3 <= I < 133.2
40	57 <= R < 58	133.2 <= I < 153.8
41	58 <= R < 59	153.8 <= I < 177.6
42	59 <= R < 60	177.6 <= I < 205.0
43	60 <= R < 61	205.0 <= I < 236.8
44	61 <= R < 62	236.8 <= I < 273.4
45	62 <= R < 63	273.4 <= I < 315.8
46	63 <= R < 64	315.8 <= I < 364.6
47	64 <= R < 65	364.6 <= I < 421.1
48	65 <= R < 66	421.1 <= I < 486.2
49	66 <= R < 67	486.2 <= I < 561.5
50	67 <= R < 68	561.5 <= I < 648.4
51	68 <= R < 69	648.4 <= I < 748.8
52	69 <= R < 70	748.8 <= I < 864.7
53	>= 70 dBz	>= 864.7 mm
255	Pas de mesure	Pas de mesure

Fig. 3.2.: Correspondence between levels, radar reflectivity, and rainfall rate (Pers. Comm. Météo-France).

3.1.2. German radar network

The German radar composites for the period 2005 to 2014 used in this study were provided by the German Weather Service (DWD), which operates a network of 17 C-band radar systems in Germany as of 2016 (see Figure 3.3). As the radar detection radius for each station reaches 250 km and a maximum distance of 200 km separates the radar stations, the extensive overlap of the detection areas permits almost a complete coverage of the German territory. Only some edges of Germany remain as a gap in the composite, for example, in the far north near the Danish border (Figure 3.3). In Southern Germany, weather radars are preferably located on hills and mountain summits to minimize shading effects induced by the orography.

The installation of the German radar network started in 1994 with the objective to detect precipitation, especially heavy precipitation events. Since 2010, the network has been renewed and improved progressively. Dual-polarized radars have replaced all radars. During the exchange phases, individual devices were temporarily disconnected. In most cases, second radars were temporarily in operation, but some data gaps resulted. For example, no data is available for the radar of Neuhaus throughout 2011. During the same year, the radar of Essen was also renewed, but no gaps remained in the data (Puskeiler, 2013). Therefore, the data used in this work have some failures, but the overlap of detection areas permits filling missing data to obtain satisfactory results. In 2012, the station of Memmingen was added to the network. Three more radars were added to the German network in 2014, located in Boostedt, Isen, and Prötzel to replace the urban stations of Hamburg, Munich, and Berlin. The renewal of radars also marks a change in the scanning strategy with the implementation of dual-polarization on 16 stations (DWD, 2011).

The elevation angles depend on the orography and the altitude of each radar site and are between 0.5° and 1.8° (Bartels, 2005). Errors in the precipitation scans are eliminated by using a Doppler filter. The spatiotemporal resolution of the composite is the same as the French national composite, namely 1×1 km^2 for the spatial resolution and a 5 minutes time interval. Moreover, the same period (2005 to 2014) is chosen as for France, Belgium, and Luxembourg allowing for homogenization, and, thus, the merging and intercomparison of both datasets.
The encryption of each scan of the DWD network entails raw precipitation values in so-called RVP6 units. The conversion from RVP6 to dBZ is performed by:

$$dBZ = \frac{RVP6}{2} - 32.5 \qquad [3.1]$$

The accuracy of RVP-6 units is 0.5 dBZ in the range from 0 to 255. This corresponds to a reflectivity from -32.5 to 95 dBZ. By using these units, negative dBZ values occur, which can be neglected for precipitations (Bartels et al., 2004). The significant advantage of these data is certainly the high resolution enabling proper identification of hail streaks.

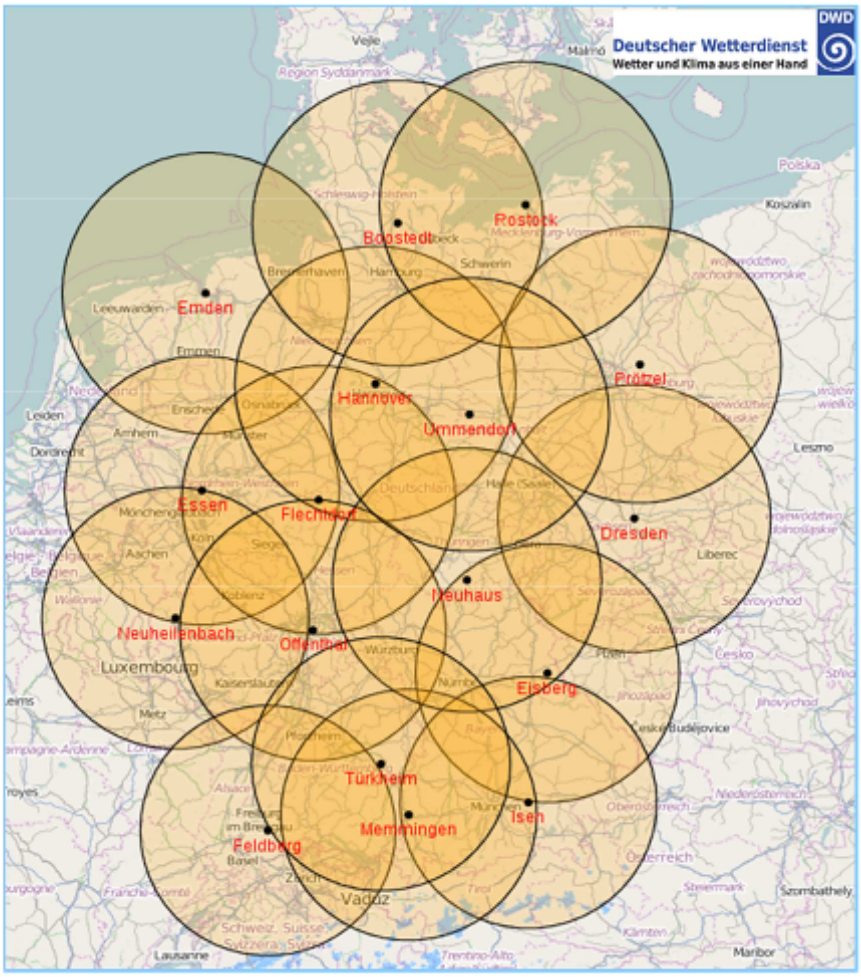

Fig. 3.3.: German radar network. Black dots are radar stations and circles represent a radar range of 200 km diameter (DWD, 2011).

The German radar composite includes an equidistant field size of 900×900 km^2 covering the whole of Germany as well as the northeastern part of France. The coordinate system of the national composite prevails in a polar stereographic projection so that each grid box in the projection is equidistant at 1.0 km. The projection plane intersects the globe at $\phi_0 = 60.0°$N and is parallel to the $\lambda_0 = 10.0°$E meridian. The central point of the composite is referred as $\lambda_m = 9.0°$N and $\phi_m = 51.0°$N (Figure 3.4). An earth radius of 6,370.04 km is used in this reference system.

Using the following equations, the geographic reference points (λ and ϕ) are converted into individual grids in the corresponding Cartesian coordinates of the stereographic projection:

$$x = R \cdot M(\phi) \cdot \cos(\phi) \cdot \sin(\lambda - \lambda_0) \quad [3.2]$$

$$y = -R \cdot M(\phi) \cdot \cos(\phi) \cdot \cos(\lambda - \lambda_0) \quad [3.3]$$

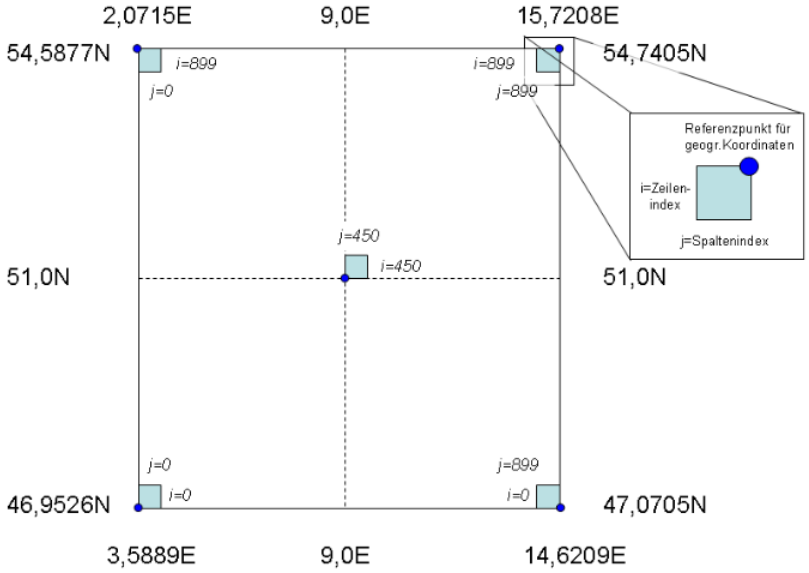

Fig. 3.4.: Coordinate system of the radar products provided by the DWD (DWD, 2011).

where (x, y) are distances to the North Pole in the Cartesian coordinate system and $M(\phi)$ is a stereographic scaling factor defined as:

$$M(\phi) = \frac{1+\sin(\phi_0)}{1+\sin(\phi)} \qquad [3.4]$$

Using these equations, the corners of the RADOLAN domain are obtained and given in Table 3.1.

Tab. 3.1.: Corners of the composite in both reference systems (DWD, 2011).

Corners coordinates	λ	ϕ	x	y
bottom left	3.5889°E	46.9526°N	-523.4622	-4658.645
bottom right	14.6209°E	47.0705°N	376.5378	-4658.645
up right	15.7208°E	54.7405°N	376.5378	-3758.645
up left	2.0715°E	54.5877°N	-523.4622	-3758.645

The DWD registers reflectivity values as binary data for storage facilities. A specific program provided by DWD is used to calculate reflectivity values and also to obtain a graphical representation for the 900 $\times$ 900 km^2 composite.

The combination of the radar networks of France and Germany covers a large area in Europe (Figure 3.5) extending around 940,000 km^2.

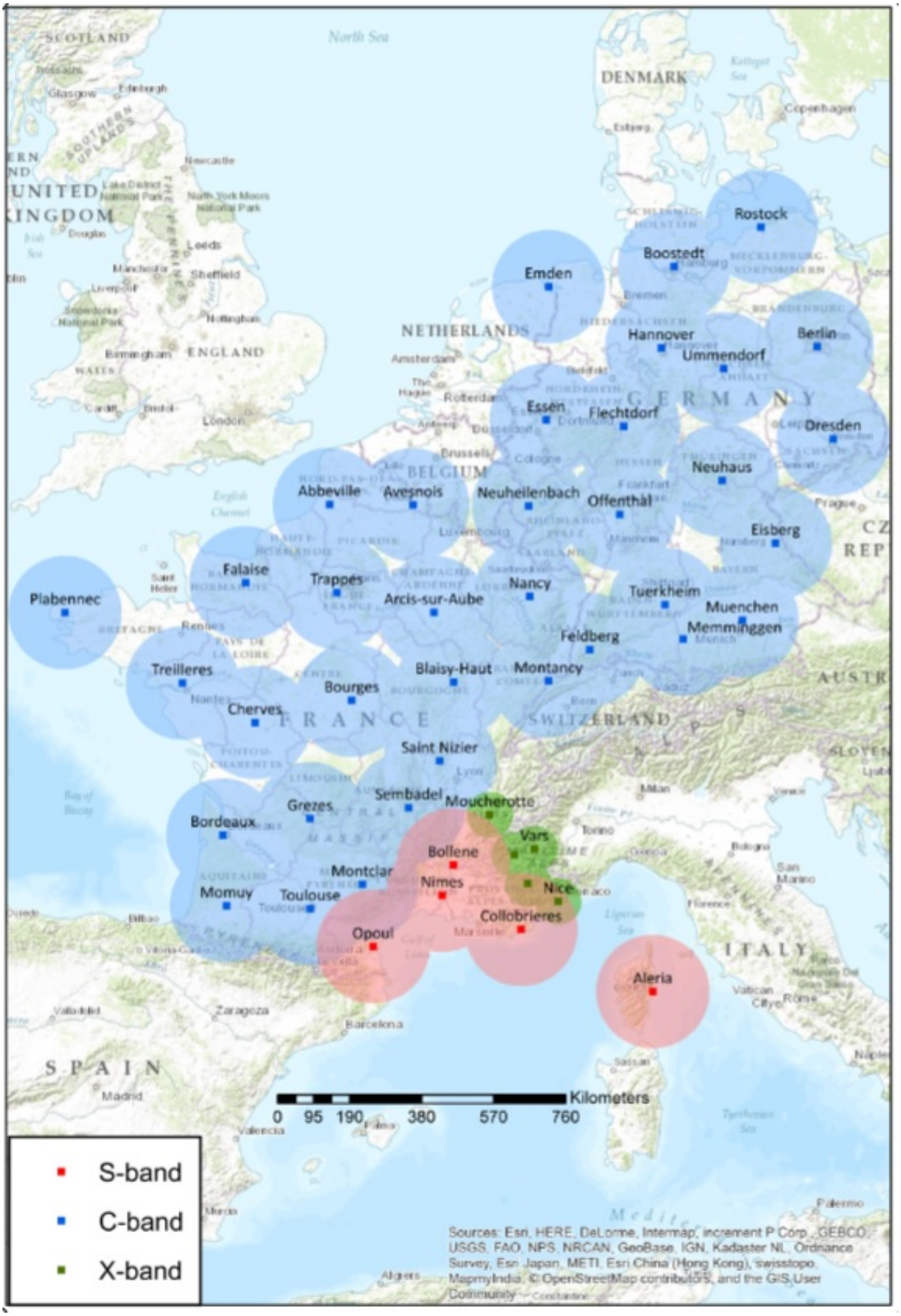

Fig. 3.5.: Location of radar stations used in this study. S-band and C-band radars have a radius of 150 km, whereas X-band radar radius equals 60 km.

Uniform European Grid

To project all radar data on a same spatial grid for analyzing hail frequency, a uniform European grid was created by the reinsurance company Tokio Millennium for the project Hail Model by Tokio Millennium for Europe (HAMLET). The grid resolution follows those of the national radar network of 1 $\times$ 1 km^2. The grid covers entire metropolitan France, Belgium, Netherlands, Luxembourg, Switzerland, and Germany (Figure 3.6) with the standard coordinate system and the standard spheroidal reference surface defined by the World Geodetic System elaborated in 1984 (WGS84). The grid is rectilinear in latitude and longitude with an equidistant spacing dLon in the zonal direction (dLon = constant). In the center of Europe at about 47 °N, the meridional grid spacing dLat is equal to dLon to minimize the grid distortion over Europe.

After the interpolation of the hail signals of France, Belgium, Luxembourg, and Germany on the HAMLET grid, all subsequent analysis and statistics were performed on this HAMLET grid. The radar data described above serve as input data for a tracking algorithm (see Section 3.2.3) that calculates potential hail tracks and reconstructs past hail streaks.

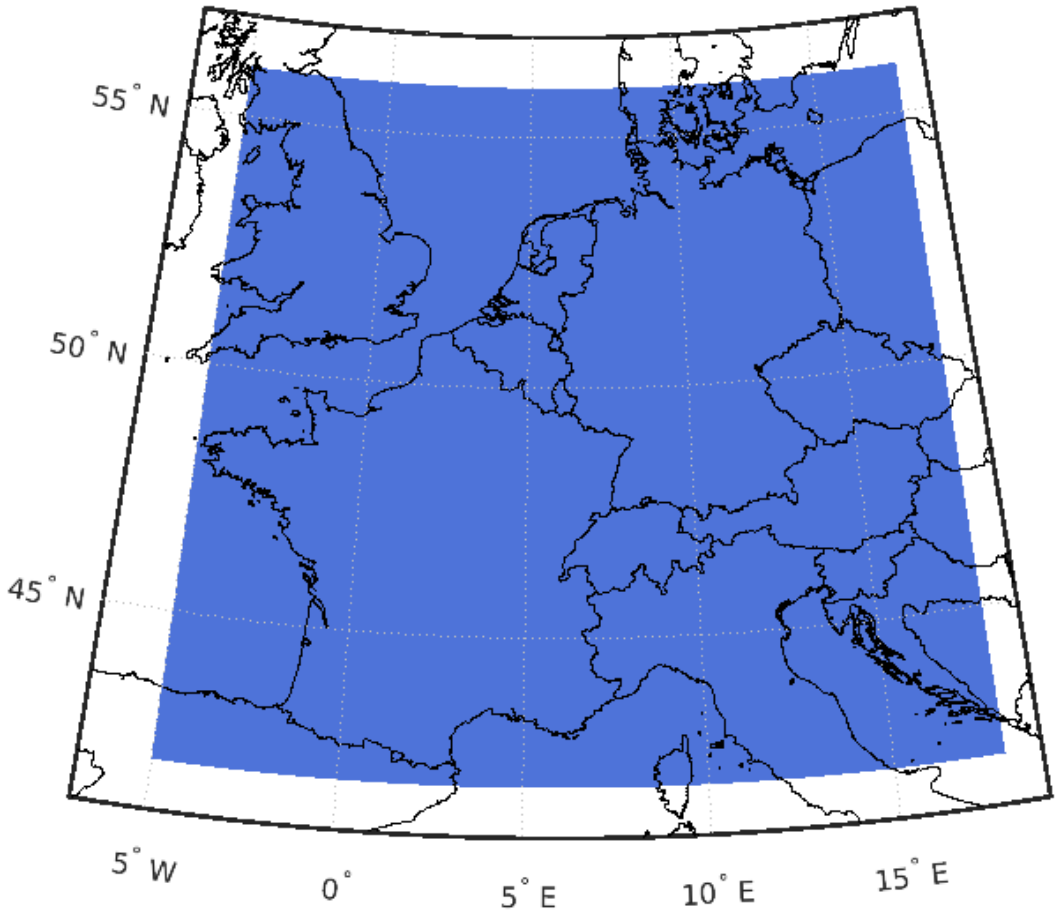

Fig. 3.6.: Domain of the HAMLET grid (blue area) with a resolution of 1 $\times$ 1km^2.

3.1.3. Lightning data

For the detection of hailstorms, we also used lightning data to filter the raw radar datasets for France, Germany, Luxembourg, and Belgium. Several authors showed an indirect relationship between the location of lightning flashes and the presence of hail on the ground. For example, Changnon (1993) found that the center of investigated lightning typically developed 9 minutes before hail occurred in an area of 5 km^2 in the Midwest of the USA, suggesting that the first lightning occurs during the growth of hailstones in clouds. He also found that the hailstorm's severity is associated with the flash rate and that the center of hail streaks are more affected by flashes than surrounding areas. Rust et al. (1981) showed an increase in the number of flashes for supercells in the Great Plains. Conversely, Soula et al. (2004) found low CG-rates for hailstorms compared to heavy rainstorms in the southern part of Europe.
Météorage (French Lightning Information) archives lightning data for France, Luxembourg, and Belgium since 1987 (Pédeboy, 2015). BLIDS (Blitz Informationdienst von Siemens) has produced a lightning detection system for Germany since 1990. The European Cooperation, EUCLID (European Cooperation for LIghtning Detection), archives all national lightning networks of the involved countries. The main mission of EUCLID is to provide high-quality homogeneous lightning data for 27 European countries based on 149 sensors (Schulz, 2016). Since 1994, the time of lightning occurrences has been provided from the Global Positioning System (GPS) satellite data and thus permits a high accuracy of the synchronization (Schulz, 1989). All sensors are operating in the same frequency range with an individually calibrated sensor to account for local conditions.

GPS-synchronized sensors record electrical activity in an area of 10 km^2 where the first stroke is recorded. Then, the strokes are grouped in flashes with an algorithm based on the distance of strokes and the distance to the strokes (Cummins et al., 1998). The total flash duration interval is limited to 1 s in the algorithm. The spatial accuracy of a flash location is 300 m. Once a sensor records a flash, an electromagnetic signal is automatically sent in real-time to the EUCLID service operations center in Austria at ALDIS (Austrian Lightning Detection and Information System), leading to a complete picture of lightning activity in real time. Since 1998, an upgrade of the sensors has permitted to separate each stroke into a flash so that each stroke location can be recorded (Pédeboy, 2015). The EUCLID coverage ranges from Sicily in the south to Norway in the north and from Spain in the west to Poland in the east.

Lightning data used in this study include information about the location of an impact point (latitude and longitude) and the event time to filter out unreliable radar signals. An examination of the past total number of days with thunderstorms from 2005 to 2013 (Mohr et al., 2016) demonstrates a high spatial variability of thunderstorm days in Europe (Figure 3.7). In this figure, an extended maximum appears in the eastern part of Austria as well as for the canton of Tessin in Switzerland (> 15 days with thunderstorms). Some smaller maxima appear near high or low mountain ranges, such as the Alps, along the Pyrénées, near the Swabian Jura in Germany or near the south part of the Alps and the Jura in France.

An overall coast-to-continental gradient can be recognized and partly explains the increase of days with thunderstorms with longitude. A north-to-south gradient can be noticed in Germany where the number of thunderstorm days substantially increases towards the south. Van Delden (2001) pointed out that these high activities can be explained by the warm and moist air from the Mediterranean that is advected over the Gulf of Genoa and the Po Valley in Italy meeting colder air from the Alps. These unstable conditions can lead to widespread thunderstorms. Other regions frequently affected by thunderstorms (> 13 days with thunderstorms) are situated in the Pyrenees, in the region of Haute Provence in Southeastern France, and in South Bavaria in Germany. Despite the high convective activity surrounding the Alps, the northern part of Western Europe, including Brittany, Normandy, and the German coastlines is low in thunderstorm activity with a frequency less than 0.6 per year.

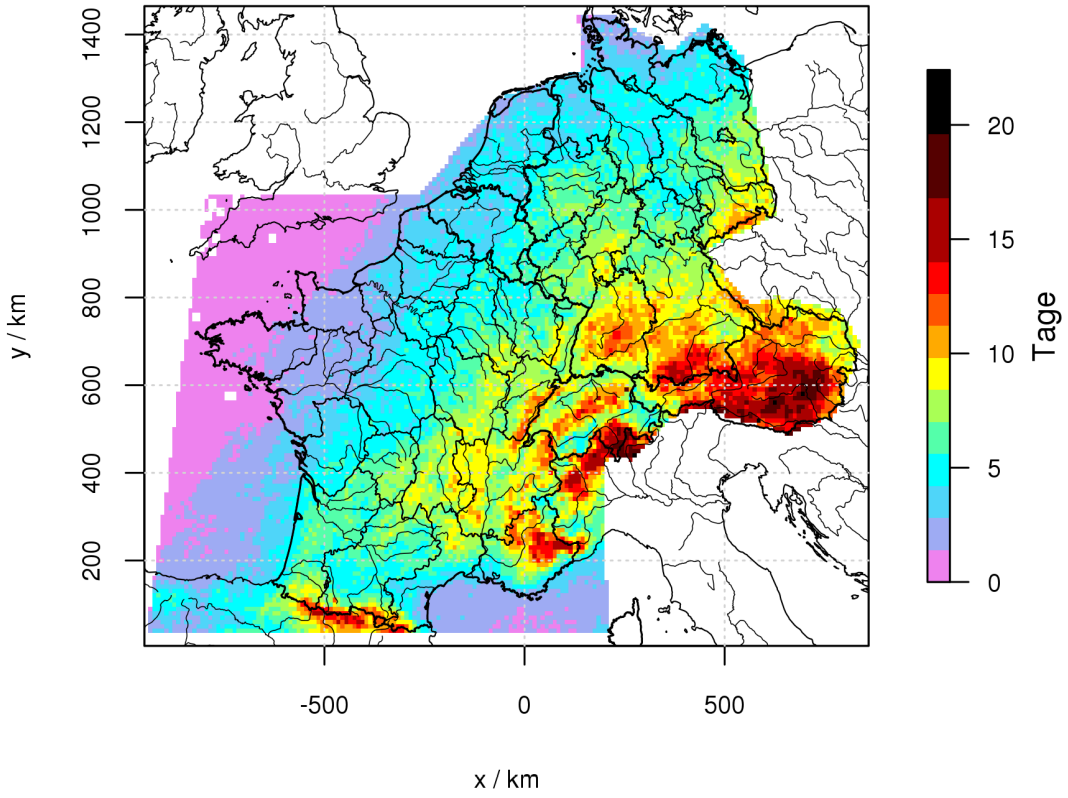

Fig. 3.7.: Annual number of days with thunderstorms within a 10 × 10 km^2 area during 2005-2013. A day with a thunderstorm is a day where lightning occurs during the summertime from April to September (Mohr et al., 2016).

In the present work, CG-lightning is considered (see Section 2.3) as the IC-lightning is not adequately detected with the existing devices. However, in mid-2012, the measurement method changed so that such flashes are also accurately identified (Thern, 2012 Pers. Comm). Even though data are available since 1992, a consistent coverage was only ensured since 2001, when a conversion of the detectors was performed.

3.1.4. Hail observations from the ESWD

The European Severe Weather Database (ESWD) operated by the European Severe Storm Laboratory (ESSL) aims to collect eyewitness reports of severe weather events endangering people in Europe, such as tornadoes, large hail, floods or severe wind gusts (Dotzek et al., 2009). These observations contain valuable information about the event, such as the location of severe weather, the time, and the related intensity. Hail reports contain hailstone diameters that are the only available measure of hailstorm intensity. The hail observations also confirm the presence of hail along a hail swath.
The ESSL was founded in 2002 (Dotzek, 2003) and formally established in 2006 to fill the lack of data on convective events. The database covers all European countries as well as Turkey and the Middle Eastern countries situated along the Mediterranean Sea and North African countries. The database extends backward in time until the 19th century (Dotzek, 2003). Although many European countries are involved in the ESSL, Germany counts the highest number of reports (23% of the overall database at 60,000 individual reports in 2014 according to Groenemeijer, 2014) and, thus, severe weather is better covered in this country compared to other countries (Figure 3.8).

Anyone can submit a report to the ESWD. However, primarily storm chasers or weather engineer associations, such as Keraunos in France, contribute observations to the online database. Since 2008, some quality control criteria (QC) have been in place regarding the reported events. QC levels permit to estimate the reliability of a report and the location of a submitted severe weather report and help to

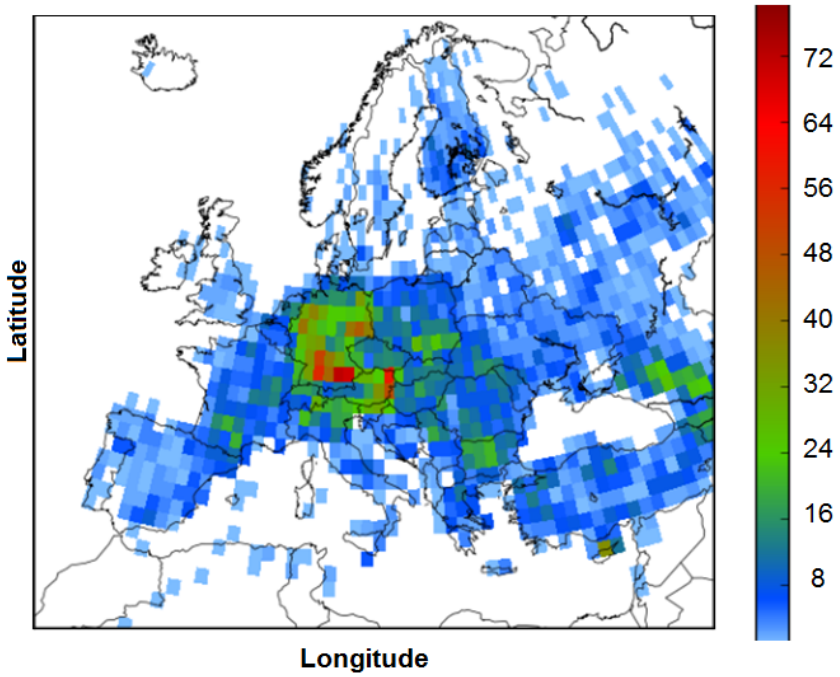

Fig. 3.8.: Spatial distribution of large hail reports from 1979 to 2014 per 1 $\times$ 1° box (Groenemeijer and Kühne, 2014).

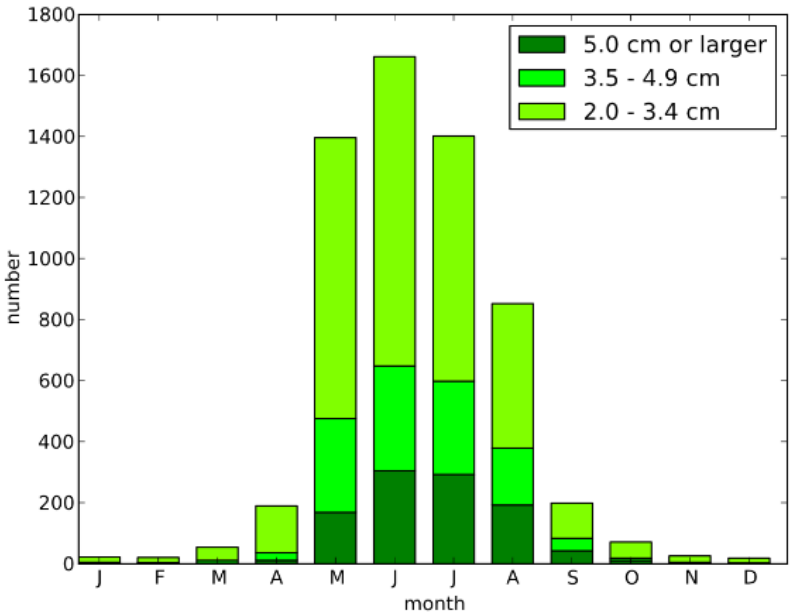

Fig. 3.9.: Monthly distribution of large hail from 1950 to 2012 according to the ESWD (Groenemeijer and Kühne, 2014).

manage the merging of multiple reports. At present, four QC levels exist (Dotzek et al., 2009):

- QCO: lowest level of confidence, where reports appear as received.
- QCO+: plausible check by ESSL or partners.
- QC1: reports confirmed by reliable sources, such as conclusive photos, newspapers, articles or certified by storm-chasers.
- QC2: fully verified reports, where all information about an event are verified and are consistent with reliable sources.

In this study, we only considered QC0+, QC1, and QC2 reports to minimize errors. Note that even for QC0+ and higher levels, several uncertainties remain, such as an incorrect timing event, a wrong location or a wrong intensity of the storm reported by the observer (not everyone perceives a storm in the same way).

Overall, as shown in Figure 3.9, large hailstones (> 2 cm) between 1950 and 2012 occurred with a characteristic monthly distribution.

A maximum appears during summertime in June for all hail sizes. The frequency of smaller hail (< 3.5 cm) is much higher than that of hail larger than 5 cm. Such statistics will be compared to the hail potential based on remote-sensing data, and individual report locations will give an idea about hailstone sizes and, thus, the intensity of single events. These locations also confirm the presence of hail along hail swaths detected by the tracking algorithm.

3.1.5. ERA-Interim reanalysis

ERA-Interim datasets consist of archived reanalysis computed by ECMWF (European Center for Medium-Range Weather Forecasts). A meteorological reanalysis is data assimilation of historical observations (e.g., radiosonde, satellites, and radar data) spanning an extended period. It provides a multivariate, spatially complete, and coherent record of the global atmospheric circulation. ERA-Interim reanalysis is available from 1979 to present (Dee et al., 2011) four times a day (at 00, 06, 12 and 18 UTC) with a resolution of 0.75° latitude by 1° longitude (representing approximately 79 km on a Gaussian grid), and integrates 60 vertical model-levels. The dataset comprises of more than 130 meteorological parameters. In this study, the following parameters are selected because of their relevance to convection development: CAPE, wind shear, potential temperature at 850 hPa, vorticity, and temperature advection at 500 hPa and 850 hPa (see Chapter 1). Since the height of the freezing-level (htf) is not available in the database, it was approximated by the zero crossings in the temperature between 950 hPa and 500 hPa. Harris et al. (2000) already used the same method in the NCEP reanalysis to identify the altitude of the 0°C isotherm:

$$htf = h(k,f1) + [h(k,f2) - h(k,f1)] \times \frac{[t(k,f1) - tref]}{t(k,f1) - t(k,f2)} \quad [m] \qquad [3.5]$$

where f2 is the index of the minimum detected in the temperature profile, f1 = f2-1, k is a loop iterating over the contents of f2, and tref = 273.15°K.

3.2. Methods

3.2.1. Data processing

Radar data contains noise and systematic errors that had to be eliminated by various approaches. Errors concern mostly individual grid points with significant reflectivity (e.g., more than 70 dBZ) compared to the surroundings. These errors frequently appear near the Atlantic coastlines or near the Baltic sea (Puskeiler, 2013) due to ship traffic. Since this study only considers reflectivity over the continent, clutter caused by ships can be neglected. Some high reflectivity values are also present in the older mosaic products, especially before 2001 around radar stations in France. To avoid this problem, the only reflectivity in the range of 35 to 70 dBZ are considered. A verification and correction filter was applied to individual values superior to 45 dBZ: when an individual grid point has a significantly higher value (difference greater than 5 dBZ) compared to all its surrounding within a range of 2 km, its value Z(x,y) is set to the average of the surrounding grid points (Puskeiler et al., 2016) as follows:

$$Z(x,y) = \frac{1}{8}\left(\sum_{i=-1}^{1}\sum_{j=-1}^{1} Z(x+i,y+j) - Z(x,y)\right)$$

[3.6]

This equation was applied on consecutive radar scans. When high reflectivity only occurred during a single time step and not in the product before or afterward, they were considered as artifacts and removed. As French mosaics before 2001 contained recurrent and extended ground clutter errors and spikes, the use of this filter remains, however insufficient, and large areas on the final composite possess high reflectivity, especially in the northeastern part of France. Furthermore, the low number of available datasets before 2001 led us not to use reflectivity mosaics during this period.

Concerning the homogenization between the French and German national composites, several corrections have already been performed from both meteorological services. For example, some French composites were calibrated by rain gauge datasets (Tabary, 2007). Reflectivity values near neighboring countries have been evaluated and calibrated with radar stations close to the border. The DWD and Météo-France calibrated their data on a regular basis and exchanged, for example, radar products within the frame of the European radar network OPERA project.

3.2.2. Lightning filter

Since hail occurs only in connection with thunderstorms, it can be assumed that lightning can be detected near a hail signal. Thus, the plausibility of radar products can be checked and corrected using lightning data. If high reflectivity occurs during a day without lightning, values are set to zero (Figure 3.10). A maximum distance of 10 km was chosen between a lightning discharge location and the grid point with high reflectivity. Distances of 5, 15, and 20 km were also tested, but a lightning filter of 5 km leads to a break of hail trajectories due to gaps in reflectivity values.

3.2.3. Convective cell tracking algorithm META

Several tracking algorithms were developed in recent years using different datasets. For example, Zinner et al. (2008) computed a severe convection algorithm, named Cb-TRAM, based on Meteosat-8 SEVIRI (Spinning Enhanced Visible and Infrared Imager) data, which is useful for nowcasting of single events. Kober and Tafferner (2009) applied Cb-TRAM on radar data to produce a radar tracker, rad-TRAM, for convective cell detection. More recently, Meyer et al. (2013) created an automated thunderstorm tracking algorithm for 3D lightning and radar data.
The Middle European Tracking Algorithm (META) is a convective cell tracking algorithm that reconstructs trajectories of convective cells based on radar data. This algorithm was first developed and optimized on 3D radar reflectivity from a single radar denoted as TRACE 3D (Handwerker, 2002) before to be adjusted on several radar stations. The original program was based on spherical coordinates around an individual radar station. Therefore, the algorithm was first adjusted on a Cartesian coordinate system computed by the DWD (Puskeiler, 2013). After that, the algorithm TRACE 3D was adapted to 2D radar

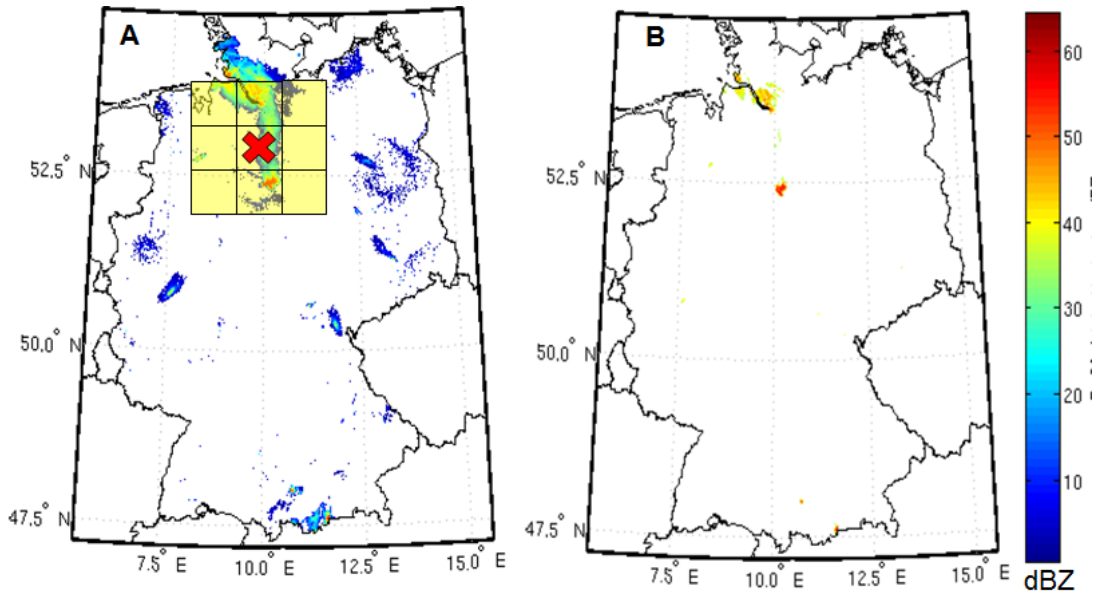

Fig. 3.10.: Radar reflectivity values on 27 July at 15:30 UTC before (A) and after (B) applying a lightning filter (fictive orange boxes) around a lightning discharge (red cross).

products by considering a unique elevation level and by enlarging the spatial domain of the algorithm. Some tests with long-living convective cells compared with ESWD hail reports along the reconstructed storm trajectories were performed to obtain a satisfactory tracking.

Two main steps are part of META: reflectivity cores identification on 2D radar composites (RC2s) and spatiotemporal tracking.

Input data

Data used for the algorithm are radar composites every 5 minutes including reflectivity filtered with lightning data (see Section 3.1.3). The algorithm was first tested and adapted for Germany with a surface of 900×900 km^2. Track outputs from TRACE 3D, using volumetric data, were available for Germany only from 2005 to 2011 (Puskeiler, 2013), and were compared with the tracks outputs from META. Tracks detection varies slightly between META and TRACE 3D. On average, shorter tracks were detected by 3D radar data compared to 2D radar data, possibly due to the presence of higher reflectivity in upper levels leading to an overestimation of convective cells at the ground. This slight overestimation was also observed by overlapping ESWD reports with TRACE 3D tracks for single events. Some short tracks were identified, but reports could not be assigned to the detected tracks, whereas tracks detected by META fit better with hail observations, even if a perfect match is not possible.

In a second step, META was adapted to the mosaic comprising France, Belgium, and Luxembourg. The area of 900×900 km^2 covered beforehand by the algorithm was extended about the dimensions of

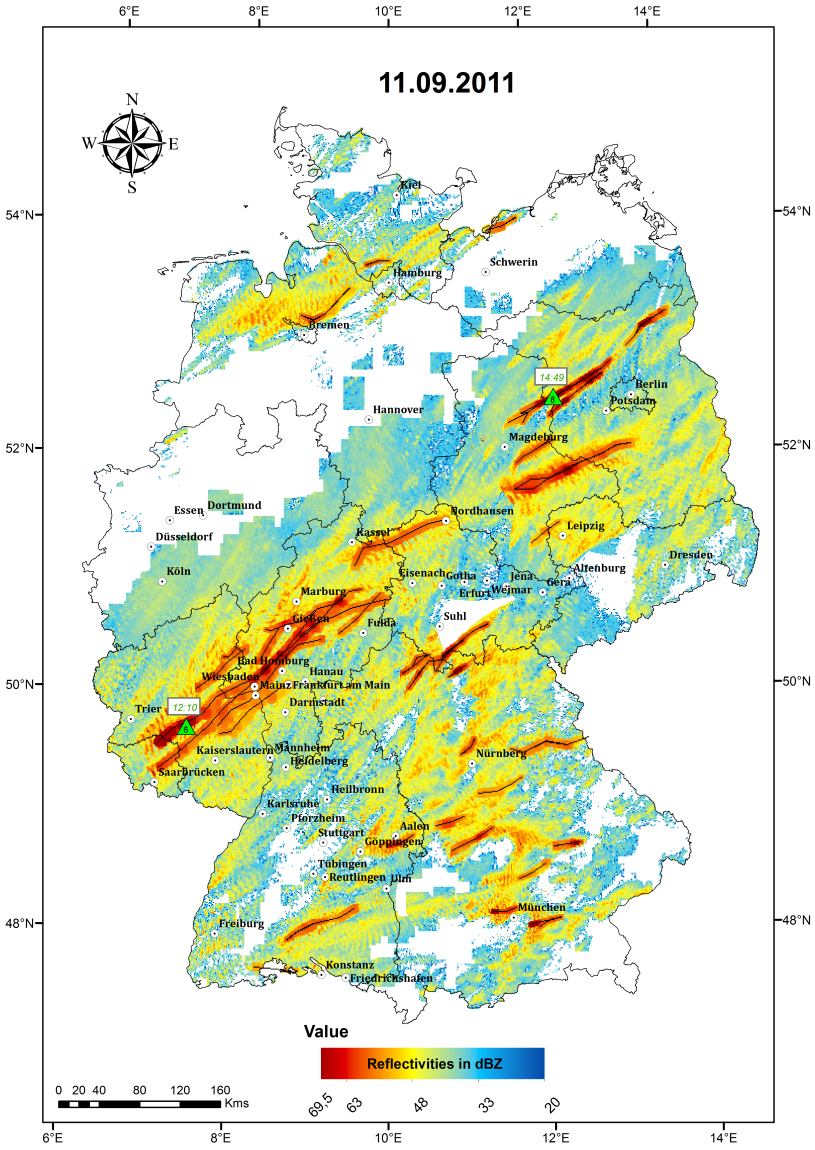

Fig. 3.11.: Tracks (black lines) detected by META overlay on radar reflectivity (colors) during hailstorms occurring on 11 September 2011 over Germany.

the national French composite to 1536 × 1536 km^2. As ESWD reports remain solely in these countries, only severe events were considered to test the accuracy of META. An example of track outputs detected on 11 September 2011 and combined with hail observations is shown in Figure 3.11.

Identification of RC2s

META only uses reflectivity values more than 55 dBZ to identify convective cells. Few reflectivity thresholds are used to identify individual cells. Otherwise individual cells with strong convection are undetectable. Fixed thresholds are already used to detect the core of a convective cell (Witt et al., 1998; Johnson et al., 1998).

Tab. 3.2.: Parameters for RC2 identification by META.

Description	Value	Units
Minimum reflectivity of a RC2	55	dBZ
Difference between the maximum reflectivity	10	dB
Maximum distance between two RCs centers that could merge	10	km
Maximum distance between two merged RC	1000	m
Minimum number of elements inside a RC	3	-
Minimum RC2 area	5	km^2
Fraction of RC2 area, which must have two minima at least	0.3	-

At first, the regions with reflectivity over 55 dBZ, named ROIP (region of intense precipitation), are detected in the radar composites. This threshold was chosen because convective cells may contain areas of precipitation associated with low reflectivity. Afterwards, the maximum of reflectivity values of each ROIP is computed. ROIP outlines follow the isopleth 6 dBZ beneath the respective ROIP maximum. Other thresholds between 5 and 10 dB were tested, but 6 dB was the most accurate to identify convective cells in this study. Figure 3.12 shows a process example of reflectivity core identification used in TRACE 3D with a minimum reflectivity of 35 dBZ and a difference beneath the maximum in an RC of 10 dB (Handwerker, 2002). The total range of reflectivity values located between the ROIP maximum and the threshold Max-6 dBZ within a maximal spatial extent of 10 km forms an RC.

Thresholds used for the identification of RC2s in this study are listed in Table 3.2.
All the above-listed criteria are stored along with:

- Near left corner position and RC2 size.
- RC2 center position, weighted with a logarithmic reflectivity that will be tracked.
- Radar data resolution in radial and azimuthal directions.
- Number of ROIP within an RC2.
- Date and time.

Tracking

After META detects RC2s in a space within a search radius that depends on cell velocities, the temporal aspect is considered. META assigns the RC2s of the former radar composite to the recent composite according to the expected velocity and position of the RC2.

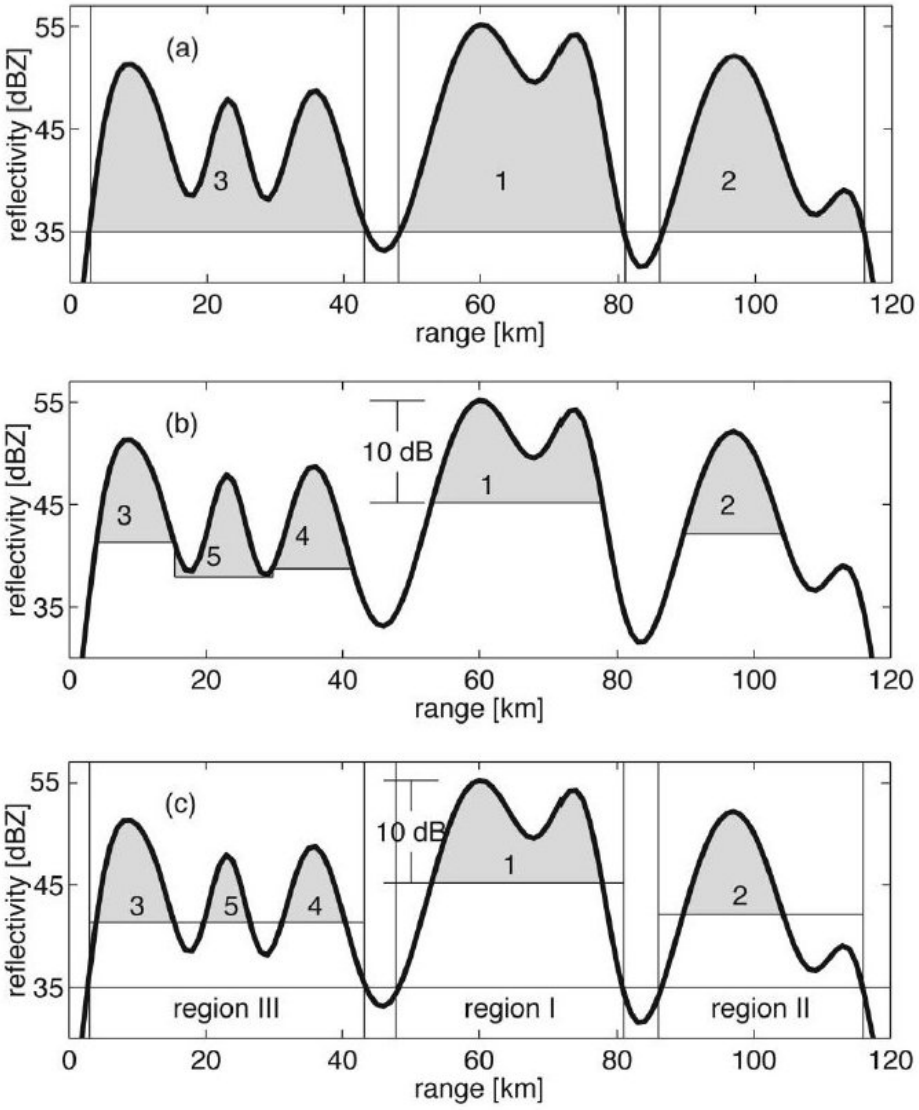

Fig. 3.12.: Processes leading to RC2 detection in regards of reflectivity values. a) At first, each element above the threshold 35 dBZ is part of an RC2. b) The upper 10 dB is taken as the RC2 limit, leading to cores, including the lower regions of more prominent RC2s. c) Contiguous regions with a threshold of 35 dBZ are identified. Within each region, the second threshold of 10 dB below the maximum is used to define RC2s. (Handwerker, 2002).

In this study, the time step between each radar scan is 5 minutes. If the time between two successive composites are in excess of 30 minutes, for example, and if no radar data are available, then the tracking is stopped during this time and restarted automatically when a complete radar composite appears. Thus, data at times $t - 2\delta t$ and $t - ($ is the time interval between two radar composites) are recorded as well as the storm position $\vec{r}t - 2\delta t$ and $\vec{r}t - \delta t$, where the velocity $\vec{v}$ is given by:

$$\vec{v}(t-\delta t) = \frac{\vec{r}(t-\delta t) - \vec{r}(t-2\delta t)}{\delta t} \qquad [3.7]$$

If an RC2 is tracked in more than one time step, then the estimated velocity results in the weighted sum of all former velocities. If no velocity is recorded, then the nearest RC2 of the next time step is assigned to be the successor of the first one. However, similarities between RC2s, for example, in intensity and size, from one time step to the next must exist in a search radius for accurate RC2 assignment and tracking. The search radius is given by the estimated distance of an initial RC2 displaced during a time step multiplied by a velocity factor of 0.6. Shorter time steps give a better allocation and, therefore, more precise trajectory reconstruction. An example of successful recognition by considering RC2 characteristics in the previous time step is shown in Figure 3.13.

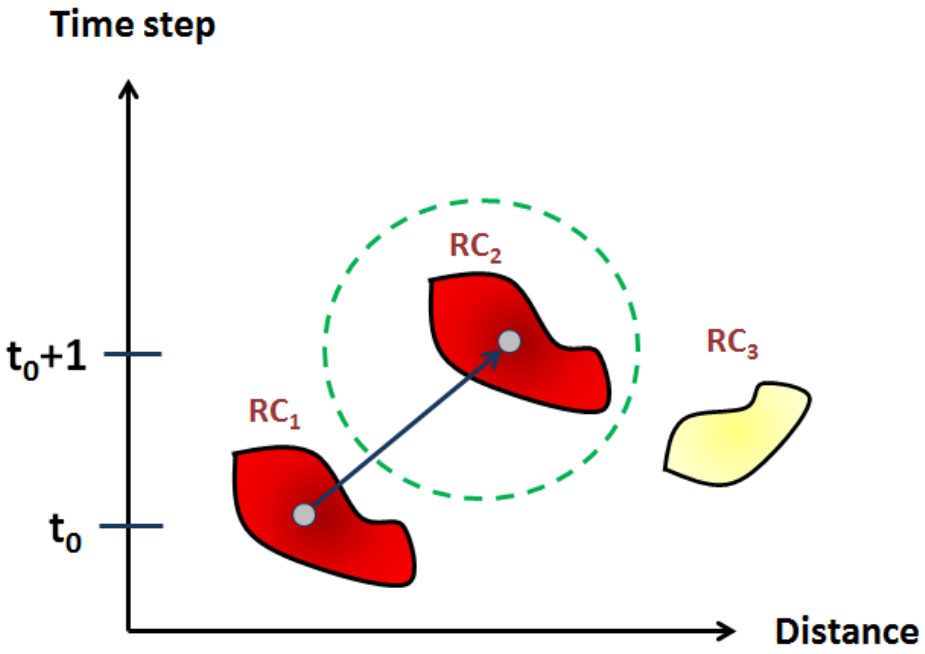

Fig. 3.13.: Cell-tracking with TRACE3D (modified from Handwerker (2002)). The green dotted circle represents the search radius between two time steps.

Special attention is given to cell splitting and merging. To detect a splitting, the complete initial RC2 is first displaced to the position of the successor, and the respective areas are compared. If the area of the successor differs significantly from the initial RC2, then a splitting occurs. In the case of merging, the opposite calculation to cell splitting is performed. Initial and successor areas are then compared, and the successor is placed at the weighted center of all initial detected cores. A merging occurs when the successor area is larger than the initial RC2.

To avoid reflectivity core crossings or overcrowding, each RC2 is enumerated separately and recorded. Table 3.3 summarizes typical characteristics recorded by META while tracking.

Tab. 3.3.: Tracking parameters for META.

Description	Value	Units
Next neighbor factor for search radius	0.5	-
Maximum time delay between two scans	1800	s
Minimum distance between two cells to remain separate	20	km
Maximal amount of grid points per RC taken for distance computing	200	-
Minimal distance for a split thunderstorm	3	km
Velocity factor for search radius	0.6	-

3.2.4. Advection correction on radar products.

For this study, daily maximum reflectivity is computed (1 km $\times$ 1 km) from accumulated national composites from 00 UTC to 23:55 UTC. The composite of maximum reflectivity on a day does not give a smoothed result, but more of a scattered product. This effect occurs when a cell travels further than its horizontal extent during a measuring interval. The faster the storm, the more the result is scattered. This can result in minimum reflectivity values between two scans, although a storm crossed the area with high intensity.

Therefore, this effect must be corrected to have the best storm intensity estimation possible. This is primarily important for the reconstruction of entire hail tracks and required parameters such as the total length of a track, the width, or spatial extension. These characteristics are also relevant for the input of a stochastic event set required for hail risk modeling.

To consider this effect, an advection correction is performed (Shapiro et al., 2010; Puskeiler et al., 2016). Advection in this sense is computed as a translation of reflectivity from one time step to the next considering the horizontal wind field estimated by META along a track. Horizontal wind components, as well as the track direction of a thunderstorm computed, are projected on the 900 $\times$ 900 km^2 German grid and the 1536 $\times$ 1536 km^2 French grid. Each point along a track includes a velocity shift-vector in the north-to-south (dv) or west-to-east (du) directions. The so-called shift-vector is denoted as:

$$\vec{U}(x,y) = \begin{pmatrix} du(x,y) \\ dv(x,y) \end{pmatrix} \quad [3.8]$$

As META only determines the center of a track, an n-time parallel duplication of the track is required with a vector field from all locations of the thunderstorm. The parallel shift on position (b,c) is done with normalized vectors $\vec{t}_1$ and $\vec{t}_2$ on the cell motion direction with a spacing of 20 km maximum on each side of the track. The position (b,c) obtained from the shift vector $\vec{U}$ is calculated as follows:

$$(b,c) = \left(x + |\frac{\delta \vec{t}_{1,2}}{\delta x}| \cdot n, y + |\frac{\delta \vec{t}_{1,2}}{\delta y}| \cdot n \right) \quad [3.9]$$

This gives a displacement field of the entire cell complex as shown in Figure 3.14.

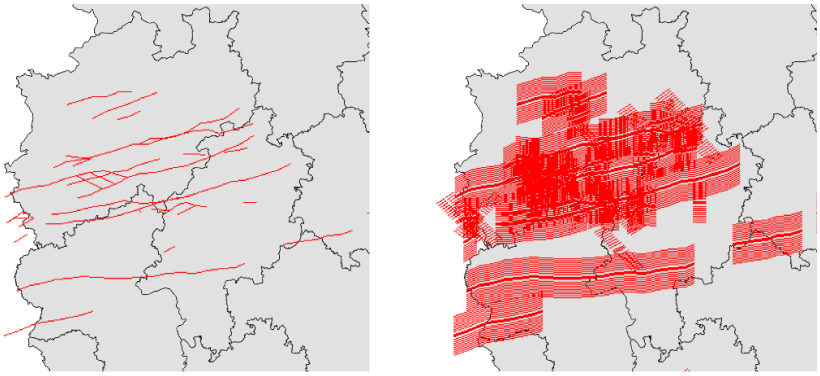

Fig. 3.14.: Tracks (red lines on the left panel) and related horizontal vector fields calculated by META (ensemble of red lines on the right panel) on 27 July 2005 in Germany (Puskeiler et al., 2016).

When a maximum reflectivity is detected along a generated track, the search for the next maximum in the same direction along the generated track is performed within a search radius r of approximately 4 km. Maximum reflectivities (dBZ_{max}) are averaged between two steps at the beginning and end of the shift vector and through the entire radius. During each step, the maxima are denoted as dBZ_{max1} for the first and dBZ_{max2} for the second. The correction of the reflectivity values along the track results in:

$$\mathrm{dBZ_{max}}(x+du\pm r, y+dv\pm r) = max[\mathrm{dBZ_{max}}(x+du\pm r, y+dv\pm r), \mathrm{dBZ_{max1}}] \quad [3.10]$$

$$\mathrm{dBZ_{max}}(x+2du\pm r, y+2dv\pm r) = max[\mathrm{dBZ_{max}}(x+2du\pm r, y+2dv\pm r), \mathrm{dBZ_{max2}}] \quad [3.11]$$

With these calculations, the scatter effect disappears and dBZ_{max} values are continually represented along the main track as can be seen in Figure 3.16 for several tracks on 15 July 2005.

3.2.5. Validation of radar products

A first approach to validate the presence of hail along detected hail swaths is to compare ESWD hail report locations on reflectivity. More than 100 single hail events were analyzed with this method. Figure 3.15 shows, for example, an overlay between reflectivity and ESWD on 17 June 2013. Reports are situated on high reflectivity along hail swaths, which attest to a conformity between hail observations and proxies.

Tokio Millennium Re is currently performing a stochastic hail event set for assessing hail risk for motor insurance, considering the diurnal cycle of traffic. Their model is created by randomizing relevant swath parameters obtained from the tracking approach of the historical event catalog (length, width, orientation, and duration). This stochastic event set will be used to quantify hail risk and to estimate probable maximum loss (e.g., PML200) for a given motor or property (building) portfolio. The reinsurance possesses some claims for Germany, France, Belgium, and Luxembourg for the period 2009-2015.

Primary work is to compare claim locations in Germany and France for past hailstorms on daily maximum reflectivity for single events. The first results show that claims are located where reflectivity is highest.

Maximum hailstone diameters estimated from ESWD (see Section 3.1.4) are interpolated along and close to individuals hail tracks giving an estimation of mean diameters for detected hail swaths. However, this method is limited and implies that only hail swaths corresponding to ESWD data contain hail. Furthermore, only a low number of ESWD reports are available (especially in France) and, thus, many hail swaths would be eliminated, suggesting an underestimation of the hail hazard.

3.2.6. Radar Convective Severity Index

To understand what makes a hailstorm extraordinary, we compare the intensities and spatial extent of elapsed hail swaths. Mahieu and Wesolek (2011) developed a severity index for thunderstorms in France based on four meteorological phenomena: hailstone diameter, downdraft velocity, tornado intensity (if existing), and precipitation rate. In the same concept, a new Radar Convective Severity Index (RCSI) is developed in this study and computed for each hail swath in the investigation area based on maximum radar reflectivity. The index was calculated for 10,183 hail swaths for the period 2005 to 2014.

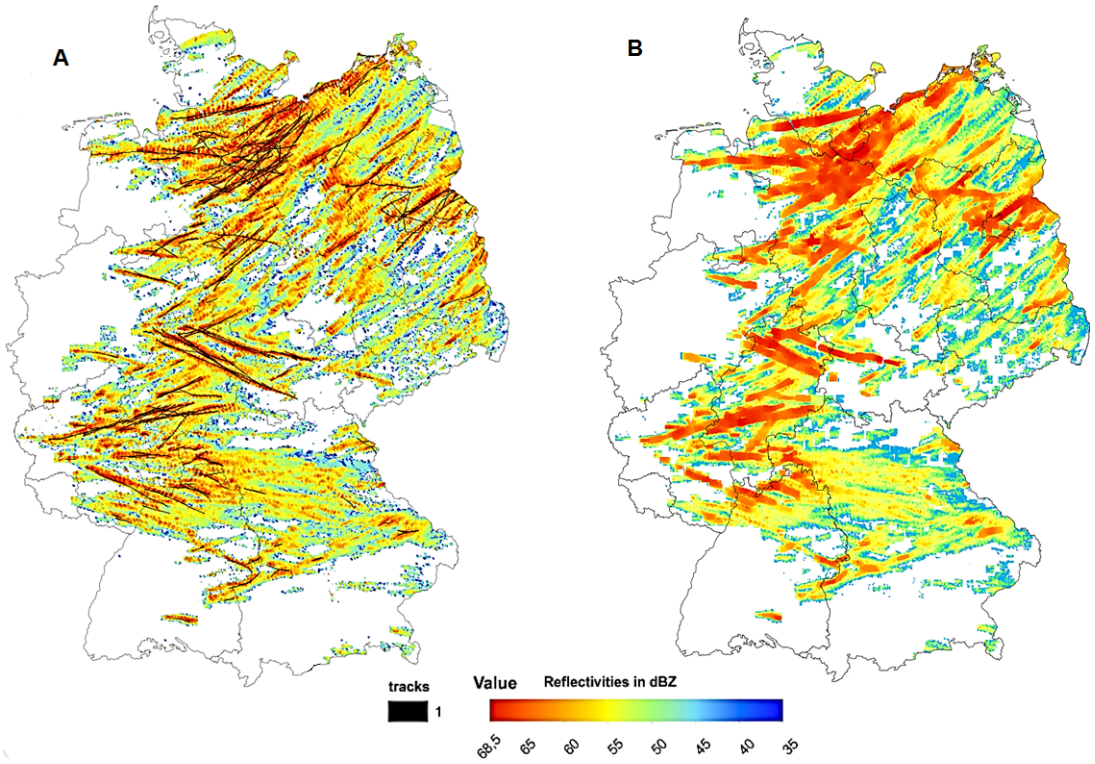

Fig. 3.15.: Convective cell tracks on 15 July 2005. Potential hailtracks calculated by META (black lines) overlapped on maximum reflectivity before (A) and after (B) the advection correction.

Maximum reflectivity within a hail swath are inputs for the index. A hail swath in this study represents an area of continuous reflectivity resulting from the advection correction (see Section 3.2.4) along with a hail track detected by META. In this way, the full spatial extent of a hail swath is considered. To avoid track crossings and overlapping, each track was recorded separately so that the total extent of a hail swath is considered. The maximum reflectivity, as well as a positive integer, were interpolated along each track with the horizontal wind fields. The indexing enumerates each hail swath per day and combines them with the respective reflectivity. Figure 3.17 shows an example of the hail swaths index (Id) locations over France, Belgium, and Luxembourg on 16 July 2013.

Each hail swath including reflectivity and index are interpolated on the uniform HAMLET grid of 1 by 1 km^2. The index was set to 1 and the rest of the grid to 0 so that a combination of the index and reflectivity result in a delimited swath with continuous data.

Finally, a severity index was computed for each swath, based on the flux energy $\dot{E}$ and the reflectivity factor Z. Waldvogel et al. (1978) computed the quantities $\dot{E}$ and Z from 175 hailstones (with a mean

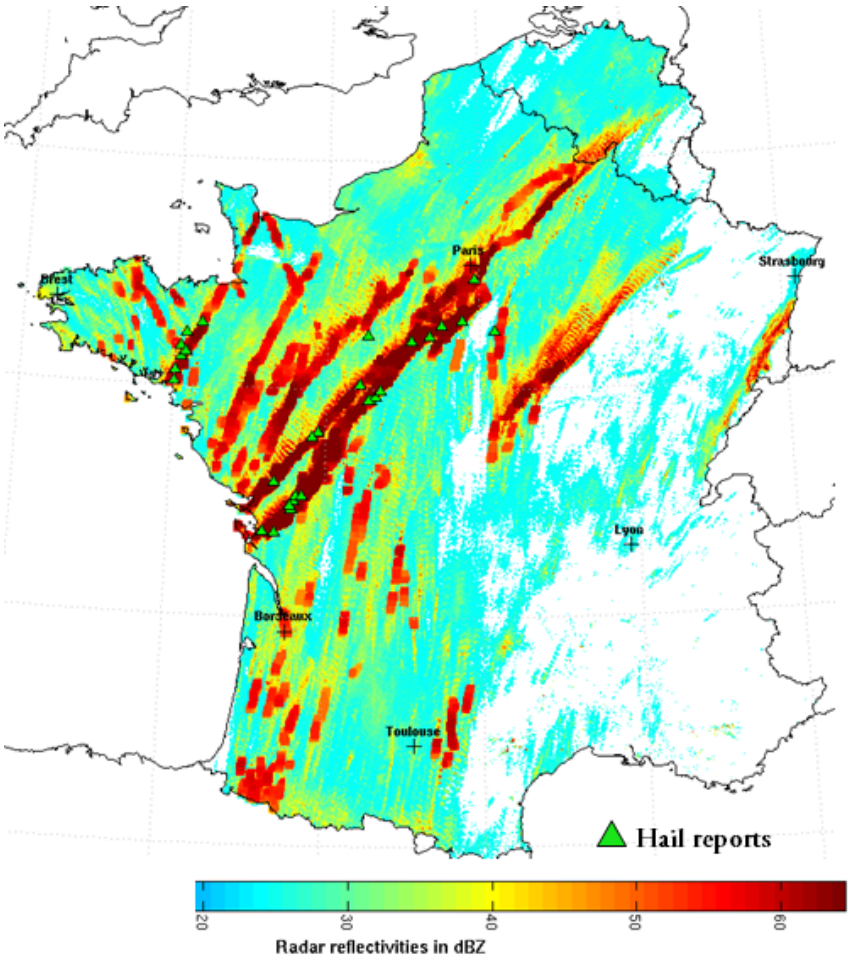

Fig. 3.16.: Radar composite showing daily maximum reflectivity on 17 June 2013. Reconstructed hail swaths depict high reflectivity values (red). ESWD hail reports (green triangles) from this day are overlayed on hail swaths.

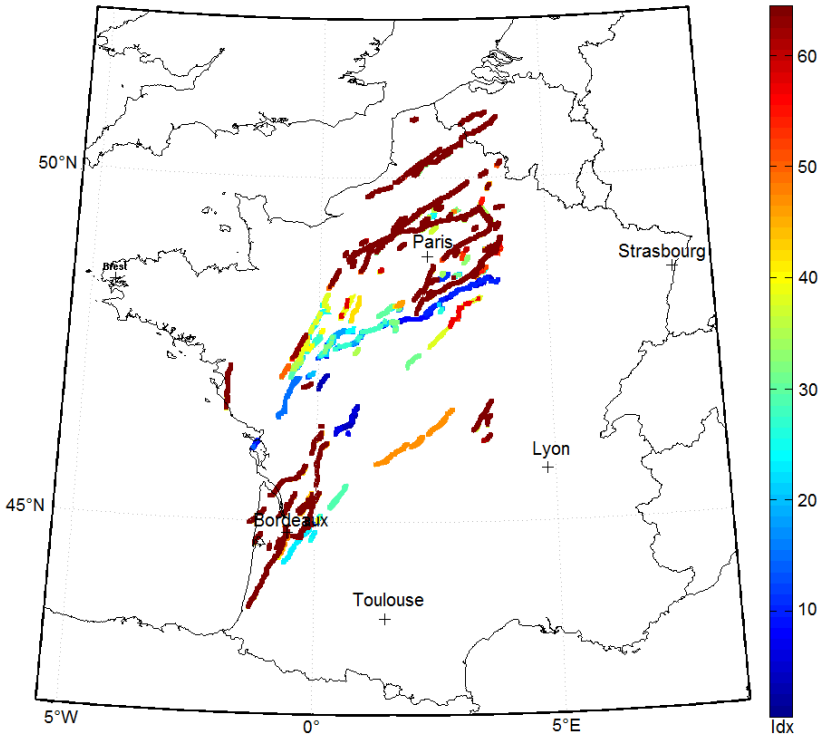

Fig. 3.17.: Numeration of hail swaths on 26 July 2013 in France and Belgium.

diameter D_i, a density ρ, and a fall velocity v) with size distributions measured with hailpads for four hailstorms in the USA at six sample sites. The equations for $\dot{E}$ and Z are computed as:

$$\dot{E} = \frac{\pi \rho v}{F_t 12 \cdot 10^6} \sum_{i=1}^{p} n_i D_i^4 \quad [\mathrm{J\,m^{-2}s^{-1}}] \qquad [3.12]$$

$$Z = \frac{1}{F_t v} \sum_{i=1}^{p} n_i D_i^{5.5} \quad [\mathrm{mm^6\,m^{-3}}] \qquad [3.13]$$

According to Waldvogel et al. (1978), the parameter n_i is the number of hailstones in the interval $D_i \pm \frac{1}{2}\Delta D$. 175 values of $\dot{E}$ and Z were computed for each hail spectra. Among them, 86 spectra with $\dot{E}$ > 0.1 were selected in the study of Waldvogel (1978a) for the relationship Z-$\dot{E}$. The diagram of the Z- $\dot{E}$ relationship with 86 data points is given in Figure 3.18.

The linear regression between Z and $\dot{E}$ from Figure 3.18 is generalized with the following equation:

$$\dot{E} = 5 \cdot 10^{-6} \cdot Z^{0.84} \quad [\mathrm{J\,m^{-2}s^{-1}}] \qquad [3.14]$$

For more convenience, reflectivity values of equation (3.14) are computed in decibels. RCSI represents, therefore, the sum of reflectivity included within an entire hail swath on a grid mesh of 1×1 km^2, and can be summarized by:

$$\mathrm{RCSI} = 5 \cdot 10^{-6} \cdot \sum_{k=1}^{n} (Z_k)^{0.84} \qquad [3.15]$$

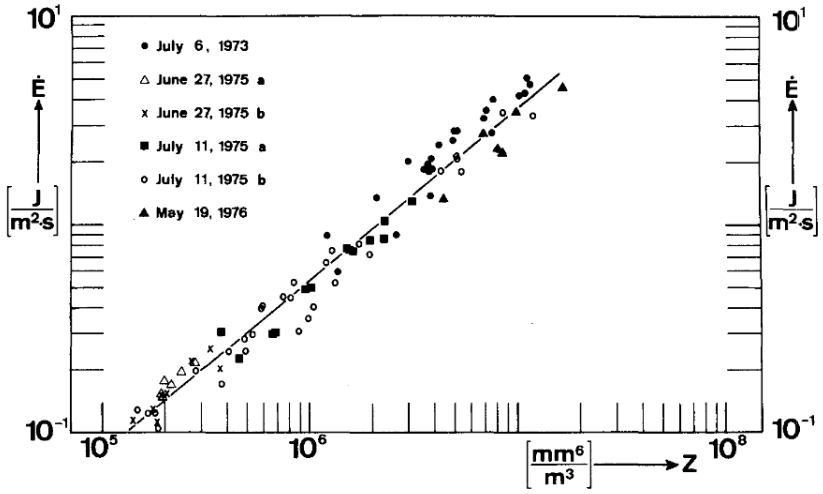

Fig. 3.18.: Scatter diagram of Z-$\dot{E}$ relationship on a logarithmic axis. 86 values of Z and $\dot{E} > 0.1$ J m^{-2} s^{-1} of hail spectra are represented from six samples sites during four hailstorms (Waldvogel et al., 1978).

where n is the number of grid boxes exceeding 55 dBZ for hail detection according to the Mason (1971) criterion.

A list of the most severe hail swaths as well as their physical characteristics can be found in Section 4.4. A hail swath occurring on 9 June 2014 crossing France towards Germany (and named Ela) was the most severe event ever recorded during the period 2005 to 2014.

All data processing steps, from the raw radar composite to the final product, are summarized in Figure 3.19.

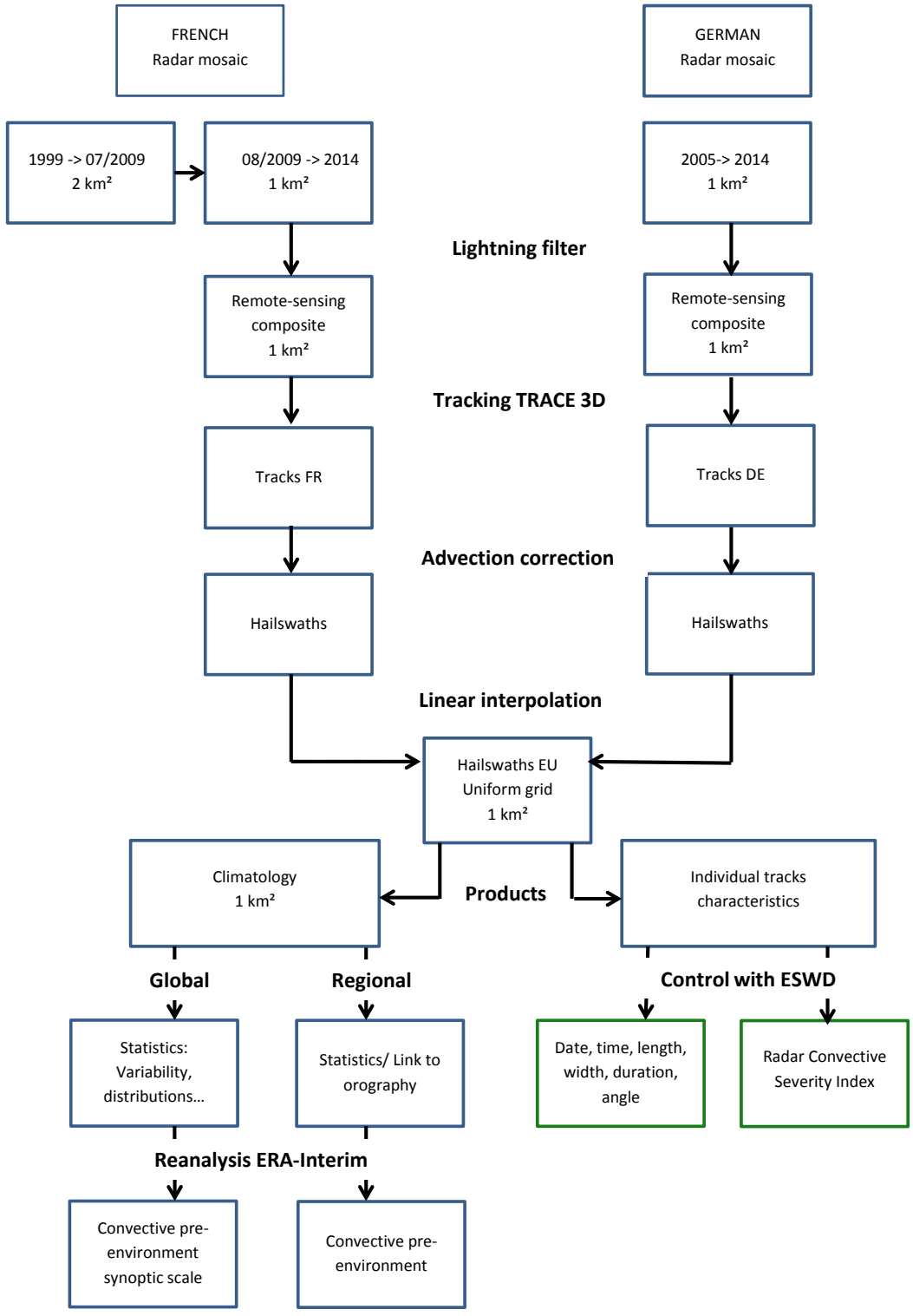

Fig. 3.19.: Data processing steps applied in this study.

4. Spatial and temporal distribution of hail events

In this chapter, 10 years of radar-based hail probability over France, Germany, Belgium, and Luxembourg are investigated. Regions highly affected by hail are highlighted, and temporal and spatial distributions of hail are examined with respect to orographic influences and prevailing climate conditions. The second part of this chapter describes physical characteristics of hail swaths and underscores dimensions of large hail events, which are most relevant for total damage.

4.1. Hail statistics between 2005 and 2014: overall results

4.1.1. Spatial distribution

Figure 4.2 presents the first hail probability map in terms of the number of hail days during the period 2005 to 2014 with a resolution of 1×1 km ^{2} based on 2D radar data. A day with hail is considered when the threshold of 55 dBZ is exceeded in the daily maximum reflectivity composite after correction, filtering with lightning data, and tracking with the META algorithm as described in Section 3.2.3. In the case of fulfilling the Mason (1971) criterion ($Z \geq 55$ dBZ) in the composite, the respective grid points are set to one while those below this threshold are counted as zero. The sum over the entire period yields the radar-based climatology. Sea areas were masked because only land areas are of interest, especially for the application to insurance property losses.

The variability of hail days is very large, but some patterns can be identified with hot spots. The area of most hail days is situated in central France on the northern flank of the Massif Central (Figure 4.1) accumulating up to 46 hail days during the period 2005 to 2014. Hail probability around the Massif Central will be further investigated in the next section.

Southwest France, including both regions Aquitaine and Midi-Pyrenees, is also particularly affected by hail. Some hot spots with up to 23 hail days can be recognized in the southeast of the region of Aquitaine as well as in the north of Aquitaine, whereas lowest hail potential is located along the coast. Furthermore, the highest hotspots with up to 25 hail days are in the east of Midi-Pyrenees at the southwestern edge of the Massif Central. Another pattern with up to 26 hail days is in the north of Midi-Pyrenees, which is the western border of Massif Central. The hail potential is very weak (around 2 hail days) on the summit of the Pyrenean mountain range. Aquitaine and Midi-Pyrenees are the two regions well known in the literature for a very high hail probability. Hail frequently occurs in the situation where a low-pressure system is situated over the western part of Spain leading to an intense southwest flow over France and advecting warm and moist air over this region (Berthet et al., 2011). This feature prevails

preferably during summertime, and hailstorms occurring in spring or at the beginning of fall occur under different atmospheric conditions. In spring, hailstorms can be associated with the passage of fronts due to baroclinic disturbances.
Another hail hot spot is located downstream on the central part of the Pyrenean mountain range, which influences the general atmospheric circulations as well as the local-scale circulation that may have consequences on the spatial distribution of hail. The central part of Pyrenean mountain ranges possesses northwards valleys (orthogonal to the mean wind) that affect local wind regimes, which in turn are strengthened in sharp valleys and permit orographic lifting.

Rhone-Alpes is also a region frequently affected by hail. This region containing the large Rhone valley is boarded to the west by the Massif Central and by the Alps to the east. The southwest part, as well as the southeastern edge of the region, has a local hail maximum up to 31 hail days. The vicinity can explain these two hot spots to the Mediterranean Sea where during southerly flows warm and moist air is advected from the south towards the north through the Rhone valley. This warm and moist air can then be lifted, for example, near a front system crossing the country from northwest to southeast, and can lead to forced convection.

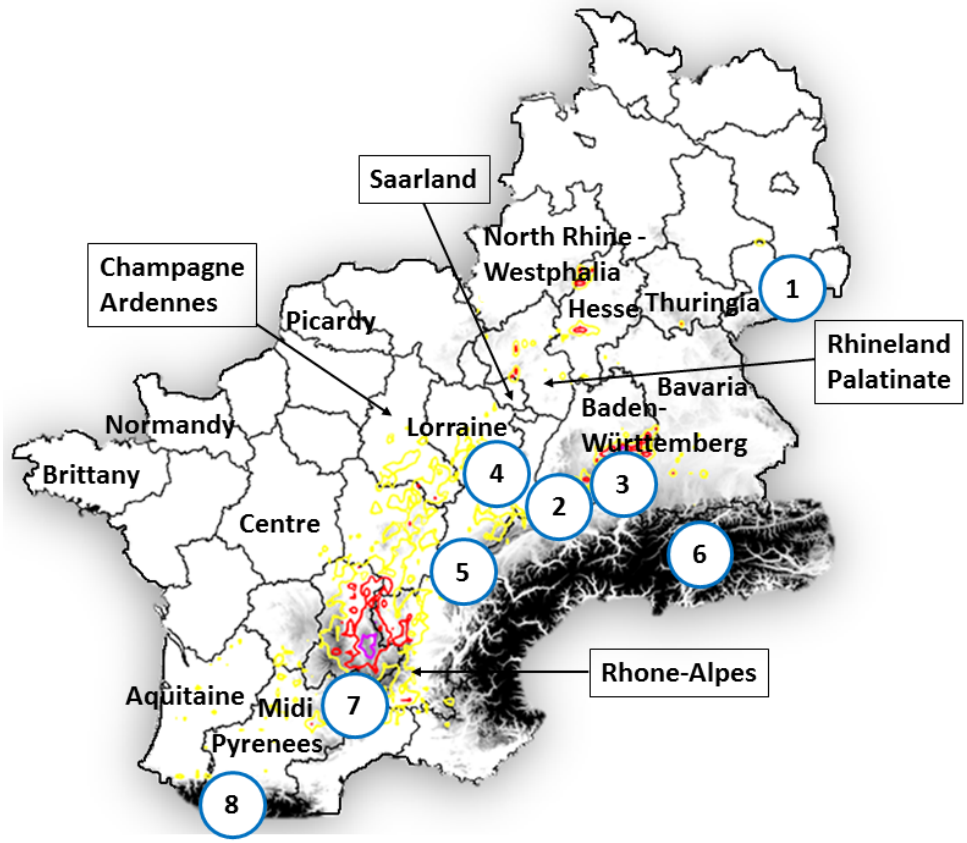

Fig. 4.1.: Regions mentioned in this study with mountain ranges. 1: Ore mountains, 2: Black Forest, 3: Swabian Jura, 4: Vosges, 5: Jura, 6: Alps, 7: Massif Central, 8: Pyrenees.

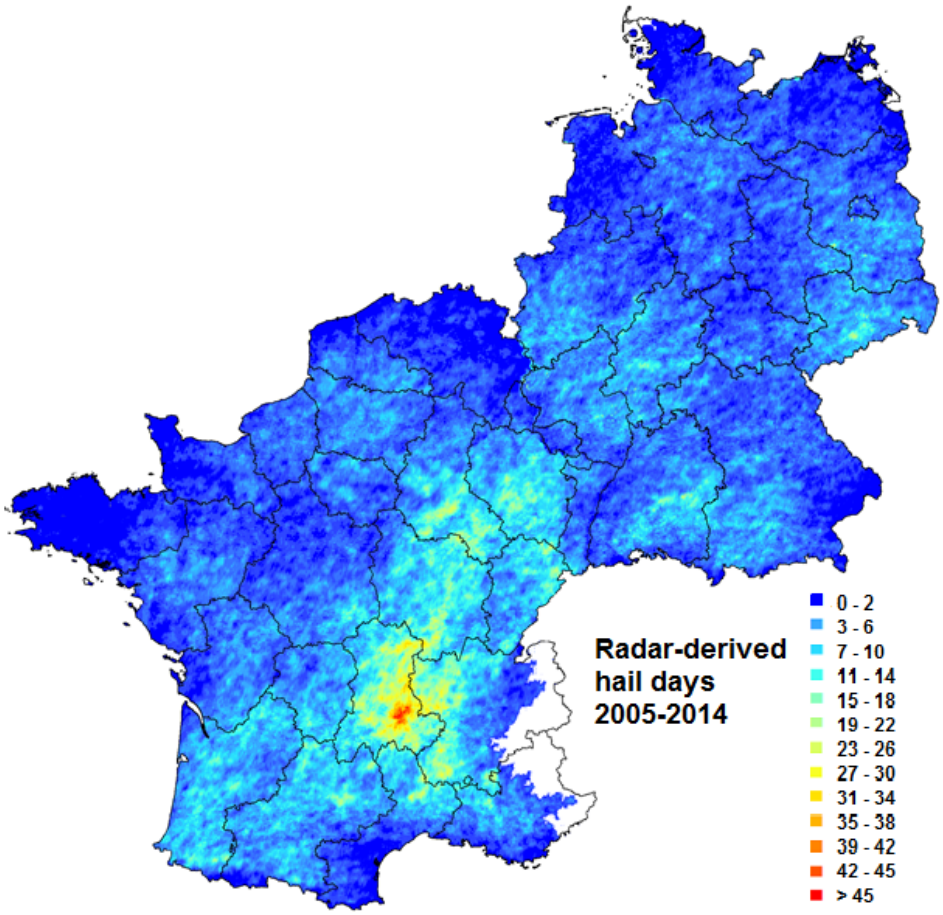

Fig. 4.2.: Number of radar-derived hail days for 1×1 km^2 grid points in France, Germany, Belgium, and Luxembourg (daily maximum reflectivities ≥ 55 dBZ) between 2005 and 2014.

The northeast part of France, specifically the regions Champagne-Ardennes and Lorraine, are affected with a maximum of 31 hail days in the southwest and 28 hail days in the south. The lowland Champagne-Ardennes region possesses mostly only hilly terrains in the southeast of the region. On average, 27 hail days can be counted during the period 2005 to 2014 in the central part of Lorraine. Continentality and flat land prevail also in this region where daily temperature lapse rate is increased. The Vosges mountain ranges are flanked to the southeast of the region and represent the solely high orography in this area. Strong southwest to northeast flows bringing warm, and moist air from Spain can affect the northeast part of France and interact with the local dry conditions. A local and weaker maximum of 24 hail days can be recognized at the southeast edge of Lorraine on the windward side of the south part of the Vosges mountains. The height of these low mountain ranges is slightly higher in the southern part of Lorraine compared to the north. The north-south orientation of the Vosges in addition to heights of low mountain ranges represent a natural obstacle opposed to the main southwesterly flow.

The main hail hotspot in Germany is located in the southwest part of the country in the state of Baden-Wrttemberg, more precisely near the Swabian Jura, south of the city Stuttgart with 31 hail days from

2005 to 2014. The low mountain ranges of Black Forest allows the flow to go around mountains at low levels causing a zone of horizontal flow convergence downstream, which is an area favorable for deep convection development (Kunz and Puskeiler, 2010; Koebele, 2014).

Weaker maxima with a mean of 11 hail days are situated north of the Alps in the Bavarian state. The north to south pre-Alpine-orientated valleys in this region may lead to flow deviations and low level convergence, similarly to the Swabian Jura area.

In the northeast part of Germany, a local maximum of up to 32 hail days is positioned over the Saxon Ore mountains south of the city of Dresden. This maximum is due to the pronounced thunderstorm activity in 2007. Also, Damian (2011) found a maximum by analyzing the lightning density from 2000 to 2009. The year of 2007 was characterized by frequent upper air troughs over Western Europe and ridges over Central Europe leading to high-pressure gradients on the eastern part of Germany and a southeast to northeast flux regime from the Czech Republic.

The northwest part of Germany, including the states of Hesse and Rhineland-Palatinate, and the southern part of North Rhine-Westphalia are regions affected by approximately 14 days with hail. Southwesterly warm and moist flows can reach these regions during hail days. Furthermore, the location of hail patterns is partly supported by the local orography that influences hailstorm development.

In contrast to hail hot spots located exclusively in the continental domain and along mountain foothills, most of the minima are found along coastlines where hail is also a year-round phenomenon ((Dessens, 1986)). Hail is rare along the Atlantic as well as Mediterranean coastlines, where the latter counts up to 2 hail days in its southern region. The large heat capacity of water may reduce the diurnal cycle of temperature leading to a decrease in lapse rate magnitude. As a result, the sea contributes to inhibition of severe convective storm development, even if the increased moisture content of the atmosphere near the coasts provides a source of energy for the storms. Furthermore, the seasonal temperature cycle over the seas is reduced compared to inland and leads to an increase in static stability. By contrast, cooling influences near the North Sea reduces the hail frequency over North Germany, which counts around 1 hail day, while the Atlantic Ocean reduces hail frequency over northwest France, where the surface temperature is lower than along the Mediterranean. Especially Brittany as well as the northern part of Normandy, areas close to the ocean have widespread minima with one or two days experiencing hail. A large minimum, located in the northern part of the central region, the region southwest of Parisian, and between Brittany and Paris may be due to a sparse radar coverage in these regions in combination with the attenuation of the radar signal from surroundings radar stations.

The Northern part of Belgium is also characterized by a low hail potential with approximately an average of one day with hail. A similar hail potential occurs in Luxembourg with 2 hail days. This low number of hail days can be explained by low pressures frequently crossing Belgium and Luxembourg with related front systems that favor convective cells.

Further hail minima are preferably found on mountain peaks, e.g., the Black Forest or the Pyrenees, with around 5 to 6 days with hail. This low potential can be due to unfavorable conditions for hailstorm for-

mation, such as a lower amount of moisture nearby the peaks and lower temperature at elevated heights. Very strong updrafts would be needed to raise an air parcel up to the mountain summit rather than along its slope. Rain, graupel or very small hail frequently prevails at the top of a mountain. Several authors previously found these hail minima over high mountains, including Kunz and Puskeiler (2010) over the Black Forest, Nisi et al. (2016) over the Alps, and Berthet et al. (2011) over the Pyrenean chain.
Thuringia and the north of Bavaria in Germany register significantly less radar-derived hail days. This area is covered by the radar station Neuhaus, which was out of operation for nearly the entire year of 2011. Another minimum that can be recognized in the hail-based statistics is situated over the Rhine valley with approximately 1 hail day. A special meteorological configuration in this valley situated between the Vosges mountains on its west side and the Black Forest on the east side permits the channeling of wind along the large valley and deviates the flow in a south-southwest to north-northeast direction. According to model simulations by Koebele (2014), low-level flow divergence predominates in convective situations leading to a decrease of convective activity.

4.1.2. Limitations

Several limitations must be considered in the hail-radar frequency maps. First, due to the local-scale nature of hailstorms and the lack of accurate observations, statistics are difficult to assess and validate. Indeed, no homogeneous observing system for hail exists over the entire region of Europe, but only local networks, for example, the hail pad network over the southwest, central, and southern France operated by ANELFA. As a result, validation between direct observations and hail proxies, such as hail days estimated from the Mason criterion, remains difficult. The use of radar and lightning data only allows obtaining hail proxies. Especially 2D radar data does not consider the vertical property of the troposphere in terms of the vertical extent of reflectivity cores or echotop height as provided by 3D radar data. Furthermore, using 2D radar reflectivity from the CAPPI, the maxima projected on the surface may be spatially and temporally shifted depending on the height, where the signal is derived, and, thus, the distance to the radar. Furthermore, effects such as bright band or beam shielding may lead to an over- or underestimation of radar reflectivity and, thus, the number of hail days obtained.
The radar coverage over Western Europe is reliable, but several regions are still not covered, such as the Alpine chain. This effect leads to a gap of data in the final composite. A limited radar coverage also exists in the southeast part of Germany and near Lake Constance leading to an underestimation of the hail potential in these regions. A low hail potential in the northern part of Belgium may prevail because only the radar stations of Zaventem and Wideumont cover this country. The far distance of North Belgium to the radar location can lead to an attenuation of radar signals and may yield an underestimation of the hail potential in this area. Northwest of France is less covered by radar stations resulting in, if data of a single station are missed in this region, no radar signal to be present from this area. Thus, the tracking of convective cells is more difficult, or even impossible, leading to a cut of an existing track or an impossibility to track the signals over space and time.

Both S-band and C-band radar data require accurate calibration when considered in the final radar composite. C-band radar are more sensitive than S-band radar, which has a longer frequency. Simultaneous use of S- and C-band radars can affect the hail proxy. Furthermore, the number of hail days can also be overestimated because of the advection correction. This leads to an increased spatial extent of the hail swath derived from META and, thus, the areas affected by hail. Moreover, the applied methodology computes maximum reflectivity only for 24 hours. When high reflectivity hits an area more than once a day, the day is only considered as one hail day and not as a multiple hail day. In reality, however, a single area of 1 km ^{2} is rather unlikely to be hit several times a day. Finally, the composite is a combination of radar data and lightning data meaning that the composite is dependent on the availability on lightning data.

This thesis presents for the first time a radar-based frequency assessment of hail for a large European area, including countries of France, Belgium, and Luxembourg based on the same methodology and investigation period. In the literature, only a few authors have estimated hail probability for the entire area of France, for example, based on insurance records or weather station reports (Ginouves, 1978). These studies rely on poor data quality and are, moreover, outdated. The hail hot spots downstream of the Massif Central in France, as well as the southwest part of France, were also recognized to be the sole synthetic hail hazard map available for France computed by Vinet (2002) based on insurance claims data and hail observations for 30 years (1962-1992) recorded with the hail pad network installed and maintained by ANELFA. A more detailed study by Punge et al. (2014) estimated the hail potential over Europe from satellite data during an 8-year period in Europe and found as well an important hail potential on the foothills of the Massif Central and the Pyrenean mountains. Hermida et al. (2015) recently used data from the ANELFA hail pad network and found that the Gers department, located on the west side of the Midi Pyrenees region, is the area most affected by hail in southwestern France.
Several hail maxima were also recognized in Germany, mostly near low mountain ranges, such as the southern parts of Bavaria in the pre-alpine domain or along the Swabian Jura where topography reaches up to 900 m. By analyzing the hail potential over Germany using 3D radar data, Puskeiler (2013) also found that an area located south of Stuttgart is the region most affected by hail with more than 30 radar-derived hail days from 2005 until 2011. The hail potential over Germany also suggests a substantial north-to-south gradient in the number of hail days. This trend was also found in several studies based on insurance or remote-sensing data (Schwind, 1957; Lindloff, 2003; Zimmerli, 2005; Puskeiler, 2013).
Northern Belgium was found by Lukach and Delobbe (2013) as a hail minimum. The top of the Black Forest was identified by Puskeiler (2013) also as a hail minimum.

Hailstorm tracks from 2005 to 2014 computed by the algorithm META are represented in Figures 4.3 and 4.4. A track is defined as the trajectory of a convective cell detected by the tracking algorithm and projected to the surface. It must be distinguished from a hail swath representing the entire extent of a

hailstorm. Results attest considerable spatial variability in terms of both track density and direction. The spatial distribution of tracks coincides well with the number of hail days with the highest number of tracks located over the Auvergne region in France and the states of Baden-Wrttemberg and Bavaria in Germany. In detail, the most significant concentration of tracks in Germany is situated along the southwestern range of the Swabian Jura with most of the tracks evolving in parallel to the ridge or crossing the mountain range mostly from the southwest to northeast. Similarly, the Alpine foreland in the southern part of Germany prevails a high number of tracks. Another region often affected by hail tracks that crossed in all directions is located to the north of the Ore mountains. The northern part of Germany is less affected by hail streaks and differs from the southern regions by showing a higher variability of track directions. Interestingly, longer tracks in north Germany often have a northwest to southeast direction presumably associated with the passage of cold fronts usually coming from the North Sea.

In France, a pronounced maximum in the track density is found again near the Massif Central (Figure 4.4). Most of the tracks come from the southwest accumulating on the Limagne plain. Another hot spot is located along the ridge of the Jura mountains with frequent south to southwesterly tracks. The Pyrenees are also often affected by hail trajectories mostly following a southwesterly flow or progressing laterally along the eastward orientation of the valleys as also described by Berthet et al. (2011). Brittany and Normandy are only affected by a few shorter tracks predominantly in a northwest to the southeast direction in coherence with cold fronts passing over these areas. In general, the northwestern part of France is less frequently crossed by tracks primarily due to the vicinity of the Atlantic that reduces convective activity.
Belgium and Luxembourg are also less frequently affected by tracks. Most of them have a southwestern direction in continuation with northern France. They occur more frequently in the southern part of Belgium than along the coastlines for the same reasons described above. The more continental location of Luxembourg leads to a higher track density compared to Belgium.

4.2. Seasonal cycle

Annual mean frequency anomalies were computed for the entire investigation area (Figure 4.5) as the subtraction of the average number of days with hail per year compared to the average number of hail days between 2005 and 2014. Positive or negative values represent higher or lower numbers, respectively, of hail days compared to the 10-year average. The annual variability is high with an absolute maximum reached in 2006 (+1.27 days with hail compared to the average). During that year, a large part of Europe, including Germany, Belgium, Luxembourg, and northwest France experienced higher temperatures, especially during the end of June and July when two heat waves occurred (Fouillet et al., 2008). As a result, sea surface temperature (SST) showed a positive anomaly leading to intense evaporation rates, and, consequently, may generate several low pressures. A high amount of moisture combined

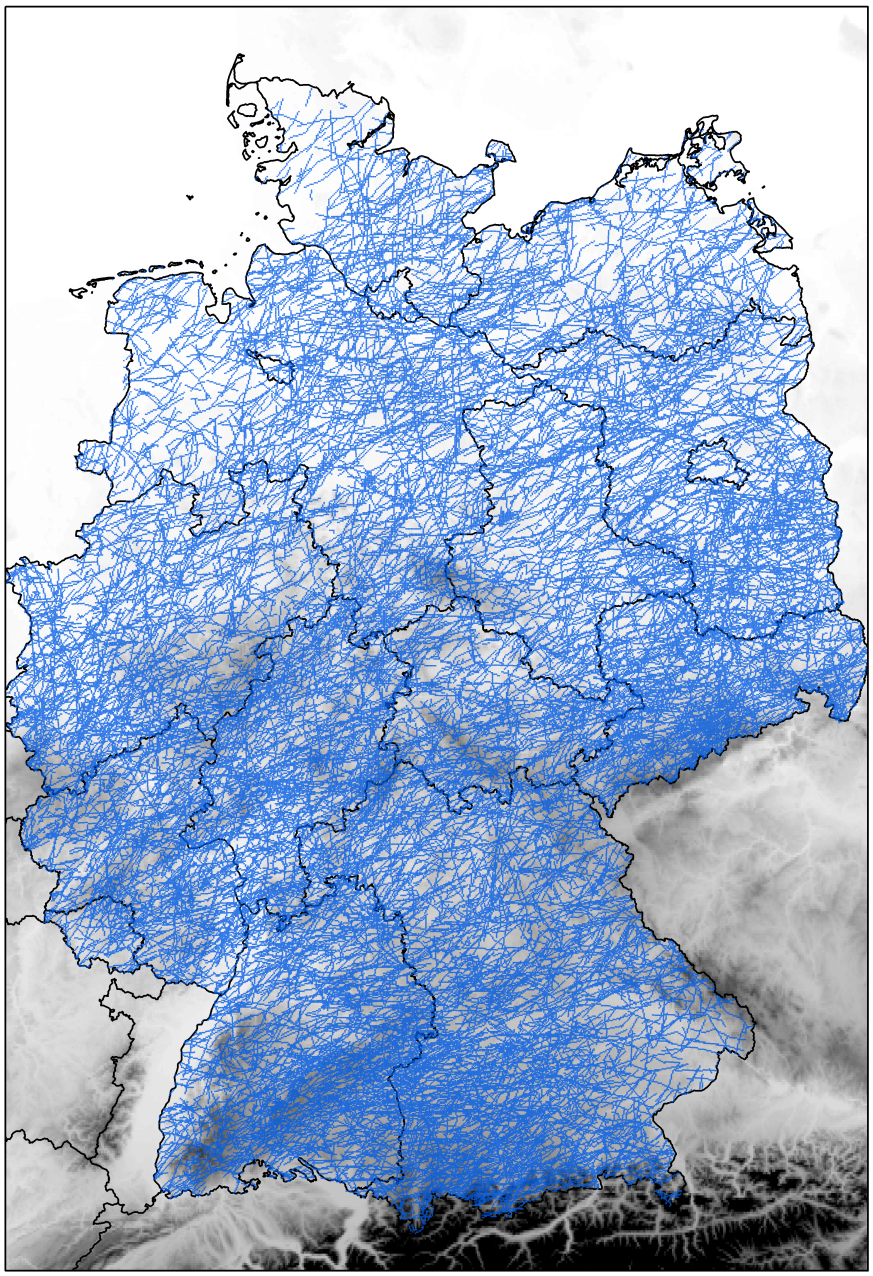

Fig. 4.3.: Tracks of hailstorms over Germany between 2005 and 2014 as detected by META over 55 dBZ.

with intense lifting by low-pressure systems may have fostered the formation of hail. For example, a very intense hailstorm severely damaged the city of Villingen-Schwenningen located in southwest Germany, south of Stuttgart, on 28 of June 2006. Note that intense lightning activity was also recorded during all of 2006 in Europe. 2007 was another year with a positive anomaly (+1.17) due to an increased convective activity over southern France and northeast of Germany. As discussed in the previous Section 4.1, the area near the Ore mountains was particularly affected by hailstorms during this year.

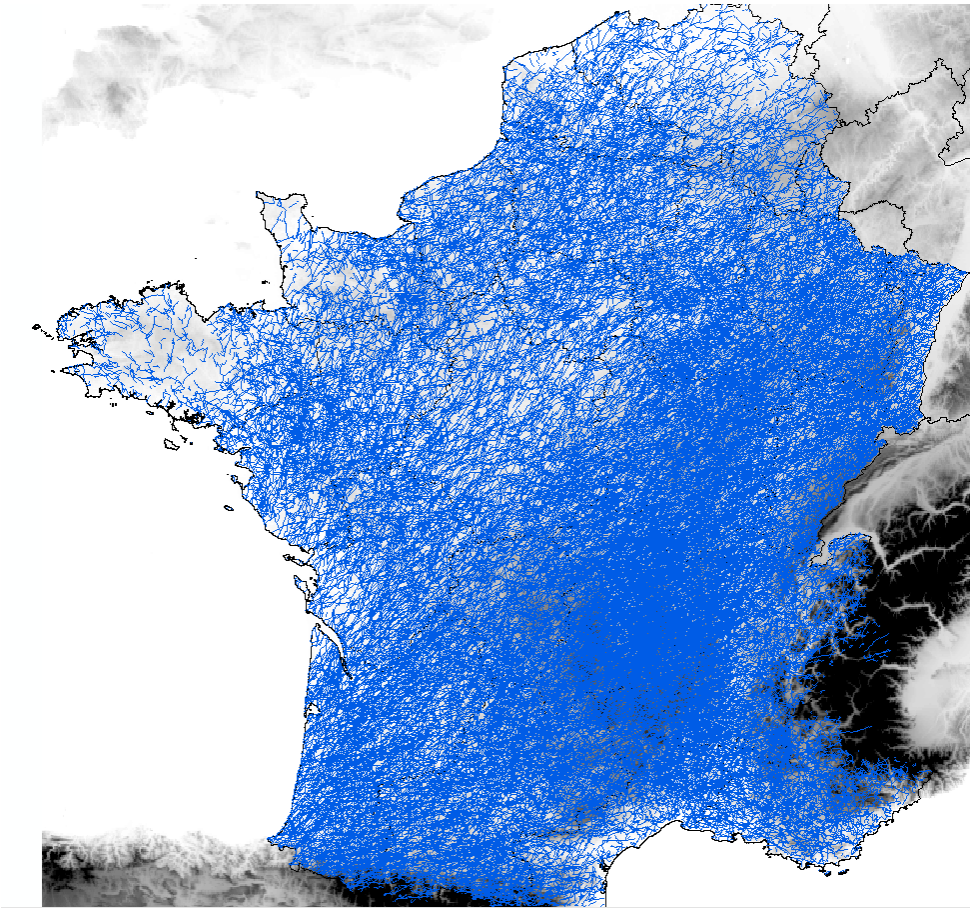

Fig. 4.4.: Similar to Figure 4.3 but for France, Belgium, and Luxembourg.

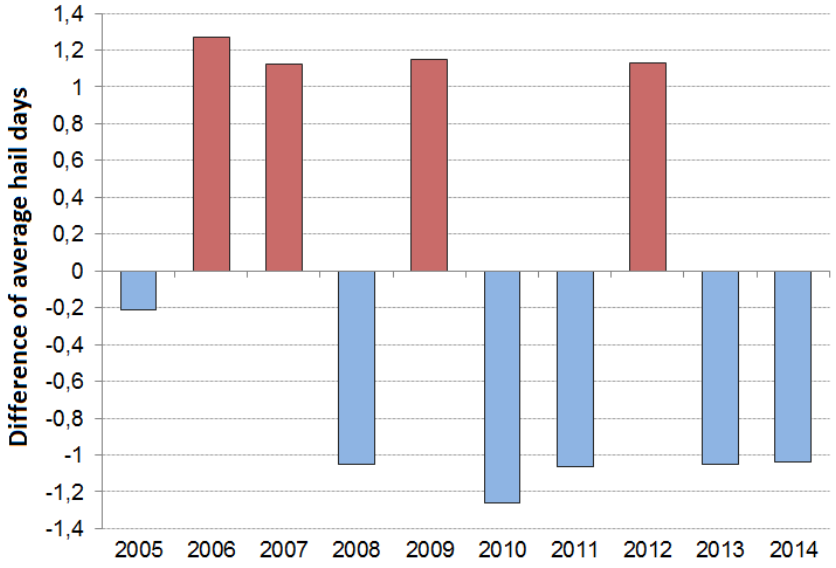

Fig. 4.5.: Anomalies of annual mean hail days with respect to the overall mean of hail days (from 2005 to 2014).

In 2012, the positive anomaly (+1.17) was due to an intense thunderstorm activity over Europe during this year. An important negative anomaly was observed in 2010 (-1.25 hail days). Although the summer

of 2010 was very warm worldwide over lands and oceans (NOAA, 2010), a persisting ridge over Europe suppressed the formation of hailstorms. A slight negative anomaly also occurred in 2005, but this remains unclear since some radar data were missed in Germany for April.

A negative anomaly reaches -1.1 during 2008 when Europe experienced a rather mild and cold summer, especially in July and August, leading to weak hail activity. No long-lasting anticyclonic period prevailed during this summer. A flow coming from the southwest sector was the most frequent situation often accompanied by rainy weather or local thunderstorms. The summer of 2011 was particularly rainy accompanied by unusual and fresh temperatures in July that may explain the less number of hail days compared to the average. Only on 11 September, at the end of an unusually warm period, several supercells producing large hail reached central and northern Germany.

The year 2013 shows a negative anomaly as well. June 2013 was colder than the average with the consequence that no hailstorms were formed, at least not in Germany. However, severe hailstorms occurred in Germany during July and August, especially on 27 and 28 July and on 6 August, with insured losses estimated above 3.3 Bn Euro for these events. A final negative anomaly is seen in 2014 (-1.03) when a single severe hailstorm crossed western France into Germany, such as the hailstorm named Ela, which hit the city of Paris.

As discussed above, 2006 and 2010 show the largest discrepancies in the number of radar-derived hail days with the largest positive and negative anomaly, respectively. Therefore, the following examines the spatial distribution of the number of hail days in 2006 and 2010. The overall hail patterns in 2006 strongly resemble the climatology with maxima near hilly terrains and minima near coastlines and over the northwest part of France. For both 2006 and 2010, the main hail day maximum is, as seen in the map shown in Figure 4.2, situated along hilly terrain, for example, in the Auvergne region. In 2006, this

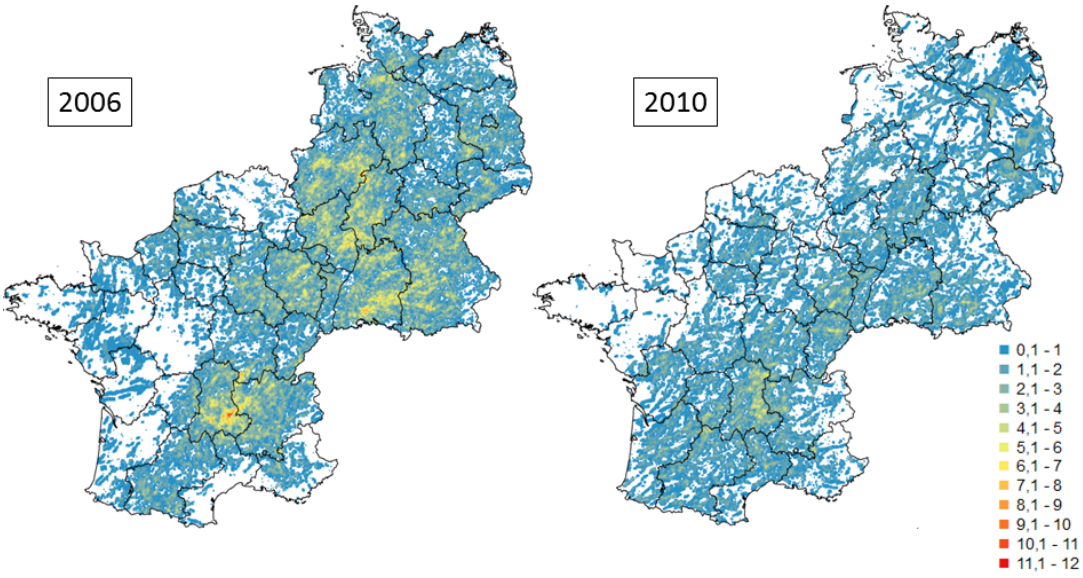

Fig. 4.6.: Same as Figure 4.2 but for the single years of 2006 and 2010.

region was affected by more than 11 hail days over and east of the Massif Central, whereas in 2010 only 6 days with hails occurred in the same region. In 2006, the northeast part of France was also affected by more hail days compared to 2010 over the entire Lorraine regions with an average of 3 days. In 2010, the south part of Lorraine, as well as the region east of the Jura mountains, was particularly affected by 5 hail days. Furthermore, a broad maximum appears along the Swabian Jura in 2006 (approximately 7 hail days) with a local maximum reaching 8 days at the southern part of the state Baden-Wrttemberg, whereas no such pattern was found in the same area in 2010. The west part of Germany, including the states of Hesse, Rhineland-Palatinate, North Rhine-Westphalia and Saarland was frequently affected by hail with some maxima reaching more than 6 hail days. A local maximum of 6 days is recognized at the eastern edge of the state Saxony-Anhalt in Germany during 2006. This structure is not present during 2010 when the area is only affected by 1 day with hail. The upper part of Lower Saxony in Germany is also affected by hail on approximately 6 days during 2006, whereas this region remains mostly without hail in 2010. For both years of 2006 and 2010, the regions, where the hail is less present compared to the mean, are located over the entirety of Belgium, Luxembourg, the northwest of France with especially Normandy and Brittany, which were not attained by hail, and along the coastlines. The Mediterranean coastline in 2010 was slightly more affected by hail than in 2006 possibly because small hail resulted from convective clouds surrounding the Mediterranean. The weather pattern configurations during summer 2006 with several upper-level troughs, and steep lapse rates at mid-level resulted in a strong unstable environment supportive for the development of organized thunderstorms over the entire domain.

The high convective season usually extends from April to September over most of Western Europe (Dessens, 1986; Mohr and Kunz, 2013). This agrees with the monthly distribution of radar-derived hail days (not shown). The overall distribution resembles a Gaussian with a maximum in July of 34 hail days and a minimum in April with 14 days. Hail is rare in April, due to a lower magnitude of the lapse rate compared to the summer. The number of days with hail increases moderately in May to 25 days and reaches 33 days in June. The number of hail days is again reduced in August with 26 days due to more stable environmental conditions on average. September has on average 24 days with hail. Hailstorms occur mostly in the southeastern part of France in late summer under Mediterranean influences when the SST and, thus, evaporation reach their maximum.

4.3. Influence of orography on hail events

As hail hotspots are frequently situated near mountains (see Section 4.1.1), orography seems to influence the frequency and distribution of hailstorms. The relation between elevation and the spatial distribution of hail hot spots is highlighted here to have a better comprehension of their variability near high, middle-range, and low mountains.

Figure 4.7 shows the number of hail days in 200 m height classes in Germany during 2005-2014 and for

France-Belgium-Luxembourg during 2002-2014. To enable direct comparison of the results, data were normalized by the maximum of the distribution yielding values between 0 and 1. The average distribution of the terrain is also shown for comparison. In France, Belgium, and Luxembourg the maximum is reached between 801 and 1000 m whereas the peak in Germany appears lower in the range of 601 to 800 m simply because of its lower orographic height. Above 2600 m, no hail days are recorded in Germany and only a few hail days are found in France due to the presence of higher mountains (the Pyrenees, Alps).

A spatial representation of hail hotspots, shows that they are mainly located on the eastern side of the mountains in the downstream direction considering the dominant flow from the southwest during hail events (Figure 4.8). In the following, the link between flow effects and the Massif Central is discussed. The region most affected by hail is located on foothills and downstream of the Massif Central. Several hail-prone regions are as well located downstream of low mountain ranges, such as near the Swabian Jura or the Ore mountains. The physical dimensions of a mountain in terms of height, width, solar exposition, and orientation substantially modifies the flow characteristics (Section 2.1.4).

A north to south gradient is located in the area of Massif Central (Figure 4.8). 36 days with hail were detected on the raster surface on the leeward side of this mountain. A larger area of 32 hail days extends around the local maximum described above, boarding the eastern flank of the Chaine des Puys (Figure 4.9), the eastern part of the Forez mountains, and the north flank of the Aubrac mountains. The surface covered by this last maximum is enlarged until approximately 100 km to the north, in the flatlands of the Limagne plain. Additional areas affected by 26 hail days can be found from the upper elevations of the Aubrac mountains in the south to the north part of the Auvergne region. Further scattered areas with the same potential of 26 hail days are located at low altitudes in northeastern France, including Lorraine, Burgundy, and the east of Champagne-Ardennes proving an influence of the southwesterly wind in these

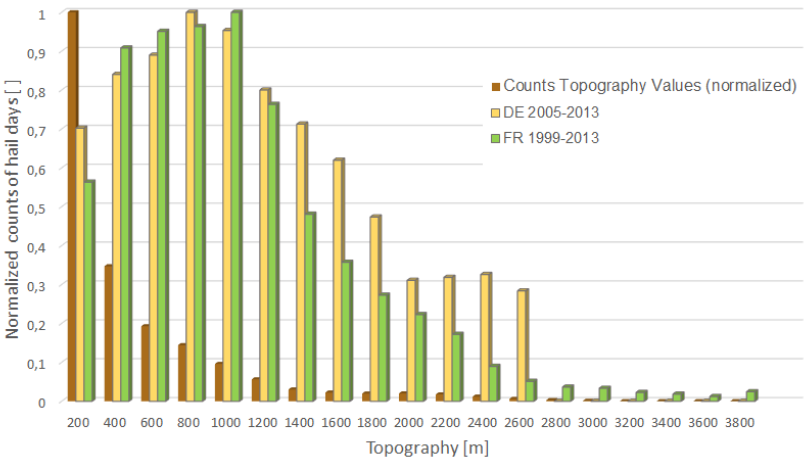

Fig. 4.7.: Histogram of height (brown bars) with radar-derived hail days. Yellow bars represent Germany, green bars France-Belgium-Luxembourg. The heights are normalized with their maximum.

continental regions. The high number of hailstorms downstream of the Massif Central suggests that the orography plays a role in the triggering of hailstorms in this region.

Three conditions are required for the initiation and development of deep moist convection: instability resulting from steep lapse rate Kottmeier et al. (2008), sufficient moisture content at low-level, and a triggering mechanism in terms of vertical lifting so that an air parcel can reach the LFC (cf. Section 2.1). It is necessary to mention the multiple scale interactions that favor the triggering of deep moist convection with processes from the synoptic scale to the local-scale (Barthlott et al., 2006). Planetary waves, such as Rossby waves that develop on the synoptic-scale (> 2000 km in length) favor low-level moisture flows and lifting mechanisms in response to geostrophic circulations balancing the wind fields by the production of vertical motion quasi-geostrophic balance (Eliassen, 1962). On the mesoscale (2-2000 km), flow convergence may trigger the development of convection via lifting (see Section 2.1).

A close-up investigation of hail hot spots shows the maximum is situated on the southwestern flank of the Livradois (Figure 4.9) situated between the Aubrac Mounts and the Livradois that extends from a northwest to southeast direction, which is perpendicular to the southerly wind flow. The hail potential is also high windward of Forez mounts with hot spots spreading out over the Limagne lowland situated behind the volcanoes of the Chaine des Puys. Most of the windward valleys located southwest of the

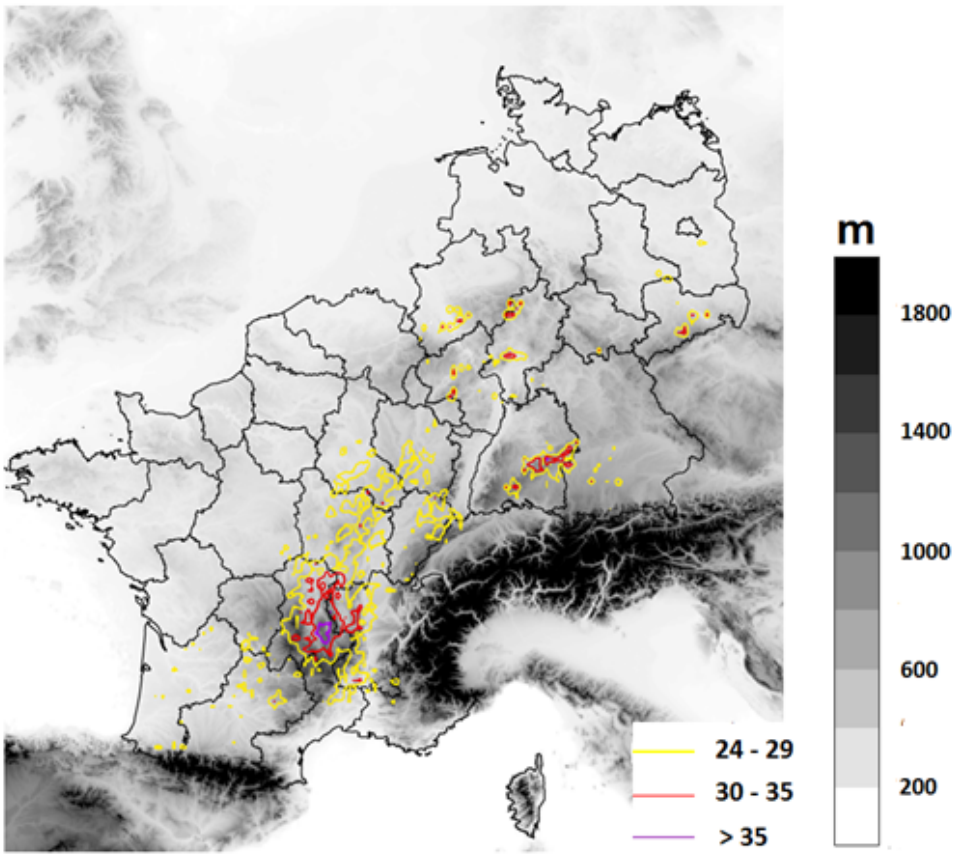

Fig. 4.8.: Contours of hail days overlaid with the orography.

Massif Central range are oriented from southwest to northeast permitting a continuous wind circulation and channeling from the southwest, and transporting warm and moist air from the Atlantic Ocean.

The maximum hail hot spot located on the flank of Livradois with 36 hail days is located geographically between middle-range mounts but extends over a few kilometers showing an interaction between several factors that result in the triggering of hailstorms in that specific region. At first, the V-shaped valleys on the western flank of the Massif Central encloses less air volume (Hennemuth, 1986) and store an important amount of sensible heat flux, enhancing upward motions.
Wind circulations in the valleys are driven by conversion of potential buoyant energy (from an unstable environment) to kinetic energy with updraft accelerations, for example, along upslopes of the Aubrac mountains. The release of potential buoyant energy necessitates dynamically forced triggering (Weisman, 1992). The heating of valley slopes can be combined with dynamic forces to enhance air to rise. Before the sunrise, surface airflow over the slopes is down-valley with stagnant conditions appearing in enclosed basins (Banta, 1990). Downslope flows typically become weaker during the night and cold air accumulates in valleys that disfavors the development of deep moist convection (Kaimal and Finnigan, 1994). After the sunrise, a dominant upslope wind develops in the isolated valley with a return circulation towards the valley center and is characterized by the advection of cold air (Langhans et al., 2013). This cold air advection counteracts heating over the slopes (Banta, 1990). The dry negative feedback mechanism limits the intensity of slope wind and represents a possible reason for non-stationary upslope flow on the Aubrac mounts, Chaine des Puys, and the southeastern slopes of the Massif Central (Figure 4.9). During the afternoon, flows may go over several mounts, especially along the Aubrac mountains and along slopes of volcanoes located on the western flanks of the mountain range. The Massif Central generates gravity waves inducing a gravity current on the leeward side of the mountain with associated

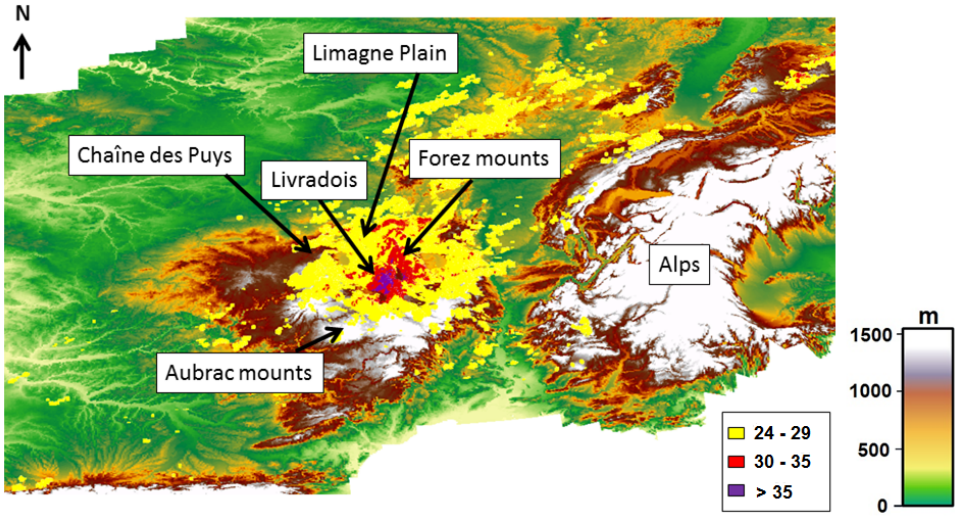

Fig. 4.9.: Visualization of the Massif Central subranges cited in the text overlaid with filled contours of hail frequency (yellow, red and purple).

sharped fronts (Chappell, 1986). The combination of high wind shear due to flow deviations from obstacles and low-level flow convergence as well as moisture mixing may lead to favorable conditions for convection triggering at low-levels on the leeward side of the mountain. After the sunset, surface cooling leads to the formation of downslope winds, for example, along with the Forez mounts, Livradois, and Aubrac mounts while upvalley winds still prevail aloft. Later, upvalley winds come to an end and are replaced by the downslope winds (Langhans et al., 2013).

The air above the ridge is influenced by strong synoptic flows, but also by daytime heating (Barthlott et al., 2006). As the slopes of the Massif Central are exposed to the sun and insolated, the mountain atmosphere can be destabilized, especially in the afternoon and early evening when convective activity is the highest. However, the effect of this large-scale lifting on convection triggering is less important than the dynamically-forced triggering at the local-scale, as discussed above. Channeling or gravity-driven winds can interrupt the diurnal cycle of winds in the valleys causing changes in wind speed and direction, and, thus, increasing wind shear during the daytime when the atmosphere is most unstable (Gross and Wippermann, 1987). At large-scale, the lifting mechanism may influence the development of deep convection (Sorbjan, 1996).

Hailstorms in Western Europe are associated mostly with southwesterly winds, but local-scale, thermally- or dynamically-driven wind circulations coming from different directions can interact with the dominant southwestern flow (Merino et al., 2013). For example, air flow coming from the Mediterranean Sea can transport warm and moist air along the Rhone valley until the Livradois by channeling and accelerating along valleys situated southeastern to the Massif-Central. These valleys are placed in a northwest to the southeast axis and permit a Mediterranean flow to circulate along the entire valley (Bastin et al., 2005). Furthermore, the Massif Central can be affected by a cold low-level wind (mistral) coming from northwest to south and transporting dry and cold continental air over the Limagne plain, thus blocking the foothills of the Livradois and Aubrac mountains where hailstorms occur frequently. Mistral takes place each time an anticyclone is centered over the Bay of Biscay, and low-pressure is located around the Gulf of Genoa (Millot and Wald, 1980). When this happens, a flow of air between the high and low-pressure areas appears, and a current of cold air blows from the north through the Mediterranean Sea. Note that the mistral blows especially during the spring and the change of season. (Millot and Wald, 1980). Thus, wind with different properties (the Mediterranean, from the southwest or mistral) can mix up at the foothills of the Livradois and create a very unstable environment. Warm and moist air masses may trigger convection leading to intense hailstorms in this enclosed area (Clements et al., 2003).

The literature concerning hail frequency over this area is rare, and nonexistent at this degree of detail. Punge and Kunz (2016) established a European hail-catalog based on overshooting-top detections and filtered with specific reanalysis data as well as hail reports, which affirms this region is frequently affected by hailstorms. The study of Dessens (1986) also confirms this. The geographical location of the Massif Central and its shape (in the continent, perpendicular to the southwestern flow) can explain the

high hail potential behind the Chaine des Puys. Moreover, the Massif Central is the first natural barrier from the Mediterranean Sea where orographic lifting can take place: warm and moist low-level air is forced to rise on mountain slopes. The deviation (in speed and direction) of the mean wind flow by the mountain can lead to a go-over regime casing gravity currents downstream.

Several large hail hot spots with high gradients are also found along the northern slopes of the Swabian Jura. A distinct, but very local, hotspot is located at the southwestern edge of the Swabian Jura partly extending on the upper flanks of the mountain. Two local maxima of 34 radar-derived hail days are situated on the north of the Swabian Jura as well as the upper eastern edge of the mountain range. The south part of these hotspots is located on the upper part of the mountain, whereas the northern parts are extending on the plain downstream. The Swabian mountain range extends from southwest to northeastern direction over several ten kilometers. Most of the days with hail occurred within a southwesterly flow, which is roughly parallel to the mountain range. This special configuration between the mountain range direction and wind flow may force hailstorms also to evolve parallel to the mountain range (Durran and Klemp, 1987). The southwest to the northeast direction of most of the tracks identified in this region confirms this hypothesis. Puskeiler (2013) also found a hail hotspot with more than 30 days with hail from 2005-2011 on the foothills of the Swabian Jura, which extends up to the top of the ridge. Kunz and Puskeiler (2010) found a Froude number below 1 in this region causing a flow around regime at low levels. Moreover, the authors hypothesize that the southwestern wind flows interact with the Swabian Jura at a very sharp angle that reduces the Froude number considerably and forces wind to flow parallel to the mountain chain.
A local maximum of radar-estimated hail days is also located in the north part of the state Hesse with 31 hail days, which is comparable to the hail potential of southwest Germany, as described above. The pronounced maximum in North Hesse lies directly to the east, and, thus, partly in the leeward of the Westerwald and the Sauerland. The orography nearby this maximum is slightly hilly. The tracks density beneath this region is also high but located further to the west suggesting that thunderstorm cells developed more in the west, and lead to hail only after a certain time and distance.
Another area with many radar-derived hail days can be found in a small area in the mid-west of the state Hesse with 30 hail days, downstream the Taunus mountains extending from southwest to the northeast, such as the Swabian Jura. As the spatial extent of the Taunus mountain remains small, orographic effects remain local behind the mountain.

4.4. Regional analysis of hail statistics

4.4.1. Seasonal cycle

Western Europe encompasses a large spatial variability of hail potential related to the distance to the sea, climatic characteristics, orographic effects, and weather patterns. As described in the previous section,

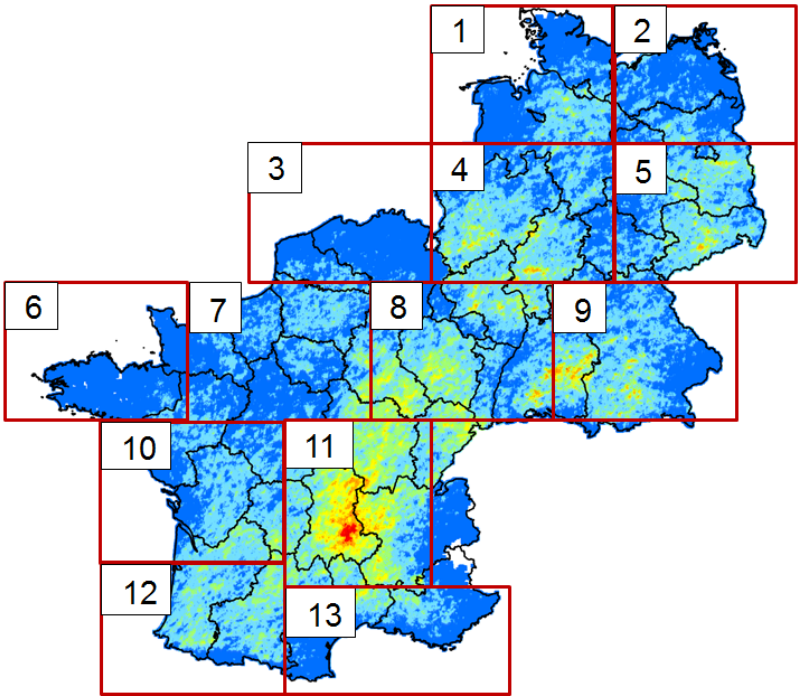

Fig. 4.10.: Definition of the 13 subdomains considered in the detailed analysis of hail days.

the hail potential is increased over hilly terrain far from the sea. Orographic characteristics (mountain ranges oriented near main wind flows, terrain gradients, and insolation of slopes), as well as circulations at low, mid, and upper levels, are determinant factors for the triggering of convection. Thermal latitudinal gradients and maritime influences contribute to enhancing the spatial variability. To better understand the characteristics of the events and mechanisms that favor the development of hailstorms, the total area under investigation was divided into 13 subdomains of approximately similar size (around 75,000 km ^{2}). Subdomains 4, 5, 7, 8, 9, and 11 are located mostly in the interior, whereas 1, 2, 3, 6, 10, 12, and 13 are influenced more by maritime air masses (Figure 4.10). Flatlands are found within domains 1, 2, 3, 6, 7, and 10 whereas higher mountains are located in regions 8, 11, and 12. Hilly terrain is situated in regions 4, 5, 9, and 13.

Figure 4.11 represents a 10-day moving average of the sum of hail days for each subdomain from April to September 2005 to 2014. The number of hail days results in the sum of grid points exceeding 55 dBZ inside each subdomain. Despite the variability in these graphs, some trends can be recognized. There is a delay in the seasonal cycle related to continentality (for example, regions 5, 8, and 11). The overall maximum is found in the mountainous region 11 comprising the Massif Central at the end of June with 531 hail days. Until the end of April, the number of hail days does not exceed 200. Specific weather patterns associated with a low diurnal cycle of the temperatures during spring may play a role in the reduced hail potential. During the spring season, reinforcement of low pressure systems forming over the North Atlantic may occur and wind flows may transport moisture and cold air into the inner continent. During May and the beginning of June, the number of hail days increases substantially from

281 for the 10-day average centered around 10 May up to 453 days on 9 June. The more important diurnal temperature cycle on continents, associated with a higher lapse rate, and lifting mechanisms engendered by mountains may explain this increase. During summertime, the peak is at the end of June, but the number of hail days remains high until mid-July with approximately 400 hail days during the 10-day moving average centered around 19 July. The passage of frontal systems over the domain during the summer, the higher lapse rate associated with southwesterly flows, advection of moist and warm air, and orographic effects may explain the peak. Between the end of summer and the end of fall, the number of hail days decreases again. Unfavorable environments, such as low near-surface temperatures, location of weather patterns that unfavored a transport from southwest to northeast, and absence of large-scale lifting are the main keys that inhibit convection.
Regions 7 and 8 also exhibit a high hail potential during the summertime with up to 282 days with hail for subdomain 8 at the beginning of July. The low moisture content in this area as well as different orographical characteristics, such as the Swabian Jura (oriented southwest to the east) compared to the arc-shaped Massif Central with high terrain gradients may explain the contrast between the hail-peak located in the Massif Central with approximately twice as many days with hail compared to the peak nearby the Swabian Jura. Within both domains, the number of hail days increases slightly until the peak with a local maximum in the middle of May (around 200 hail days). Air mass properties affecting the area may be different in May compared to July. Spring hailstorms may be associated with subtropical air masses coming from Spain, while some summer storms can form ahead of cold fronts. The number of hail days decrease sharply from the hail-peak season to the end of September. The temporal hail potential of subdomain 8 agrees with previous studies in Germany where the peak of large hail appears in June and July (Puskeiler et al., 2016). Gudd (2004) found a peak in the first decade of July in the study area of region 4 in West Germany that coincides with the results in this study.

Region 12 located in the very southwest has a hail peak in the middle of June with 214 hail days during the 10-day moving average centered around 19 June. Afterwards, the number of hail days first slightly decreases and then increases. This maximum found in June differs from the analysis by Dessens et al. (2015) who found that May is the most active month of the year followed by July over the southwestern part of France and the Mediterranean area (situated along the Rhone valley). Reasons for this discrepancy can be due to a longer period analyzed by Dessens et al. (2015) than in this study and by the use of hail pads in southwest France. Furthermore, the scattered network of hail pads used in the study of Dessens et al. (2015) is denser near the regions influenced by maritime effects instead of the inner continent.
The maximum number of days with hail in region 10 located in western France occurs during the beginning of June, reaching 168 hail days during the 10-day moving average centered around 9 June. The combination of coastlines and continental flatlands may influence the temporal occurrence. Furthermore, the absence of hilly terrains does not permit orographically-triggered convection. The Mediterranean Sea influences region 13 situated in southern France. Hailstorms appear principally in June when the heat capacity of the Sea increases from spring to summer. Higher lapse rates and weather pattern features

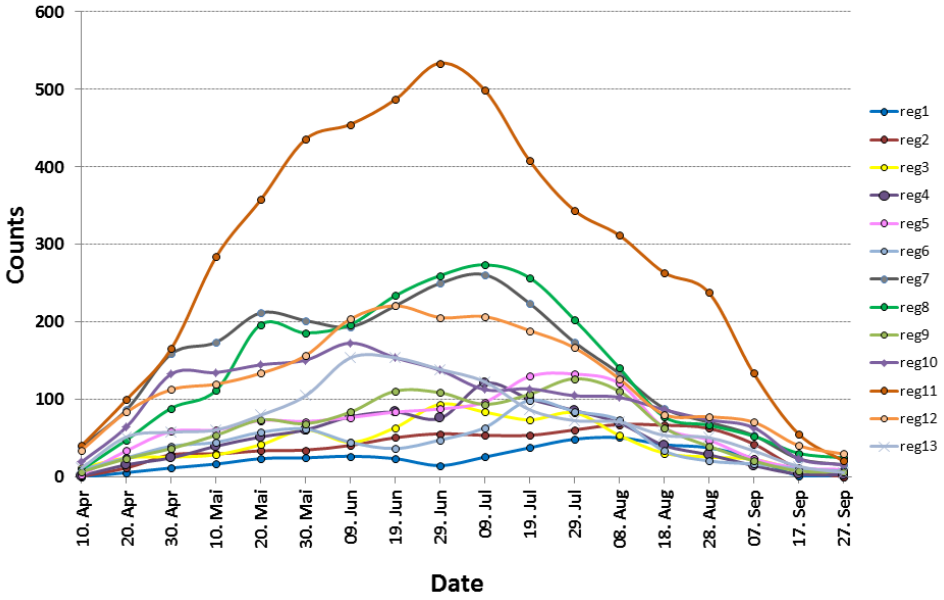

Fig. 4.11.: Time-series of radar-derived hail days (10 days moving average denoted as counts) for the subdomains shown in Fig. 4.11.

over the Mediterranean during June, such as the location of a low on the western side of the Sea, may explain this peak in June.

Region 3 covers the Picardy region in France as well as the upper western part of Belgium. The highest number of days with hail occurs during the end of June. Northern France and Belgium have a temperate maritime climate influenced by the North Sea and the Atlantic Ocean, with cool summers and sea-breeze conditions that may explain the peak of hail at the beginning of the summer. The sea-breeze is a circulation that develops due to differential heating of air over land and sea during the day. As the sun heats the surface, a resulting pressure gradient develops causing low-level flow from the sea to the land with a return flow aloft (return current). Sea-breeze generally occurs in spring or summer in Belgium when the temperature difference is the most important between land and sea compared to the fall. The same effects can occur in the region 6 which cover the region Brittany in France. The maximum is reached during the summer in mid-July. Exposed to the Atlantic summers are often marked with cold winds that transport moist and cold air masses over the flat region. A radar-based climatology from 2003 to 2012 conducted over Belgium by Lukach and Lukach and Delobbe (2013) proved that June is the most favorable season for hail.

Region 9 located in southeast Germany is where the highest number of hail days occurs at the end of July when the convective activity, due to local (local winds, uplifts) and larger-scale (for example, temperature advection) is the highest (increase of wind shear, low-level convergence). Note that the eastern edge of Germany is not accurately covered by radar stations, so that the number of hail days, as well as the temporal occurrence, may differ in reality.

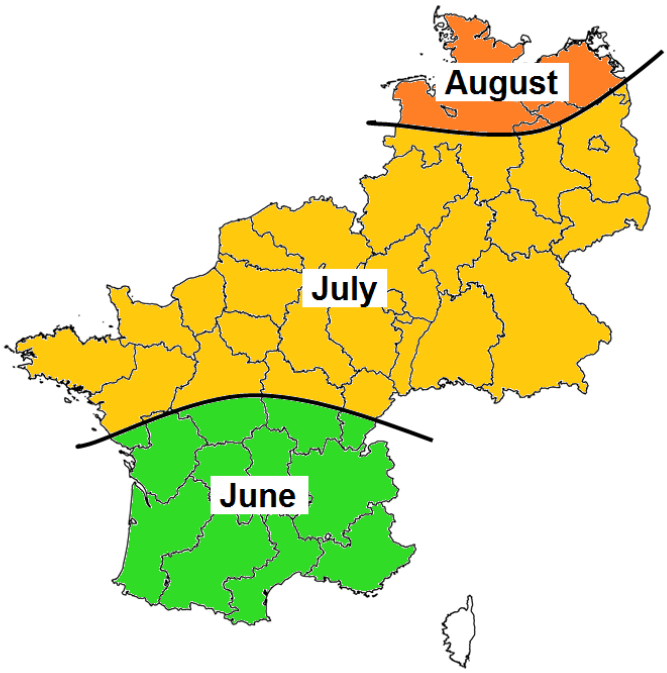

Fig. 4.12.: Month with the highest hail frequency occuring on average.

Regions 4 and 5 cover the western and eastern parts of Germany, respectively. Both regions have a mostly flat terrain with local hills. The maximum of hail days in regions 4 and 5 is approximately similar during the summer. This peak occurs during the beginning of July for region 4, whereas the peak appears at the end of July for region 5. This time delay may be due to the larger distance to the sea for region 5 than for region 4. Region 4 is more affected by maritime inflows than the inland. As the difference of temperature between sea and land is the highest during end June and July, the sea breeze is the most important process during the beginning of the summer, mainly affecting region 4.

Regions 1 and 2 have a similar hail cycle with maxima in August. The low number of hail days during the entire season may be due to the proximity of the Baltic Sea and the lower associated lapse rate unfavorable for deep moist convection. Furthermore, both regions are flat, so that orographic effects play only a marginal role over this area .

To summarize, a temporal shift of the maximum can be observed among all 13 subdomains. The spatial distribution for the month with the highest hail frequency for each region is resumed in Figure 4.12. The latitude differs over the entire investigated area causing a temporal shift of lapse-rates. Seasonal moving of weather patterns affects the number of days with hail.

4.4.2. Diurnal cycle

The diurnal cycle of convection is mainly determined by the near-surface temperature cycle and the resulting increase in the lapse rate due to solar insolation (Nesbitt and Zipser, 2003). Important trigger mechanisms, such as low-level flow convergence due to thermally-induced circulations over complex terrain, inhomogeneities in land use or sea-breeze circulations additionally influence both the daily temperature and convection cycle (Nesbitt and Zipser, 2003).
The hourly distribution of the number of hailstorms considering the onset of each cell-track per subdomain is shown in Figure 4.13. The onset is referred to where the cell tracking algorithm detects a potential hail core. Since the local time (LT) varies through Europe with approximately one hour from Brittany in France until Saxony in Germany, all given times are converted to LT representing four minutes per degree of longitude. Four minutes were then subtracted for each meridian situated westerly from the Greenwich meridian, whereas four minutes were added on the eastern side of the Greenwich meridian. All graphs show high variability. In general, hail is more frequent during the afternoon (13 to 18 LT) than during the night (midnight to 10 LT).

Hailstorms in subdomains 1, 2, 3, 6, and 13 located along the North Atlantic and Mediterranean coastlines as well as the North and Baltic Sea coastlines start principally at the beginning of the afternoon (13-15 LT). The earliest peak is reached at 13 LT in subdomain 6 over Brittany. Then, hail is more frequent at 14 LT in subdomain 1 located near the North Sea. Subdomain 2 situated along the Baltic Sea and subdomain 3 over Belgium have a peek at 15 LT. Over each subdomain located along coastlines, the number of hailstorms decreases sharply during the late afternoon. The absorption of solar radiation may explain this decrease by upper convective clouds leading to stability and weakened vertical motions.

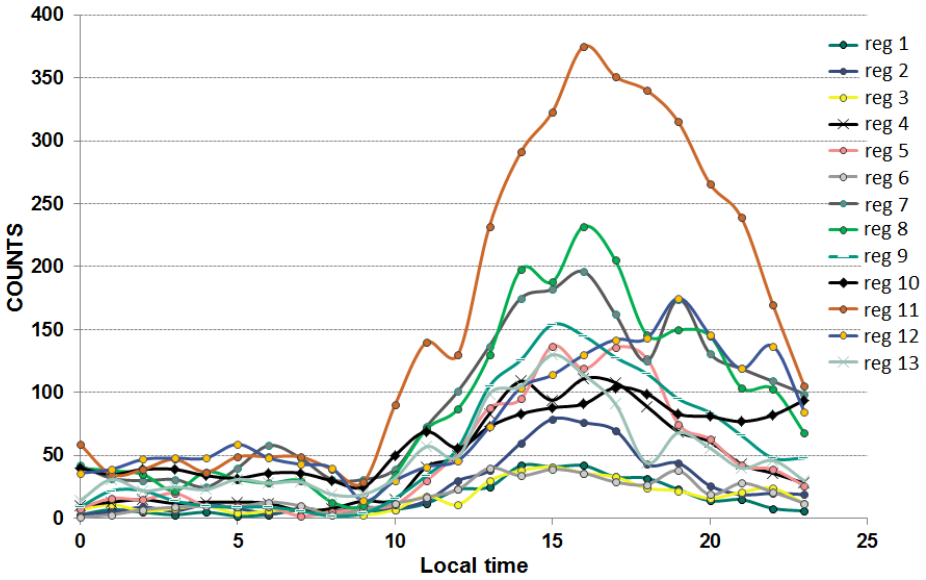

Fig. 4.13.: Hourly distribution of hailtracks for each subdomain.

The early start of hailstorms in these subdomains, as well as their lower diurnal cycle compared to other subdomains in the investigated area, can be plausibly explained by the lower temperature cycle due to the large heat capacity of the ocean. Subdomain 5 (East Germany) peaks at 15 LT, subdomain 9 (southeast Germany) reaches its maximum at 15 LT, subdomain 8 peaks at 16 LT, subdomain 11 over the Massif Central has the most important potential at 16 LT, and subdomain 7 has its maximum at 16 LT. The peak during the late afternoon for more continental subdomains is due to the surface heating resulting from daytime solar radiation as well as local effects, such as the orography (Nesbitt and Zipser, 2003).
The maxima in subdomains 10 and 13 located on the Atlantic facade appears later compared to other subdomains. Subdomain 10 has a peak at 17 LT and the subdomain 12, located between the Atlantic Ocean and the Pyrenees mountains, is at 19 LT.

Some literature exists about the diurnal cycle of hail in Western Europe. Kunz and Puskeiler (2010) also found a maximum of the hail events during the afternoon (13-18 LT) for the southwestern part of Germany based on a combination of radar data and insurance loss data. The study of Nisi et al. (2016) reveals a maximum of 13 to 18 LT depending on the investigated region with a peak 2 hours earlier on the pre-alpine domain compared to over the Alps range. An explanation for this time shift could be the initiation of the first convective cells by cold pools over the pre-Alps. Dessens (1986) also found a maximum during the late afternoon over southwestern France, which is under maritime influences.

4.4.3. Onset of hailtracks

To compare the spatial distribution of hailstorms during the night and day and to distinguish between convection triggered within the boundary layer and by large-scale lifting processes from upper tropospheric levels, the spatial distribution of track onsets is shown in Figure 4.14 at 02 and 18 LT (Figure 4.15). High spatial variability is observed for both hours. The occurrence probability during the night is much lower than during the day (227 onsets at 02 LT compared to more than 750 at 18 LT). During nighttime, onsets spread randomly along coastlines and the continent without any recognizable structure. Local effects such as the land to sea breeze during the night may affect the trigger of convective cells near the coastlines. The land sea-breeze effect may be reinforced over the Mediterranean as well as the Atlantic coastlines (Simpson, 1994).
In contrast, onsets at 18 LT form several systematic patterns near mountains, such as the Massif Central or the pre-Alpine domain in southern Germany or near the French Pyrenees. Local effects, such as low-level convergence and orographic effects, combined with large-scale features (fronts, large-scale lifting) may contribute to the reinforcement and development of convective cells near the mountain ranges.

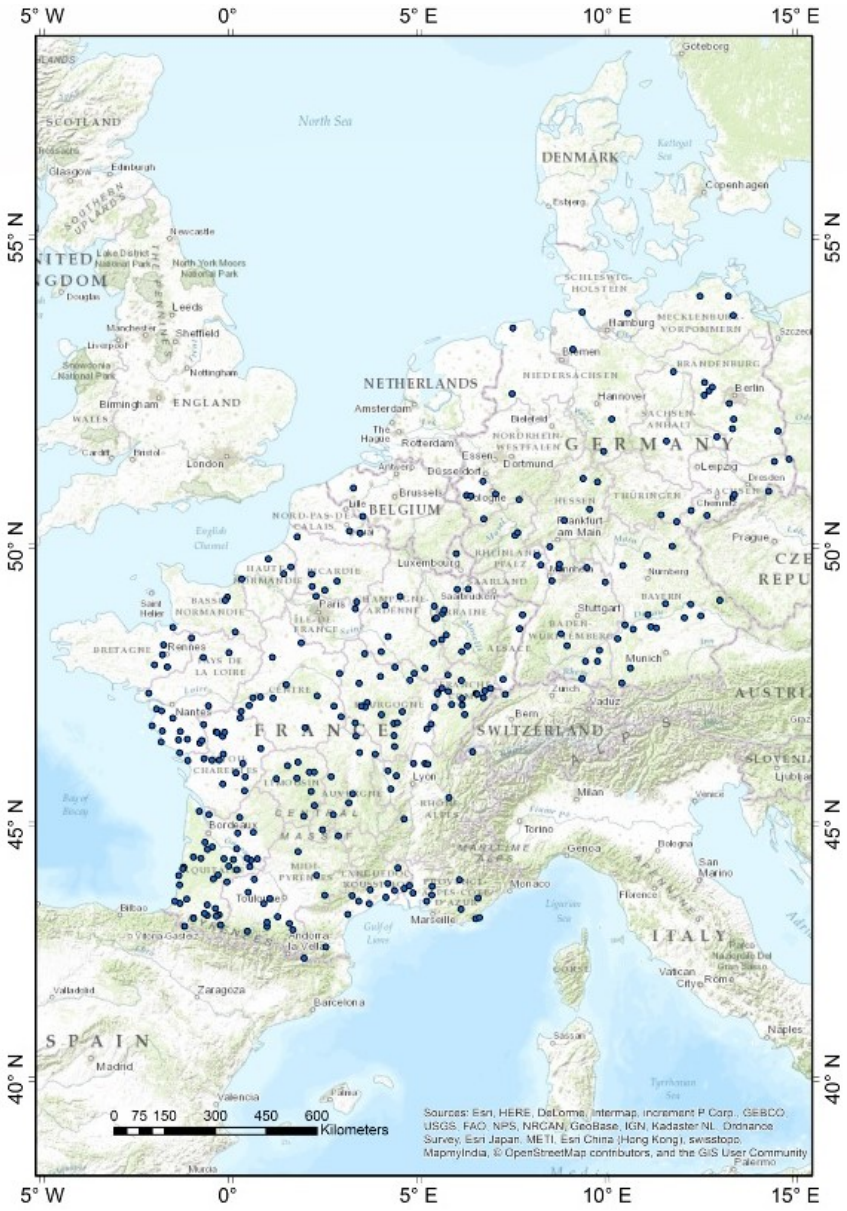

Fig. 4.14.: Location at 02 LT of the starting point of individual tracks detected by META.

4.4.4. Characteristics of hail swaths

In the following section, the main characteristics of all hail swaths occurring in France, Germany, Luxembourg, and Belgium are investigated. The computation and reconstruction of an entire swath are explained in Section 3.2. Length, width, orientation, and duration of all 20,163 individual hail swaths detected by the algorithm META are considered in this analysis.

A hail streak's length is defined as the distance in kilometers between the start and the end of a track determined by the tracking algorithm META, i.e., the period where the threshold of 55 dBZ is reached or exceeded. Figure 4.16 shows the occurrence probability of all detected hail swaths as a function of the

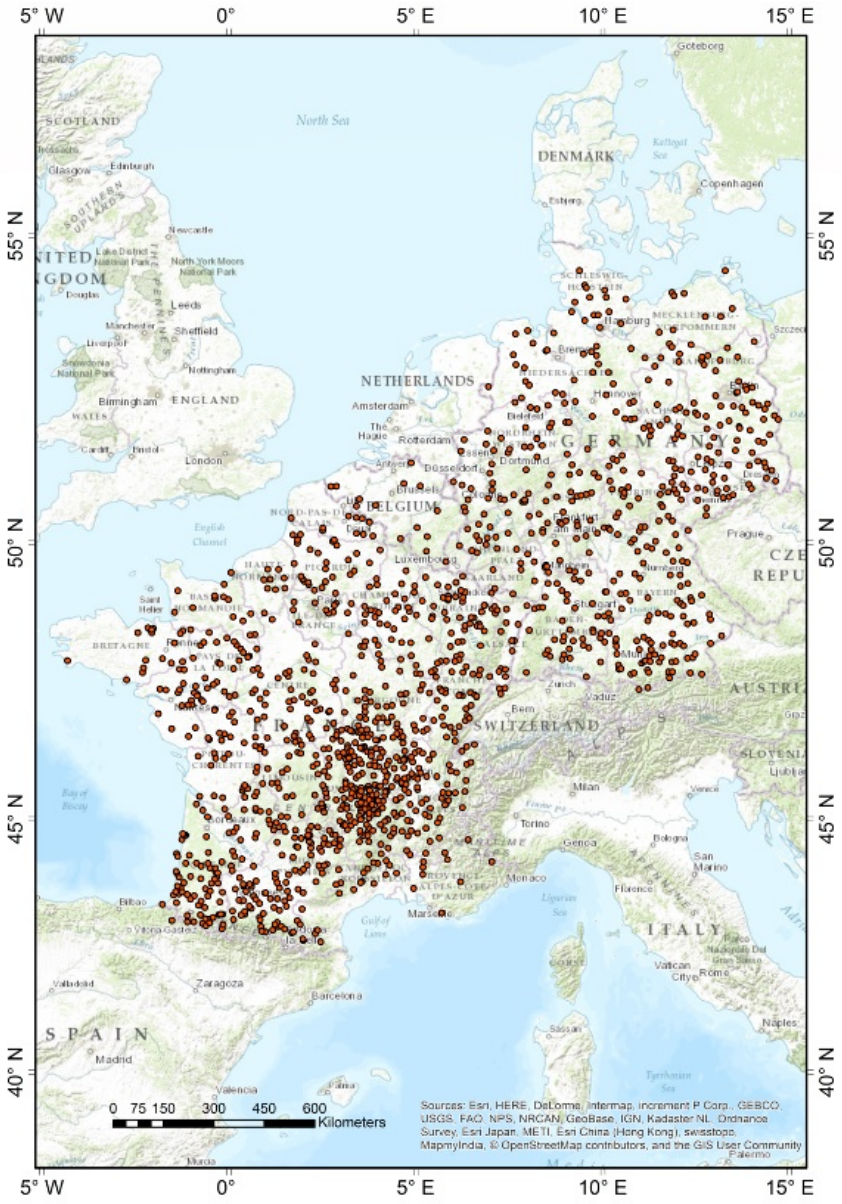

Fig. 4.15.: Same as Fig 4.16 but at 18 LT.

length in classes of 10 km. The tracks having a total length less than 1 km are neglected because these are considered not convective, and where heavy rainfalls are expected rather than hail. This distribution follows an approximately exponential function with a significant maximum for the first class. In total, 43% of all recorded storms over Western Europe possess a length between 1 and 10 km. Trajectories having a length between 10.1 and 20 km decrease sharply to 19% of the overall sample of trajectories. After that, the occurrence of storms possessing longer lengths decreases slightly. Approximately 30% of all streaks occur with lengths between 20.1 and 150 km. Less than 8% of storms have a length greater than 150 km. The longest swaths can be expected for highly-organized convective systems, such as MSC, including squall lines and supercells where large-scale features substantially dominate over local-scale

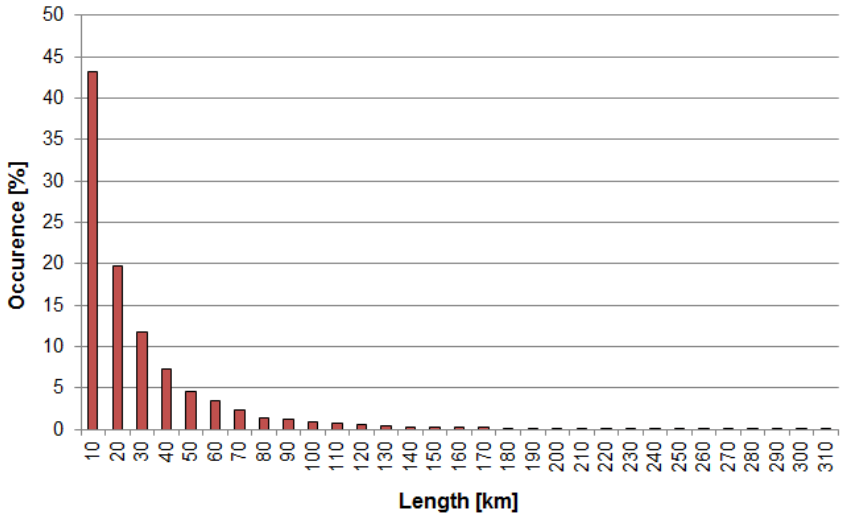

Fig. 4.16.: Histogram of the length of all hail streaks between 2005 and 2014.

effects, such a flow convergence downstream of mountains.

Hailswath widths separated in kilometer classes are shown in Figure 4.17. The width is expressed as the maximum diameter of the largest reflectivity core ($\geq$ 55 dBZ) during a hailstorm or the longest distance between two cores evolving laterally, in the cases of cell-merging or splitting. As only the largest width of each swath is recorded, the results may be overestimated. A Gaussian distribution overlaps the result with a peak at 9 km (21% of occurrence) and minimums at both 4 km (0.8% of occurrence) and 15 km (0.6% of occurrence).

Figure 4.18 shows the mean angles of hail swaths with 20° classes. The mean angle represents the mean orientation of a storm trajectory, and is the angle recorded by META at the center of a swath, as most of storm trajectories are linear. The orientation is defined as the angle between the line intersecting

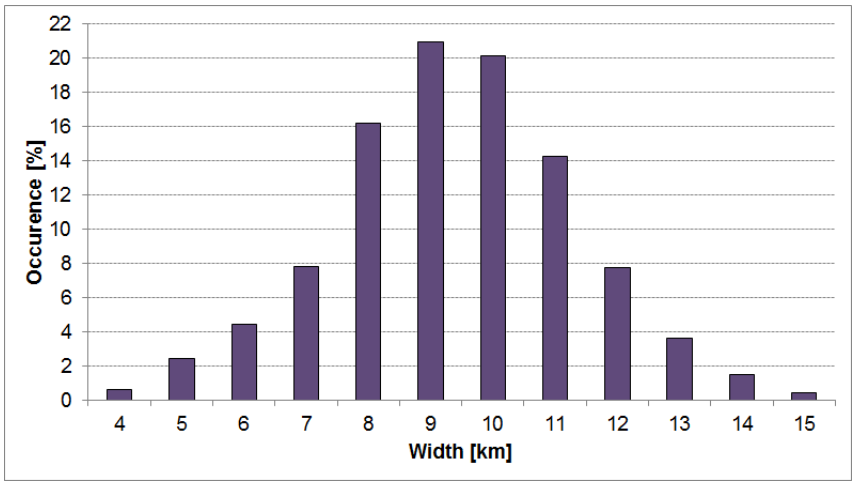

Fig. 4.17.: Same as Fig. 4.16 but for the width.

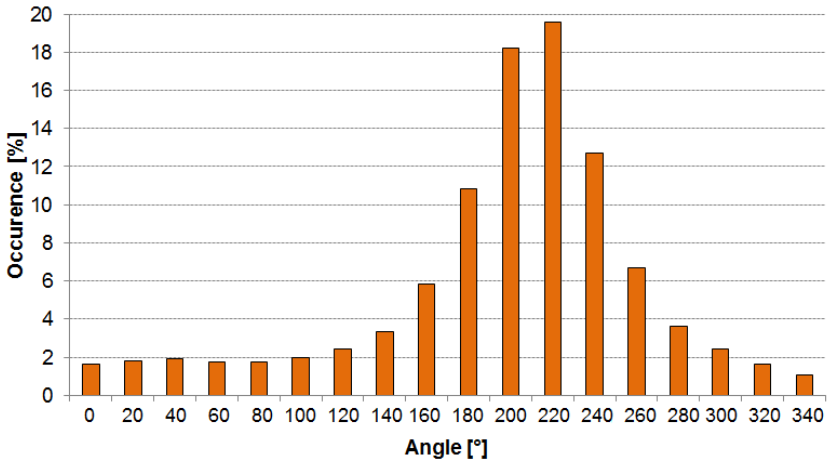

Fig. 4.18.: Same as in Fig. 4.16 but for the mean orientation.

core centers, before and after the central point of a swath, to the azimuth. With this method, three time steps must exist for a swath to be recorded with a duration of 15 minutes. For slight arc-shaped trajectories, central orientation may not be accurately represented. However, only a few tracks are curved so that this effect can be neglected. The maximum occurrence (19.3%) is found in the propagation direction between 220° and 240° attesting a southwest direction. Around half (51%) of the hailstorms crossing Western Europe come from a southwest direction between 200° and 260°. Only 2.8% of all swaths have a northwesterly direction. The principal southwesterly swath orientation found in the statistics confirmed previous results, such as the study of Puskeiler (2013) who found an important number of hail days (around 320 days) in southwest Germany where the swaths are oriented southwesterly. In the Aquitaine region in France, Berthet et al. (2013) found that severe hailfalls during 1952 and 1980 came from a southwest direction with a mean of 241°.

One of the outputs of the META algorithm is the number of time steps (a time step is equal to 5 minutes) of an entire hail streak (i.e., the time above the threshold of 55 dBZ). Thus, the total duration of a hail swath can be simply computed by multiplying 5 minutes by the number of steps minus one. As already mentioned above, a minimum of 3 time steps (so, a total duration of 10 minutes) is needed to be recorded by the algorithm. Figure 4.19 shows the occurrence rate of hail swaths in classes of 30 minutes. In accordance with the length, the duration also decreases exponentially with a peak situated at 30 minutes. As for the other physical characteristics, long-lived swaths are rare: only 2.4% of all cells persist over 5 hours, which correspond to organized cells.

4.4.5. Relationship between hail swath dimensions and storm intensity

To identify the characteristics of severe convective storms, the relation between the spatial extent represented by the severity index RCSI, length, duration, and orientation of the hail swath are assessed using boxplots representing the 25% and 75% quartiles as well as outliers. Figure 4.20 shows the distribution of RCSI as a function of a length separated into 50 km classes. As expected, the median of the RCSI

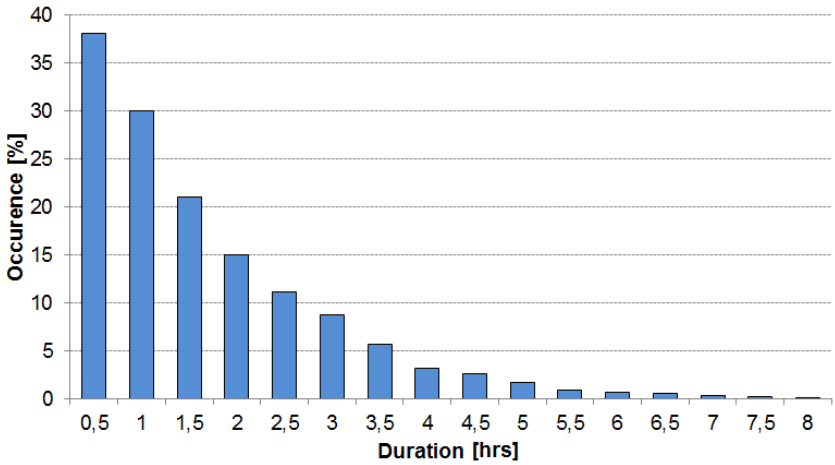

Fig. 4.19.: Same as for Fig. 4.16 but for the duration.

increases substantially with length from 252 for events shorter than 50 km to 2,263 for storms longer than 600 km. Also, the spread of the distribution tends to decrease with length. This effect, however, is due to the low number of long events. Nevertheless, the most intense hailstorms (RCSI > 2200) have a length superior to 450 km.

Another important parameter to estimate the severity of hailstorms is the total duration related to the total spatial extent, as shown in Figure 4.21. As for the length, values of RCSI increase with longer duration: the median is equal to 221 for storms shorter than 1 hour and increases up to 1,040 for storms

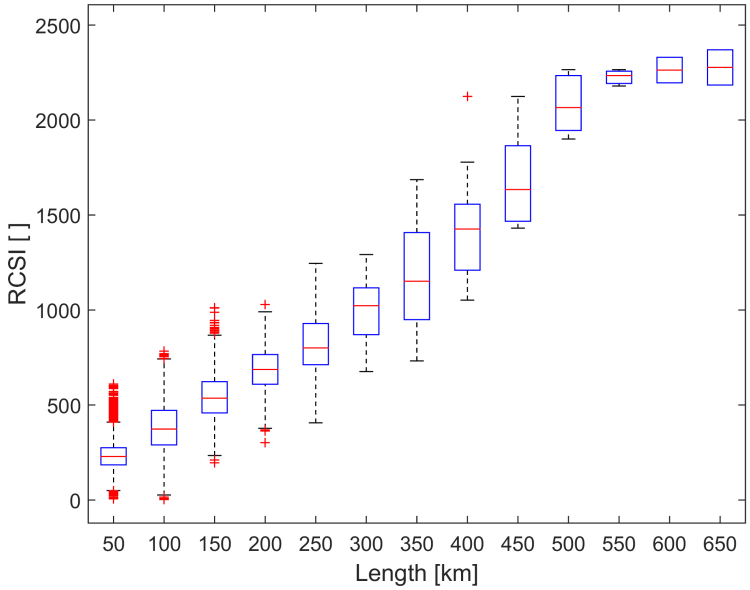

Fig. 4.20.: Boxplots of the RCSI as a function of swath length for all events between 2005 and 2014. The boxplots indicate the interquartile range (blue box), median (red bar), x% of the distribution (dashed vertical lines), and outliers (red cross).

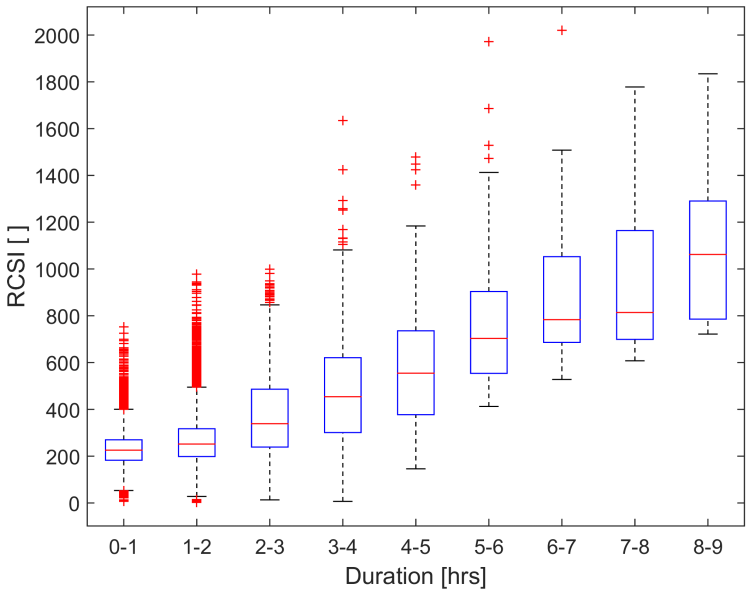

Fig. 4.21.: Same as Fig. 4.20 but as a function of duration.

persisting longer than 8 hours. The variability remains high with widespread distributions over time, possibly due to local high/weak reflectivity values along a swath that can affect the values of RCSI.

Figure 4.22 shows the monthly distribution of the swath lengths. In general, the longest tracks occur in July followed by June when the hail potential is also the highest for subdomains located in the southern part of the investigated area. In the same way, the shortest tracks appear in April and September at the beginning and end of the convective season, respectively, with maximum lengths of 180 km in April and 315 km in September. In May, only single tracks are greater than 400 km corresponding to severe hailstorms. In August, the maximum length is equal to 483 km. For each month, the interquartile range remains weak due to the exponential decrease in the number of storms with length.

The last parameter considered is the mean orientation of hail swaths for intervals of 30°, as shown in Figure 4.23. As for the monthly distribution, the range of the boxplots for shorter events is limited. The maximum of the sample is located between 210° and 240° corresponding to southwesterly flow.

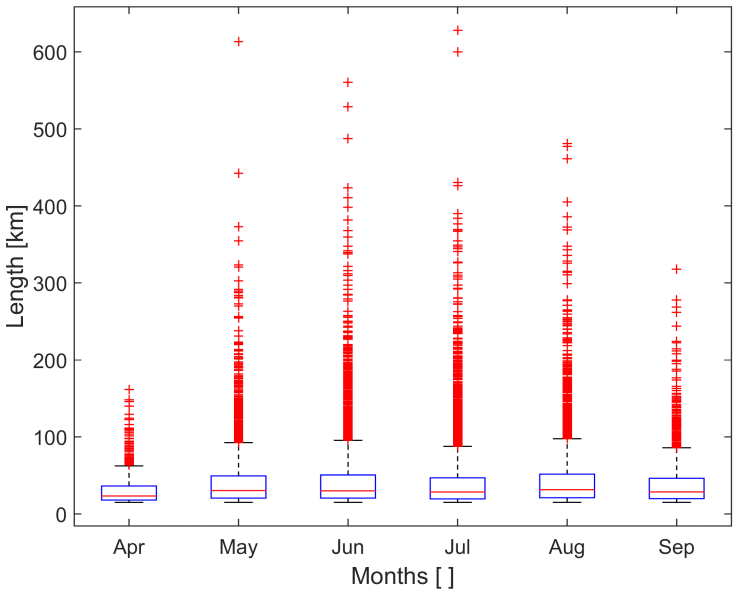

Fig. 4.22.: Same as in Fig. 4.20 but for length as a function of the months.

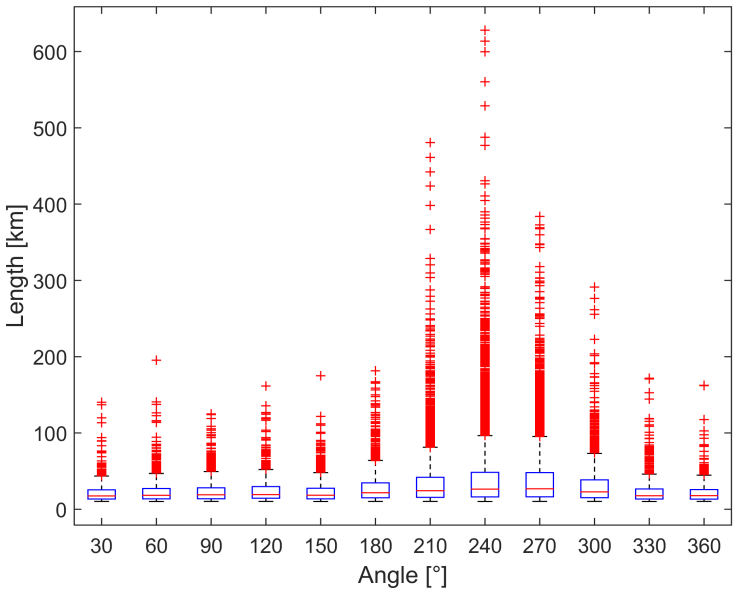

Fig. 4.23.: Same as for Figure 4.20 but for the length in a function of the orientation.

Minima are found for 330° and 30°, i.e., for flows coming from northwest and north-northeast directions.

To resume, intense storms can be identified, particularly during July, with a large spatial extent associated with long durations and lengths, respectively, coming from southwesterly directions. Favored atmospheric conditions that initiated convection at the surface are investigated in the next chapter.

5. Environments favoring hail

In this chapter, air mass properties in terms of stability and lifting surrounding hailstorms are investigated. The dataset used for this study is ERA-Interim reanalysis.
Principal Component Analysis (PCA) was conducted to improve the understandings of relations and interactions between selected meteorological variables (e.g., values of meteorological parameters at hailstorm onsets) and hailstorms severity. The second part of this chapter focuses on the atmospheric conditions prevailing around the first RCs of hail tracks identified by the tracking algorithm. The purpose of this section is to analyze the distribution of appropriate meteorological parameters and their magnitude near the events to gain a better comprehension of the large-scale mechanisms as prerequisites of hailstorm formation. Finally, synoptical conditions during hailstorms are analyzed for the geopotential height and wind speed anomalies with the objective to identify specific meteorological patterns prevailing during hailstorms and to quantify them near the storm for the large sample size of hail events obtained by this study.

5.1. Air mass properties over Europe at the onset of hailstorms

A PCA was first performed to assess the variable contributions to RCSI that quantifies the severity of a hail event. The results obtained by the PCA are used for further analysis in the next sections. In this PCA, hail swath characteristics were investigated along meteorological parameters. Input data for the PCA include mean values of selected meteorological parameters from ERA-Interim at hail swath onsets recorded by META. As META records coordinates of each hail swath's starting point, the nearest neighbor between the coordinate of the onset and the ERA-Interim coordinate grid was considered by selecting the smallest Euclidean distance between the two. Values of ERA-Interim assigned to the nearest neighbors for all hail events were recorded as a list, which provides the PCA input. As parameters from ERA-Interim are available every 6 hours, 12 UTC was chosen for each meteorological parameter representing pre-convective conditions of the day (e.g., Mohr and Kunz, 2013; Mohr et al., 2015b).
Six meteorological parameters were chosen in this study: vertical wind shear, CAPE, the difference between the equivalent potential temperature at 500 and 850 hPa (for stability/instability), the height of T0 (freezing level), specific humidity, and surface wind speed as all these parameters seem to have a link to convection according to the literature (Kunz, 2007b; Busch, 2013; Mohr et al., 2015a; Nisi et al., 2016; Punge and Kunz, 2016). Also, all these parameters show a relatively clear signal in the results, which was not the case for other tested parameters, such as vorticity advection. Temperature near the ground

was also neglected as no direct relation between hail, and this parameter could be found in the literature (Dessens, 1986). This is also the case for heat flux, where the effects are especially local or regional.

- Windshear as the wind speed difference between 6 km and the surface has an important influence on the organization of convective systems (Markowski and Richardson, 2010). Only in the case of substantial wind shear, organized storms, such as multicells, supercells or MCSs can form (See Section 2.2).

- Difference of θ_e between 500 and 850 hPa resulting in negative values characterize an unstable troposphere. In the mesoscale, θ_e is also a useful measure of the static stability of the unsaturated atmosphere (Bolton, 1980). Under stably stratified conditions, θ_e increases with height, and vertical motions are suppressed. The pressure level 850 hPa was chosen to compare those values with the study of Bolton (1980).

- CAPE represents the amount of convective potential energy available to accelerate an air parcel vertically, allowing the quantification of the upper thermodynamic limit of lifting. This study uses the median due to the skewed distribution function of CAPE.

- Height of freezing level T0: according to Dessens (1986), hail is favored by both high freezing levels in the ambient atmosphere and strong updrafts allowing ice particles to grow rapidly by accretion.

- Specific humidity at 950 hPa (q950): both thunderstorm and hail formation require a substantial low-level moisture supply (Longley and Thompson, 1965).

- Surface wind speed: strong winds approaching mountains could initiate convection in the vicinity of mountains by low-level convergence. Nevertheless, the role of surface wind speed on hail formation is not a direct effect.

PCA was performed in several steps. First, the values of each meteorological parameter among all hail events were recorded in a table. Then, the values in the table were centered (subtracted the mean from each attribute) and standardized to remove the influence of location and scale of the variables in the raw data. With these methods, columns in the table have a mean equal to 0 and a standard deviation equal to 1. Then, a covariance matrix was computed from the centered-standardized values in the table to understand the evolution between two variables (Jolliffe, 2002). A covariance matrix is always a symmetric matrix with the variances on its diagonal and the covariances off-diagonal (Wold et al., 1987). After this, eigenvectors with their corresponding eigenvalues were computed. An eigenvector is a vector that does not change its direction after a linear transformation (Jolliffe, 2002). Eigenvalues are simply coefficients attached to eigenvectors, which give axes magnitude. Another step is to sort eigenvectors by

decreasing eigenvalues, and therefore to choose eigenvectors with the highest eigenvalues. The ranking from highest to lowest values identifies the relevant eigenvectors for the study (Jolliffe, 2002). In this thesis, the first two components were chosen, which accounted for 62% of the total variance.
Interestingly, each variable is positive along the first component (C1), as shown in Figure 5.1, meaning that each variable contributes to the hail potential. Along the second component (C2), four variables (wind shear, T0, CAPE, and instability) are positive and two (surface wind speed and specific humidity) are negative indicating that these variables play a different role. Variables with negative values contribute less to pre-convective conditions favoring hailstorms compared to those with positive values. Among the positive values, wind shear ranks first with +0.62 along C1 and +0.51 along C2. A perfect fit between variable and components would yield a value of 1. Therefore, even if the wind shear reaches the highest values in this PCA, it only explains a fraction of the components. The second highest values are obtained for the instability reaching +0.61 along C2 and +0.415 along C1. So, wind shear and difference of θ_e between 500 and 850 hPa appear to be the most determining factors for the pre-convective conditions during days with hail.
Finally, PCA can be grouped into two clusters: surface variables, including surface wind speed and humidity, and those quantified from vertical profiles represented by the wind shear, CAPE, freezing level, and instability. Several studies, in particular those focusing on U.S. storms (Laing and Fritsch, 2000), found evidence that suggests a relationship between hail occurrence and convective available potential energy (CAPE) times vertical wind shear (Brooks et al., 2003; Craven and Brooks, 2004). In Europe, few authors agreed that these two latter parameters are relevant for hail occurrence (Púčik et al., 2015; Groenemeijer and van Delden, 2007; Kaltenböck et al., 2009;Eccel et al., 2012; Tuovinen et al., 2009). For example, in the Netherlands, Groenemeijer and van Delden (2007) determined a strong association of hail to high CAPE values and strong shear prior to events with large hail. Wind shear seems to not be a less relevant parameter for severe hailstorms in Europe compared to the U.S. (Graf et al., 2011; Mohr et al., 2015b).
A second PCA considering the 100 most severe hailstorms in terms of RCSI will be discussed in the next section.

5.2. Synoptic-scale anomalies during hail days

An investigation of upper tropospheric levels in addition to 2D quantities is important as hailstorms require specific atmospheric conditions to develop. Moreover, the upper atmospheric environment governs the meteorological conditions at all lower levels creating conditions that favor or suppress the development of hailstorms (Houze, 1993). Four parameters are considered for anomalies analysis: geopotential height, wind speed anomalies at 300 hPa, wind shear anomalies, and CAPE anomalies. Geopotential height and wind speed anomalies were computed for a large domain over Europe, while wind shear and CAPE were analyzed in the investigated area. Relative differences were computed for each parameter by

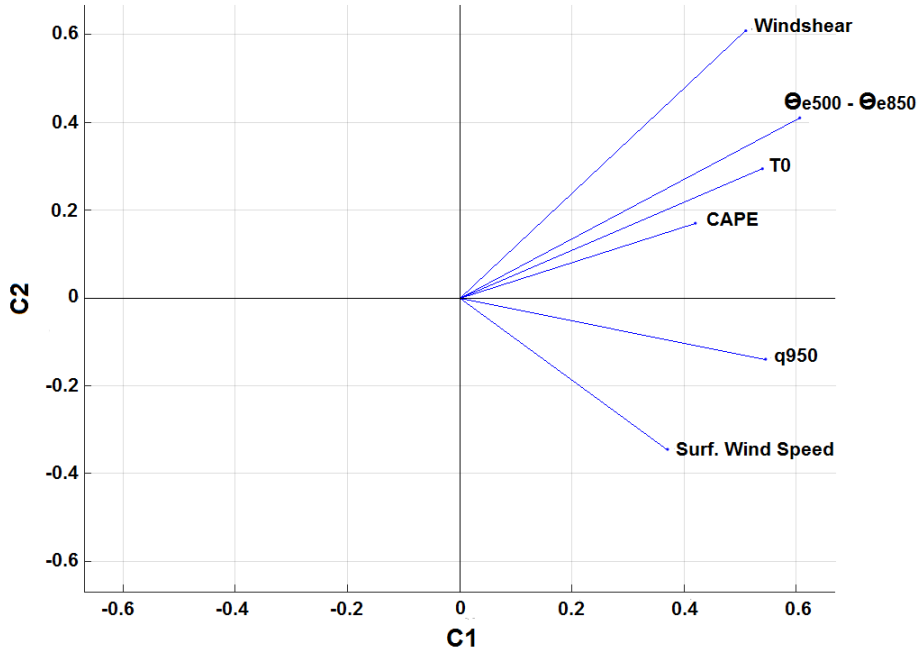

Fig. 5.1.: Principal Component Analysis of the investigated meteorological parameters along the first (C1) and second components (C2).

subtracting the values for all hail days from the mean of the parameter for all days from April to September (and thus combining days with and without hail) from 2005 to 2014. These differences were then divided by the mean of the parameter for all days to obtain relative differences expressed in percentage.

Figure 5.2 represents the relative deviation of geopotential height at 300 hPa during hail days compared to the overall mean (including days with and without hail). Blue areas correspond to lower geopotential during days with hail compared to the mean, and red areas to higher geopotential. Black lines represent the mean .

The mean decreases steadily from the south towards the north of Europe, which is not the case for the anomalies where some patterns can be recognized. In Figure 5.2, the standard deviation ranges from -26 to 28 gpdm compared to the mean (not shown). Negative values are situated over the Atlantic Ocean while positive values are positioned over Central Europe. Negative anomalies may correspond to depressions centered west of Brittany with -23% compared to the mean. An upper-level shallow ridge extends over Central Europe from North Africa to Scandinavia. Enhanced instability explains the formation of convection forming thunderstorms with an increased risk of hail occurrence (Craven and Brooks, 2004). Therefore, areas ahead of low-pressure systems are often associated with convection forming conditions (Van Delden, 1998 and García-Ortega et al., 2012). For example, Schemm et al. (2016) found that 40% of hail during 2002 and 2013 in Switzerland were initiated by fronts (using an automatic front detection

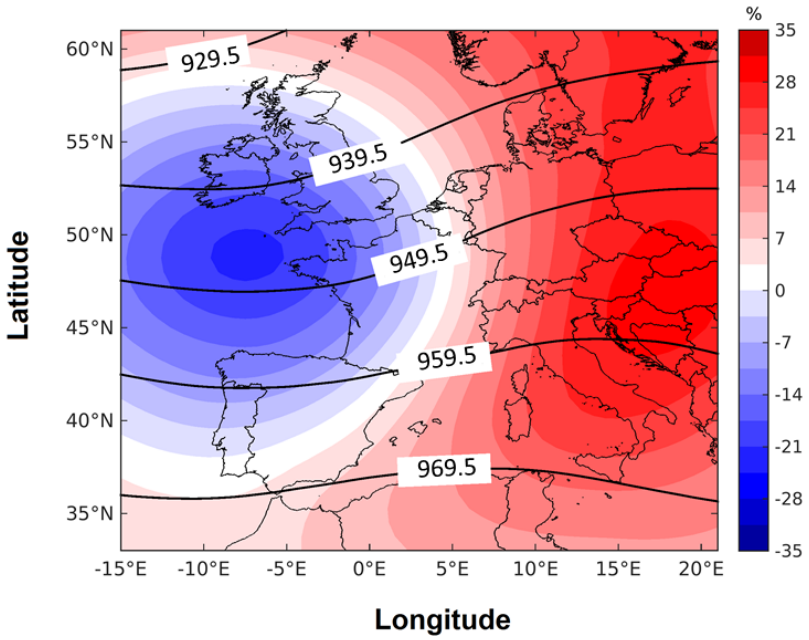

Fig. 5.2.: Anomaly of the 300 hPa geopotential height between days with and without radar-derived hailstorms between 2005 and 2014 (color contours) and mean geopotential height (in gpdm) during hail days (black contour lines).

algorithm). Specific locations of the low-pressure systems in the mean over Brittany and Central Europe lead to a continuous flow coming from Spain and reaching France and Germany from the west-southwest (WSW). This WSW flow is generally found to prevail during severe hail events and covers several European countries, such as France (Vinet, 2001 and Berthet et al., 2011), Spain (García-Ortega et al., 2011), Switzerland (Willemse, 1995; Muriset, 2003 and Schiesser, 1990), and Germany (Kunz, 2007b and Kapsch et al., 2012).

The location and intensity of the jet stream is also a relevant parameter decisive for large-scale properties of air mass (Dayan and Abramski, 1983). Moreover, windspeed at upper levels, as well as wind direction, directly determine the shift of storms (Archer and Caldeira, 2008). Figure 5.3 shows the relative wind speed anomalies at 300 hPa compared to the average and mean during the convective season. The highest values in the mean are found south of Spain. Windspeed decreases smoothly to the southwest and northeast but decreases sharply toward the northwest and east. The jet stream maxima extend straight from the southwest to northeast direction.
On hail days, negative anomalies are situated over the British Isles with a strong decrease from the south of England (-5%) to the north of Scotland (-30 %) suggesting that the variability is higher over this region. A weaker negative pattern is centered over Sicilia and ranges from Tunisia to the south of the Balkans. During hailstorms, the location of the jet stream is shifted northwards from the mean over the

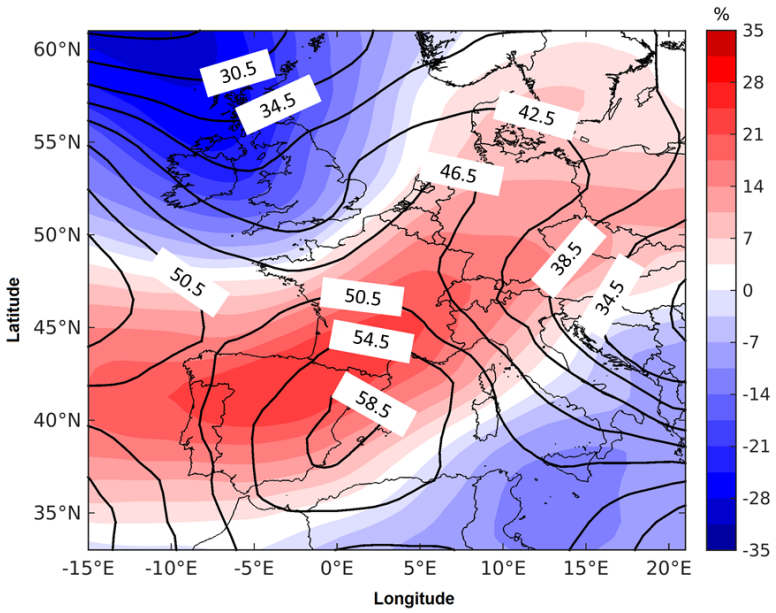

Fig. 5.3.: Same as Figure 5.2 but for wind speed at 300 hPa (in m s^{-1}.)

western part of the Mediterranean Sea. A wide positive anomaly extending from Portugal to northeast Europe (with around +25%) over northern Spain and southern France) indicates that windspeed is more intense over these regions during hail days. This reinforcement of the jet stream over southwestern Europe leads to a strong wind shear favoring hailstorms (Dessens, 1960; Longley and Thompson, 1965). Warm and dry air at mid-tropospheric levels (500 to 700 hPa) coming from the Iberic peninsula spreads towards northwest Europe, denoted as the Spanish plume (Morris, 1986). Such a configuration increases hail potential over western Europe by the creation of low thermal stability, capping inversion and sometimes an elevated mixed layer (EML). The capping inversion is the lower part of the EML. Above the cap, the EML permits the release of instability in the case of lifting in the entire air column (potential instability), thus favoring the development of deep convection. Dry air situated at mid-level scales can, in addition, aid to structure airflows within convective cells. EML and capping inversion configuration are frequent during the initiation of deep convection, for example, an MCS or a derecho, which need strong dynamic forcing. Numerous severe convective storms occurred during a Spanish plume over Europe in the past, for example, the Pentecost storm in June 2014 where several MCSs affected France, Belgium, and Germany and caused around 340 Million euros for insured losses (Verspecht et al., 2014), or the derecho in Belgium in June 2010 which caused several fatalities (Hamid, 2012).

Besides geopotential and wind speed aloft, both shear and CAPE are two other atmospheric properties that are decisive for the development of thunderstorms. Moreover, these two parameters were identified by the PCA in the previous section as important predictors for hailstorms. Because the regional climate

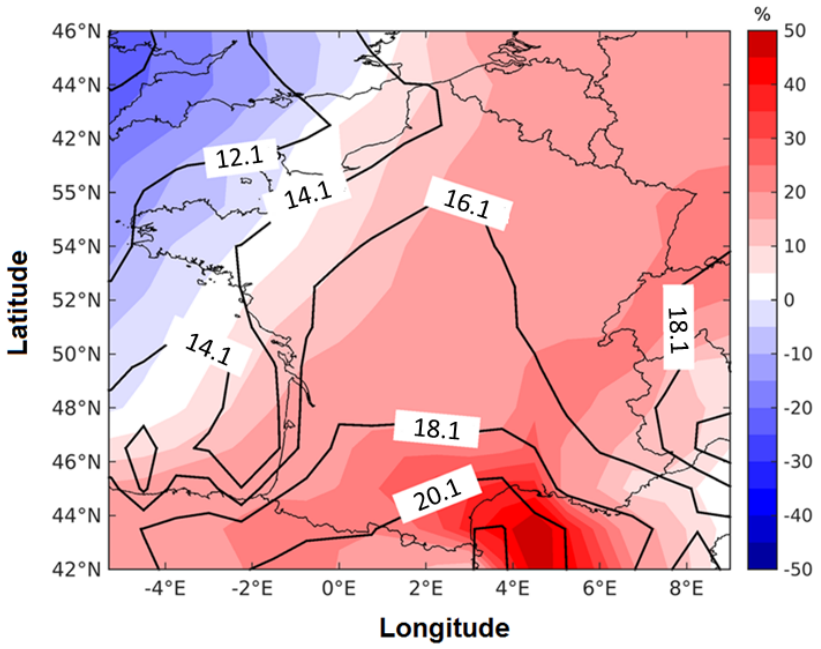

Fig. 5.4.: Relative anomalies of wind shear 0 - 6 km in France, Belgium, and Luxembourg between days with and without hail (color contours) and the mean of the wind shear during hail days (black contour lines).

governs both parameters, anomalies are investigated in the following separately for hailstorms identified over France, Belgium, and Luxembourg from those over Germany.

In Figure 5.4, the mean of the vertical wind shear decreases from southern France (> 20 m s^{-1}) to northwestern France (with 14 m s^{-1}) along the English channel. High positive anomalies in wind shear in France are situated along an SW-NE corridor going from the Pyrenean to the Alps and reaching 19 m s^{-1} at the south of the region Auvergne. This corridor coincides with the location of the highest hail potential in France (see hail climatology in Section 4.1). Values greater than 20 m s^{-1} can be observed in the region Languedoc-Roussillon in southern France. Values between 14 m s^{-1} and 16 m s^{-1} are situated over the northwest and central parts of France, but also over Belgium and Luxembourg where conditions for organized convection are favored. Brittany and the English Channel show lower wind shear values with around 12 m s^{-1}.

The wind shear magnitude on hail days is lower in Germany (Figure 5.5) compared to France, with average values between 16 m s^{-1} in southeast Germany and 14 m s^{-1} over central and north Germany. A strong positive anomaly of +26% is situated south of Bavaria and Baden-Wrttemberg. The anomaly decreases to the north to amounts less than 10% near the coasts.

The strongest positive anomalies of CAPE are situated over the Western Mediterranean (Figure 5.6) with values around +33%. The warm and low-level atmospheric moisture available in this region combined with drier mid-level air coming from Spain or North Africa gives rise to higher CAPE values and creates more instability. Weaker positive anomalies are situated in the rest of France as well as Belgium and Luxembourg due to the higher stability of the vertical profile. The eastern part of France as well as the southwest experiences weaker CAPE values. A cool Atlantic air flow may induce less latent heat than the Mediterranean inflow in the south and, thus, is responsible for weaker potential energy .

Figure 5.7 shows the relative anomalies and mean values of CAPE for Germany. Positive anomalies are situated over the western part of Germany along with a SW to NE axis. This pattern could explain the location of a relevant climatological hail hot spot in western Germany. Mean values of CAPE are highest in southern Germany with up to 1630.9 J kg^{-1} at the southeastern tip of Germany. Low CAPE values are prominent in the west and northeast parts of Germany with values less than 1030 J kg^{-1} centered over the state of Hessen and less than 730 J kg^{-1} near the Baltic Sea. CAPE along the coastlines remains weaker than the inland.

Preferred environments for hailstorms were analyzed at a synoptic and regional scale. The synoptic scale investigation reveals that hailstorms occur preferably ahead of a trough approaching from northwest Europe towards the southeast and during a pronounced jet stream extending from southwest to NE Europe. These upper-level features create favorable conditions for hail development. The strengthening

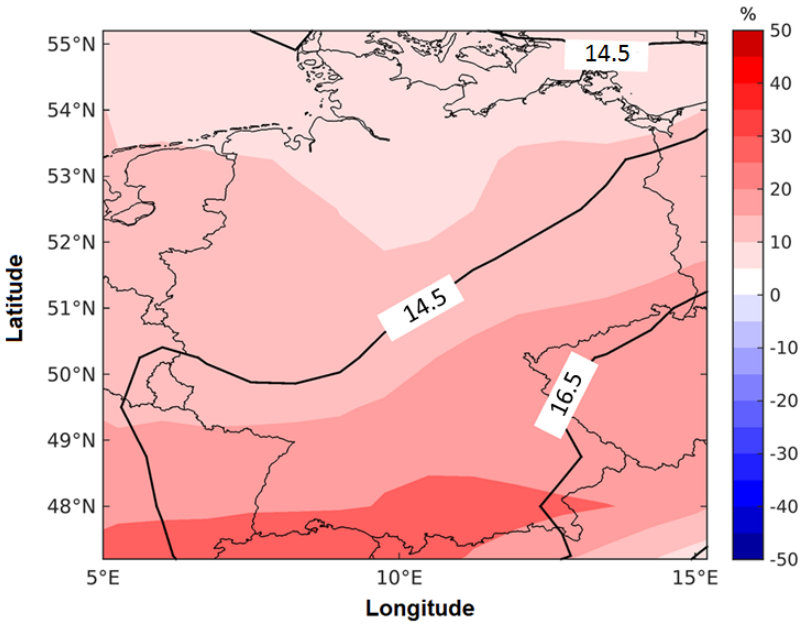

Fig. 5.5.: Same as for Figure 5.4 but for Germany.

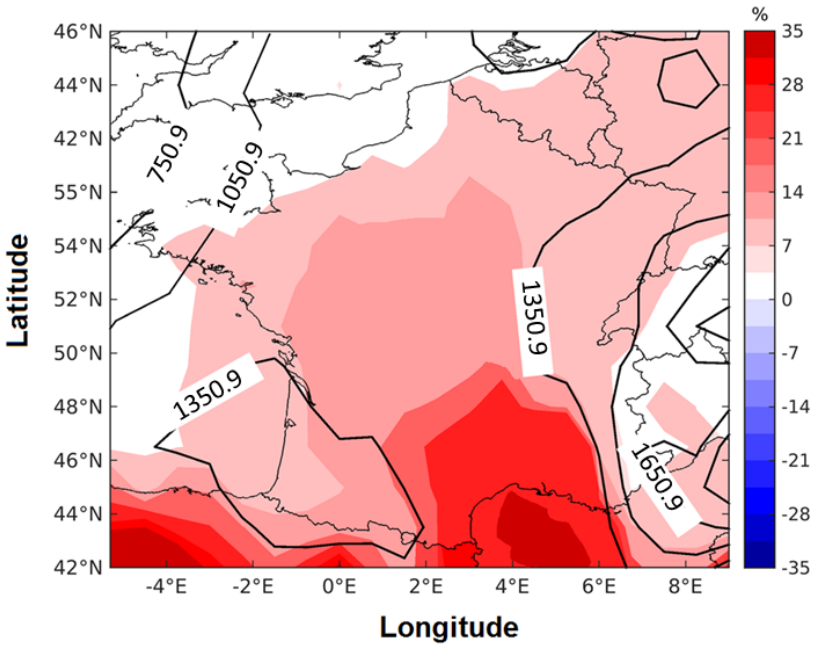

Fig. 5.6.: Same as for Figire 5.4 but for CAPE.

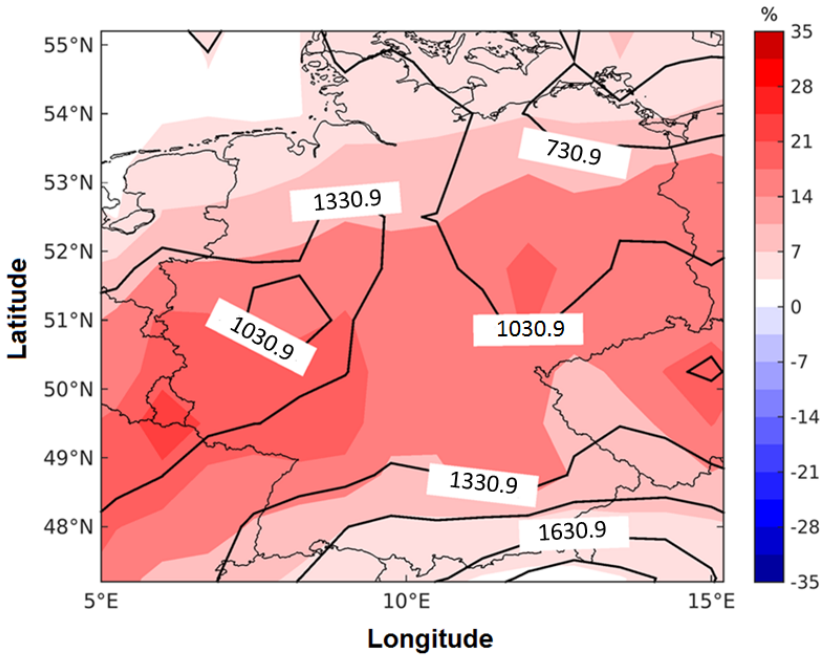

Fig. 5.7.: Same as for Figure 5.6 but for Germany.

of the jet stream permits the intake of dry air from southern Europe to central Europe that mixes with Mediterranean air flows and increases instability. Lifting of air masses, from upper-tropospheric levels (positive vorticity advection, positive divergence at 300 hPa) may be decisive for the triggering of hail-storms.

5.3. Pre-convective environments

In this section, atmospheric conditions prevailing near the first hail streak detection are investigated. The results may be useful for hail warnings. The mean sea level pressure is investigated to confirm the hypothesis of the presence of low-pressure systems in Atlantic. This parameter was also tested in the previous PCA but was not retained in its final display because of the high variance. In addition, the vorticity advection and divergence are analyzed because these parameters indicate vertical lifting. Vorticity advection and divergence were not considered in the PCA because these two variables are highly interdependent, and thus collinear, and their role as pre-convective predictors would be difficult to separate. Two additional parameters already considered in the previous section that play an important role in the trigger of convection are wind shear and CAPE.

For the analysis of ambient conditions, coordinates of hailstorm onsets were first transformed from the HAMLET grid to the nearest grid point of the ERA-Interim grid. Then, an area of 13° × 13°, or approximately 1000 × 1000 km^2, was defined around each starting point of a hail swath. The meteorological fields, computed for all hail events, are shown as mean fields of the respective parameters. They are added up together such that the central point of the composite represents the total number of onsets. Mean sea level pressure is presented in Figure 5.8 with standard deviation, where values range from 925 hPa in the northwest to 1024 hPa in the southwest. As expected, the beginning is located south of the minimum low pressure in an area with a large gradient.
The standard deviation decreases steadily from northwest to southeast of the investigated area. The highest standard deviations are situated in the northwest (+5.8) and spread out slightly from the mean, suggesting the variability is higher northwest of the central point compared to the southeast. This indicates stronger or more frequent depressions over the seas.

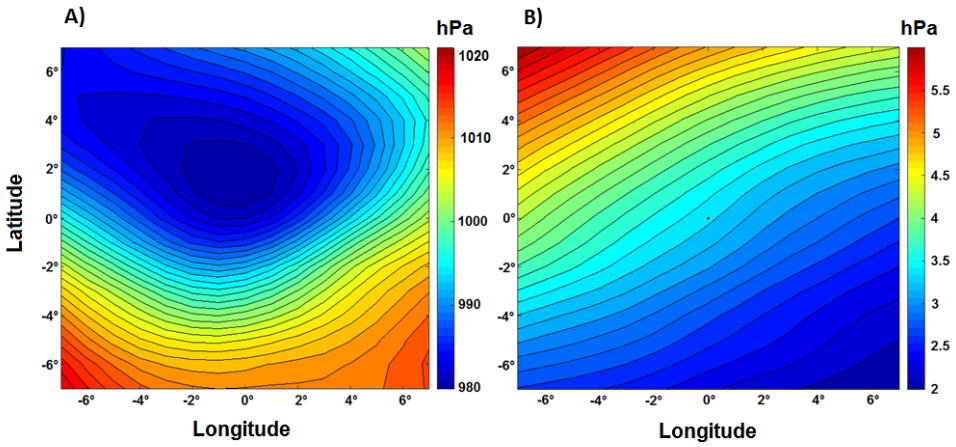

Fig. 5.8.: Composite of mean sea level pressure at 12 UTC for all identified hail streaks initializations between 2005 and 2014 represented by the central black dot (A) and corresponding standard deviation (B).

The mean of the vorticity advection between 300 hPa and 500 hPa is presented in Figure 5.9. The wind at these levels can be considered to be in quasi-geostrophic balance, which is a prerequisite in the Omega equation quantifying the synoptical-scale vertical velocity (Pamdey et al., 1976) as described in Section 2.2. According to the Omega equation, positive values of the composite mean of this parameter (i.e., vorticity advection increasing with height) indicates lifting in the troposphere, which may help air parcels overcome the CIN. Note, however, that differential vorticity is only one term in the Omega equation (Viúdez et al., 1996), which may be compensated by the minimum of temperature advection or adiabatic heat transfers. All events in Figure 5.9 are situated on the eastern edge of a large positive anomaly at differential vorticity advection with $0.35 \cdot 10^{-9}$ s $^{-2}$, hence ahead of a trough in a zone with high gradients. This agrees with the study of Busch (2013) who conducted the same type of study over Germany, but for substantially smaller sample size and without consideration of the first hail streak detection location. This slight difference of vorticity advection magnitude can be due to the much smaller sample size of fewer than 200 events in Busch (2013). Note that a location downstream of an upper tropospheric trough axis is the favorable location for surface low-pressure systems to develop as positive vorticity advection suggests lifting as well as favoring the triggering of hailstorms (Whiteman and Doran, 1993). This is consistent with patterns present in the mean sea level pressure, northwesterly from the central point (Figure 5.8). An analysis of the standard deviation of vorticity advection is meaningless because this parameter does not follow a normal distribution.

Another proxy for large-scale lifting is the divergence at upper levels shown in Figure 5.10. Hailstorms are situated at the eastern flank of the maximum divergence meaning that most of the hail events are connected or even triggered by lifting processes at upper levels. On the other hand, this result is an indication that low-level convergence and, thus, convection triggered in the boundary level may be of less importance for hailstorms. These high values of divergence are related to strong updrafts and long-lived storms (Markowski and Richardson, 2010).

The mean of vertical wind shear, defined as the mean of the wind speed difference between 500 hPa and 1000 hPa, is presented in Figure 5.11. Overall, the shear decreases from the southwest (with a maximum of up to 18.5 m s $^{-1}$) towards the northeast. The shear values at the center of the composite, situated northeast and downstream of the maximum, reach up to 16 m s^{-1}. The center situated in a zone with a strong gradient corresponds to the divergence at 300 hPa. The location downstream of the maximum can be due to the location ahead of a trough where windspeeds usually increase. According to Markowski and Richardson (2010), multicells form preferably when the wind shear is between 10 m and 20 m s^{-1}, whereas supercells require even higher shear starting from approximately 20 m s^{-1}. Considering this assessment, one may assume that the preferable type of event is multicells or supercells.

Figure 5.12 presents the composite median of CAPE as well as the standard deviation. The CAPE near the events reaches around 980 J kg $^{-1}$ to the northwest of a maximum area that reaches up to high values

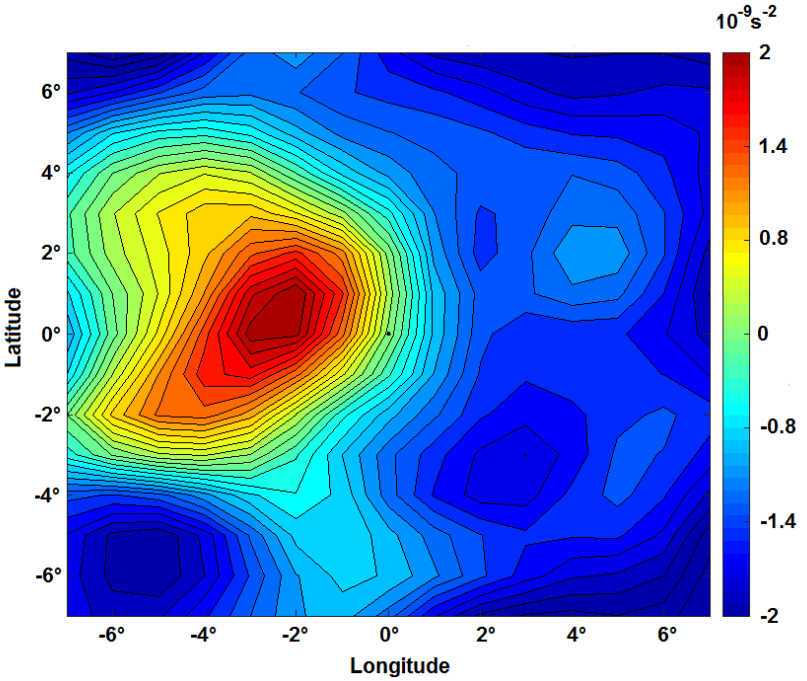

Fig. 5.9.: Difference of the vorticity advection at 12 UTC between 300 and 500 hPa for all identified hail streaks between 2005 and 2014 (central black dot). Positive values suggest a rising of the air according to the Omega equation, while negative values indicate descent.

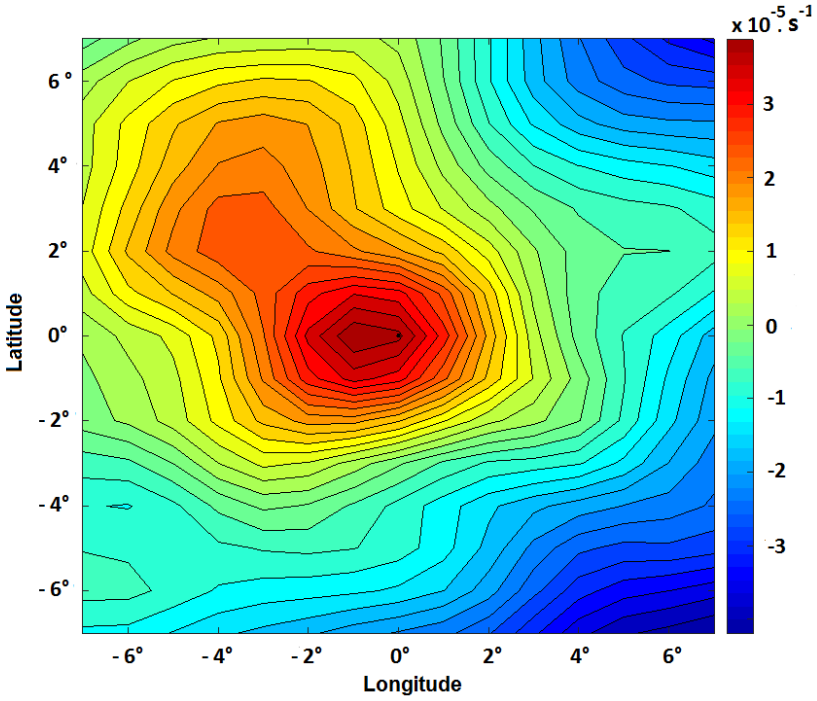

Fig. 5.10.: Same as Fig. 5.9, but for the mean divergence at 300 hPa. Positive values indicate divergence of the air, whereas negative values represent convergence.

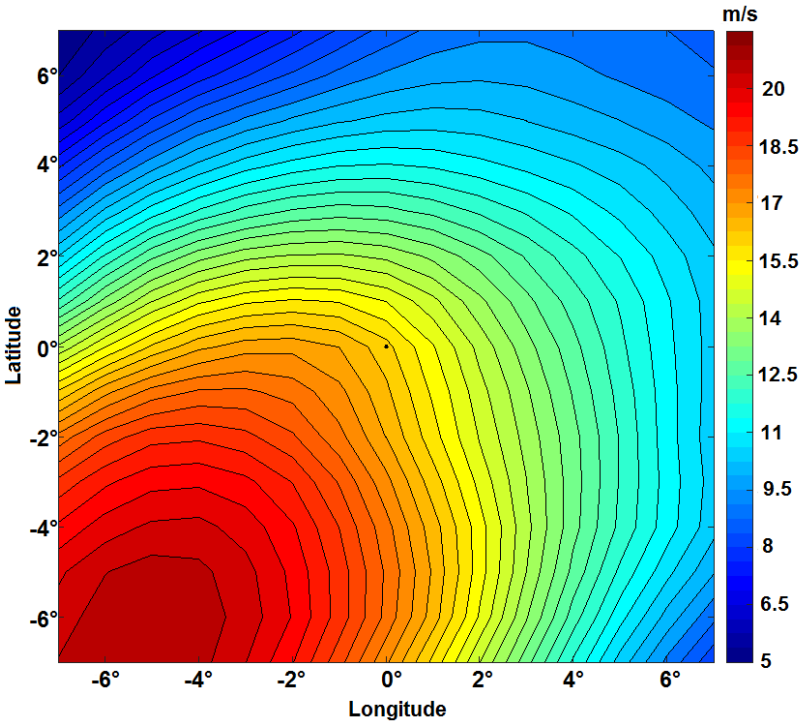

Fig. 5.11.: Same as Figure 5.9, but for the mean of wind shear between 500 and 1000 hPa.

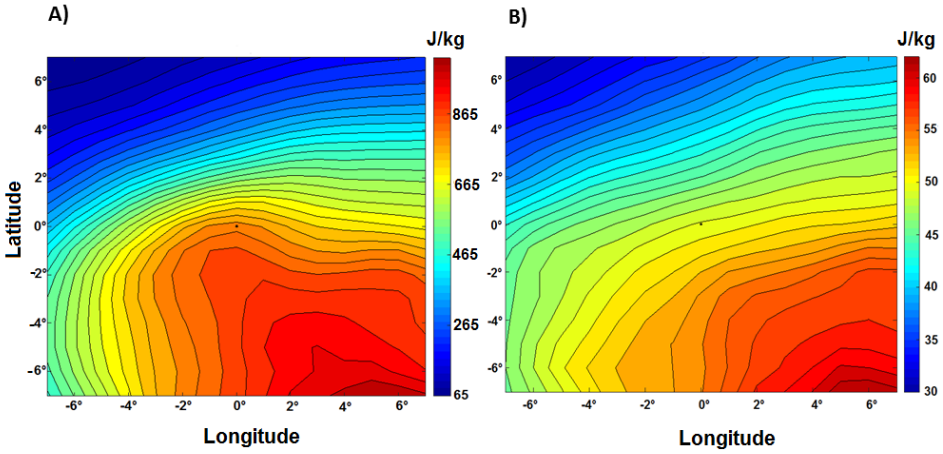

Fig. 5.12.: Same as Figure 5.8, but for the mean CAPE.

of 1165 J kg $^{-1}$. Other studies found lower values in the statistical mean for observed hailstorms (e.g., Busch, 2013; Groenemeijer and van Delden, 2007). When analyzing the standard deviation of CAPE (Figure 5.12), the highest variability is noticed in the southeast areas of the events with maximum CAPE values. This may be due to a higher instability in these regions. The minimum is reported northwest of the events where the location of the trough seems to support tropospheric stability.

5.4. Air mass properties of the 100 most intense storms

In this section, atmospheric environments, as well as hail swath characteristics during the most intense 100 hailstorms (the 100 storms having the highest RCSI), are investigated to identify and quantify the decisive parameters for the development of hailstorms. Conversely to the previous section, the central point of hail swaths (computed by META) is considered instead of the hail streak initial location because the entire spatial extent of the hail swaths is examined, such as the length or the mean swath orientation. Furthermore, the physical characteristics of hail swaths were not considered in the PCA in Section 5.1 because of the high variability of the parameters. In this sample of only 100 hailstorms, the variability of the parameters is lower. A PCA was first computed with several meteorological parameters and so, in contrast with the previous PCA, includes the physical characteristics of the hail swaths, namely the duration, length, width, and mean orientation. Details about the computation of these latter parameters are given in Section 5.1. Furthermore, a radar chart (Robbins, 2012) of severe hail swath features was established to visualize, summarize, quantify, and compare the significant factors during the mature-stages of hailstorms.

5.4.1. Predictors for severe hailstorms

Meteorological parameters in terms of vorticity advection, freezing level, wind shear, CAPE, difference of θ_e surface wind speed, and specific humidity at 950 hPa as well as hail swaths duration, length, and width were considered in a PCA. The coordinates of the hail swath centers were interpolated to the ERA-Interim grid.

Figure 5.13 represents the output of the PCA. The first component separates the higher from lower event frequencies and the second component represents the storm intensity. As for the PCA in the previous section, each variable possesses positive values along C1 and plays a role to explain the values of RCSI. Two variables, specific humidity at 950 hPa and surface wind speed, are negative along C2 while the remaining variables are positive along this axis. Thus, these two parameters seem to have a less important relevance during very severe hailstorms in Western Europe compared to other variables.

The duration possesses the highest values along C2 (+0.61) but only +0.25 along C1 suggesting that intense events are not frequent and explained by their long duration. The length is the second variable with elevated values on C2 (+0.45) and only +0.15 on C1. Thus, this parameter appears to be relevant for severe hail events. As for the duration, the frequency of long events is low, whereas shorter events occur more often. Track width is another parameter that plays a less relevant role during intense events (around +0.3 for both components) than the duration or the length, possibly because the width variability remains low.

For the meteorological parameters, wind shear, vorticity advection, and freezing level T0 are close to each other on the PCA. Indeed, these meteorological parameters interact: organized convection persists due to an influence between sheared environments and intense updrafts, which transport warm low-level

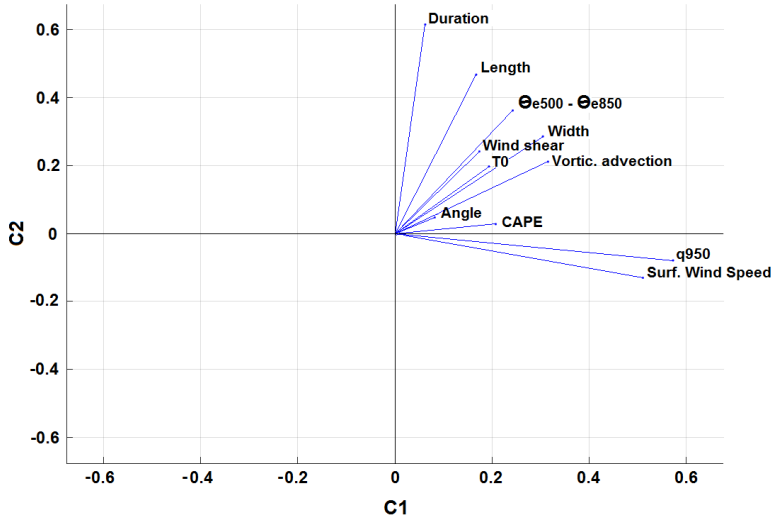

Fig. 5.13.: PCA output of meteorological variables (from ERA-Interim) as well as the hail swaths characteristics (from META) for the most 100 severe hail events between 2005 and 2014 (e.g., the highest RCSI).

air upward (Markowski and Richardson, 2010). Warm air can affect the height of the freezing level. Orientations of hail swaths (denoted Angle in the PCA) have low values along C1 and C2 meaning their role is not crucial for the severity of hailstorms. These can be due to organized cells that cross large areas without low-level effects, such as orographically-induced flow deviations. Interestingly, as mentioned in Section 4.4, the five most severe storms occurred within a deep southwesterly flow coming from Spain or Africa. CAPE is characterized by low values along both axis which may be due to extremely variable CAPE values in climate models. Duration, length, humidity, and surface wind speed are separated by almost 90° meaning that they have independent effects.

In conclusion, duration, length, and instability of the troposphere characterize best the severity of hailstorms in western Europe and it could be interesting to focus on these parameters for further extreme events and hail warnings.

5.4.2. Characteristics of severe hailstorms

The typical signature of the 100 most severe hailstorms is represented in a single chart, which is a graphical method to display multivariate data and easily compare different groups of data. The length of each spoke is proportional to the magnitude of the variable. Figure 5.14 shows a radar chart with five axes corresponding to the number of parameters considered: the total length of a hail swath, its duration, width, orientation, and during which month the event happened. Three different RCSI intervals were chosen for the 100 most severe storms. The lowest value of the severity index is equal to 1,000 while the maximum is 2,124.3. Thus, the interval was set to 375, with the first interval, including RCSI values between 1,000 and 1,375. The values of the second interval are situated between 1,375 and 1,750, and the last interval is set between 1,750 and 2,125. The corresponding parameter values within each group

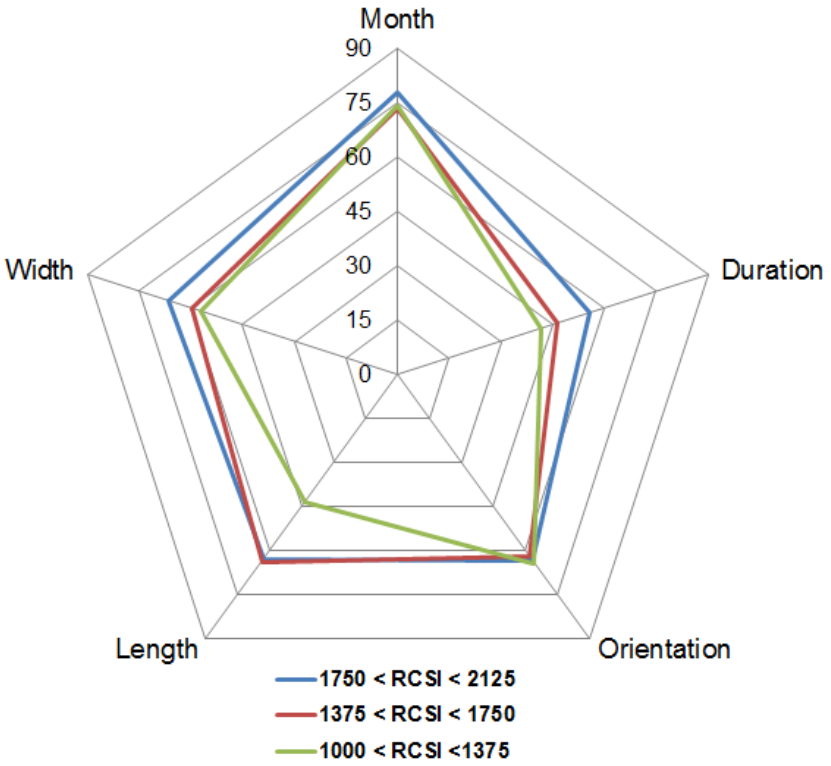

Fig. 5.14.: Radar chart representing the contribution (in %) of five parameters for severe hailstorms development.

were first averaged and then normalized to their maximum. Therefore, maximum values on each radius of the radar chart are 100%. The values 'orientation' and 'month' match among all groups. Indeed, more severe hail events occur principally in July and have an SW to NE direction (between 222° and 231°).

The values of these parameters of the third group (highest RCSI) are closest to their respective maximum suggesting that high values are specific to very severe storms. In contrary, group 1, with the lowest RCSI values, has a low spread. The hail swath length is quite low with only 43.2 % compared to 63.6% for the second group, and 62.8% for the first series. Long duration and high track width characterize the very extreme events.

A list of the 10 most severe hail events with their respective characteristics is given in Table 5.1. The event named Ela, occurring on 9 June 2014, is the most severe hailstorm recorded between 2005 and 2014 with an RCSI of 2,124.3. This hailstorm crossed several countries and had a length of more than 380 km. The second most severe event during the same period was the 30 June 2012 with an RCSI of 2,019.8.

Hail activity during the year 2013 was also particularly important with 5 severe hail events that occurred during this year and RCSI ranging from 1,834 to 1,971.9.

Tab. 5.1.: Characteristics of the 100 most severe hailstorms between 2005 and 2014 (e.g., the highest RCSI values). The length and width are in km, the orientation is in degrees to the azimuth, and the duration is in minutes.

Year	Month	Day	Hour	Minutes	Length	Width	Orientation	Duration	RCSI
2014	6	9	22	30	381.68	13	221.56	135	2124.3
2012	6	30	13	30	560.53	17	227.43	645	2019.8
2013	7	28	15	30	348.91	19	237.89	180	1971.9
2013	7	27	11	45	367.53	16	249.15	420	1934.6
2011	9	11	13	45	187.62	12	223.19	120	1880.1
2013	8	6	14	0	99.55	16	237.59	135	1879
2013	8	21	14	45	477.14	15	216.41	510	1847
2013	6	17	0	0	528.72	14	216.97	450	1834
2007	5	13	10	30	613.49	13	224.76	405	1746.1

6. Discussion and Conclusions

In this study, the spatial and temporal variability of hailstorms in France, Germany, Belgium, and Luxembourg were investigated. For this purpose, a hail climatology was computed for 10 years between 2005 and 2014. Hail events were detected by the combination of different datasets, including radar and lightning data.

A large part of the work was the development of methods for the detection of hail from meteorological data as well as the use of a tracking algorithm (META) with post-processing to reconstruct a large event set of past individual hail swaths. Furthermore, orographic conditions leading to the development of convection as well as pre-convective environments were analyzed.

Conventional meteorological observation systems inadequately detect hailstorms due to their small spatial extent and their partially short lifetime. Area-covering observation systems, such as radar and lightning data, fulfill the prerequisites for detecting convective systems because of their high spatial and temporal resolutions. However, no clear relation to hail can be derived from the individual datasets. Therefore, different observations were combined in a meaningful way to reproduce hail events statistically.

Two-dimensional radar data from the German and French weather services (DWD and Météo France) were used as the most important data source for this study. The high spatial resolution of radar composites (1 km^2) covering large areas in western Europe allowed for detailed estimates of severe convective events. To reduce computer costs, radar data were first separated into two composites: one radar composite included only Germany and the second included France, Belgium, and Luxembourg. The same methods were applied to both composites to perform a homogeneous climatology. First, an extensive correction of errors and clutter was performed. Individual grid points of radar composite with very high radar reflectivity and echoes were eliminated. A correction of radar signals with lightning data was applied next since lightning always occurs in connection with thunderstorms. In a further step, appropriate methods were developed to detect hail in radar data that were filtered with lightning data. The hail criterion of Mason (reflectivities above or equal to 55 dBZ) was applied to 2D radar data. Then, the adapted cell tracking algorithm META based on the algorithm TRACE3D (Handwerker, 2002) was applied to the radar data to reconstruct 30,188 individual hail trajectories in western Europe during the investigation period. An advection correction was applied afterward, since missing data or fast-moving thunderstorms creates gaps in the dataset due to the 5-minute temporal resolution.

After these corrections, hail days derived from radar data were computed. A day with hail is counted when the daily maximum reflectivity values on 1 km^2 overpasses the Mason (1971) criterion of 55 dBZ.

A sum of all hail days between 2005 and 2014 constituted the hail potential, which showed a high spatial and temporal variability within western Europe. While no or only a few radar-derived hail days occurred in the northern parts of Germany, Brittany or along the European coastlines (0-2 hail days), more than 40 hail days were detected on the leeward side of mountain ranges, such as in the Massif Central in France. Other regions frequently affected by hail are located far away from the Atlantic or Mediterranean, such as southwest France, northeast France (regions of Burgundy, Champagne-Ardennes, and Lorraine) or West Germany (states of Hesse, Rhineland-Palatinate, and south of North Rhine-Westphalia). Several hail hotspots are also situated in southern Germany, such as nearby the Swabian Jura with a maximum of 32 hail days or downstream of the Ore mountains (maximum of 23 days with hail) in northeast Germany.

The high spatial variability in the number of radar-derived hail days and the increasing number around orographic structures suggest an influence of the orography on the triggering and amplification of thunderstorms. The investigation of the connection between hail occurrence and orography often shows a maximum of hailstorms downstream the mountains. In the case of wind coming from a southwest direction, this corresponds to the leeward side of obstacles. During days with hail, a go-around regime near the Swabian Jura leads to a low-level moist convergence downstream, which is required for deep moist convection. The same wind features can appear near the Massif Central in France. In this area, positive buoyancy combined with high wind speed during days with hail during the afternoon may permit wind to cross over the mountain, and lead to low convergence downstream.

In addition to the hail potential, the distribution of radar-derived hail days in western Europe was examined in connection with various pre-convective meteorological conditions. It is found that an interaction between several meteorological factors on different spatial and temporal scales (from the synoptic to regional scales) favor the triggering and development of hailstorms. Indeed, the investigation reveals that hailstorms occur preferably south of a trough approaching from northwest Europe and during a pronounced jet stream extending from southwestern to northeastern Europe. These upper-level features create favorable conditions at the middle and lower troposphere for DMC. The detected strengthening of the jet stream permits the intake of dry air from southern Europe into central Europe (for example, during a Spanish plume) that, combined with moist (Mediterranean) air advection at lower levels, are favorable environments for deep convection. The lifting of air masses from upper-tropospheric levels, revealed by positive vorticity advection in combination with high amounts of moisture and CAPE values, seems to be favorable factors for hailstorms. Furthermore, high wind shear present in the mean particularly over southern France and southern Germany influences the development of organized cells in these regions. Dynamic forcing and vertical motions induced by the orography results in the rise of air, especially at nearby mountains. On the leeward side, low-level convergence associated with gravity waves induced by obstacles has a core role in the triggering of hailstorms.

According to a Principal Component Analysis (PCA), both wind shear and stability/instability (in terms of the difference of equivalent potential temperatures between 500 hPa and 850 hPa) of air masses

appear o be two important factors for the development of organized convective cells. A severity index was also performed for each past hailstorm. Very severe hailstorms generally occur with a long and wide trajectory, long duration, and within a very unstable environment favorable for deep moist convection.

Using radar data to derive a hail probability map includes several limitations and shortcomings inherent in the available data sets. First, radar data for the large investigation area are only available as 2D radar reflectivity from the German and French weather services. The use of both C-band and S-band radars in the French composite implies a certain amount of inhomogeneity. However, tests for individual days have shown that the detected tracks, including their reflectivity, do not show variations that are related to the different radar bands. Another problem is the relatively frequent failure of radar systems. In some cases, radar stations were out of operation all year round, resulting in less accurate or absence of coverage in the respective area. Shorter gaps in the datasets were known but could not be fully considered in this work due to their multiplicity. Therefore, some minima appearing in the climatology of the radar-derived hail days maybe because of these gaps. However, the downtime of the radars only affects approximately 2 to 8% of all possible days, which leads to a maximum estimated uncertainty of 10% suggesting the spatial distribution is reasonably unaffected. False echoes can also occur in radar data, especially near radar locations (Puskeiler, 2013). Furthermore, the radar coverage plays an important role in the number of hail days detected. Indeed, the radar coverage density is less important in the northwestern part of France, leading presumably to an underestimation in the number of hail days in this region. Furthermore, the northern part of Belgium is only partly covered by the radar station of Avesnes located in northern France. The long distance to the radar location added to radar failure can explain the low hail-frequency over Belgium. The Alps remain a gap in the French composite because radar stations do not yet cover this region. A recent installation of new X-band radars in the Alps need calibration and validation before data can be integrated into the national composite. The radar coverage is also not accurate in the edge of southeast Germany, which may explain the gap of hail days in this area.

Despite the various errors in the radar data described above, the final results are reasonably robust. For example, good correlation is shown between the distribution of hail near the Swabian Jura areas in both this thesis and the study of Puskeiler (2013), although 3D radar data were used in the latter case. The distribution of hail in western Europe is also similar to large-scale structures of satellite-estimated hail probability by Punge et al. (2014) data. Therefore, the results are based on the best possible accuracy achieved with these data.

With the findings gained in this work, the development of a hail damage model was performed at the reinsurance company Tokio Millennium Re. In the future, an improvement of the results can be achieved by considering longer periods, especially in the subdomains highly exposed to hail. More accurate detection of hail could be achieved, especially in mountainous terrains, using the new X-band radar in the Alps. A detailed and high-resolution investigation of wind flows on the leeward side with the unique use of radar data is impossible, and therefore other local observations should be used for

nearby mountains. For example, an investigation of the Froude number, which is a measure of the flow regime conditions due to nearby obstacles, should be investigated to find further evidence of the flow around regime to be decisive for the increased frequency of hail days downstream of several mountains. These additional observations may help to better understand the effects of orography on the triggering of convection and the generation of gravity waves.

Acknowledgements

Many people contributed to the success of this thesis for whom I would like to thank.
All my gratitude amounts to my supervisor, Prof. Dr. Michael Kunz, who always pushed me to give the best. He had a great patience and always answered my questions. He spent a lot of time to correct this thesis, even as he was very busy. Therefore, it was a pleasure to work with him. He is also a very comprehensive person that adapts fast to each situation. His gastronomy tastes, especially by choosing red wine, reminded me home.
Thank you to Prof. Dr. Kottmeier for accepting me as a PhD student at the Institute and being co-referee for this work. He gave useful feedback for my thesis and always finds the best opportunities for his students.
The reinsurance Tokio Millennium Re AG made it possible to finance the project HAMLET. I would like to thank especially Mister Peter Geissbhler, Head of Nat Cat, by the insurance company and Senior Cat Analyst Stefan P. Ritz for their fruitful work. We achieved rigorous work within a good atmosphere, and I wish them all the best for developing HAMLET.
GRACE school, especially Andreas Schenck, gave me the opportunity to access scholarships and participate in great workshops and winter schools, such as at Masada, in Israel where I discovered this country. Thank you so much for all your efforts!
My working group was composed of wonderful people. My very nice officemate Heinz-Jürgen always supported me in every situation. He was at first extremely helpful for programming issues, especially during GIS failures. He is also a great cyclist who comes EVERY day to work with the bike, even with rain, snow, strong winds or illness. He helped me to improve my cycling skills, and I will miss our trainings. Thank you to the other members of the working group, including Manuel Schmidberger, Susanna Mohr, David Piper, Florian Ehmele, and Sven Baumark. They constituted a young, dynamic, and efficient group. Their feedback was always very useful. It was also nice to go skiing with them in Alpbachtal (Austria), especially by the apres-ski with some homemade Schnaps of Monni.
I also had a very good time with all colleagues of the IMK-TRO. With many of them I had the pleasure to do outdoor activities, including road cycling, which permitted me to visit almost all southwest Germany with Enrico, Florian, and Christian as well as Rik and Axel. With my girls Hilke, Luisa, Eva, Julia, and Katharina we loved to meet for baking, cooking or swimming.
Thank you to my other colleagues, Jutta, Manuela, Philipp, Friederike, Bianca, Vera, Sebastian, Alberto, Hans, Gregor, Tobias, and Rowell for eating and going out together. I spent great times with you, and I will visit you whenever I can. Thank you to the other members of IMK. The atmosphere was very good

and relaxed.
Doris Stenschke, Frederike Schoenbein, Silvia Deckert, and Rosie Gräbner were very helpful for administrative documents and very nice people. They always tried to help me and gave their best. It was a pleasure to have them at my side.
Gerhard Brückel and Gabi Klinck were available in case of IT critical issues, and made a very serious effort to help. Thank you for the nice discussions.
Thank you to my friends in France, and so it is time for me to switch to French: Merci tout particulièrement à Stephanie et Jonathan qui m'ont toujours soutenue et accueillie dans leur merveilleuse demeure! Vous avez toujours été d'un énorme soutien et vous me manquez! Bravo Priscilla pour ton courage dans ton metier d'infirmière. Ta force m'a beaucoup encouragée: Machs geut! Merci Aurélien: On s'est serré les coudes ensemble à Karlsruhe. Egalement merci à Florian qui m'a permis de connaitre de formidables personnes telles que Maxime, Natacha, Felix et j'en passe..j'en garde d'excellents souvenirs! Merci à la petite amie de Heinz-Jürgen Lucie avec qui j'ai toujours pu discuter librement de mes soucis outre-Rhin et jouer au mini-golf.
Special regards to my family, including my grandfather of 94 years who has an unbelievable energy that always gave me courage. My brother and father helped me overcome the distance that separates us and provided much humor that keeps me smiling. All my respect amounts to my dear mum, who supported me despite her long and difficult disease. Good luck for the future.

Of course, thanks to my boyfriend who permitted me to reach mountain summits with the road bike and who always supported me.

A. Bibliography

Admirat, P., 1973: Natural hailcores and their abilities to estimate the efficiency of hail prevention systems. *Proc. WMO/ IAMAP Sci. Conf. Wea. Modification*, 197–206.

Amburn, S. A., and P. L. Wolf, 1997: Vil density as a hail indicator. *Wea. Forecasting*, **12 (3)**, 473–478.

Amorati, R., P. Alberoni, V. Levizzani, and S. Nanni, 2000: IR-based satellite and radar rainfall estimates of convective storms over northern Italy. *Meteor. App*, **7 (1)**, 1–18.

AMS, 2000: *Glossary of Meteorology. Second Edition*. American Meteorol. Soc., Bosten, United States, 855 pp.

Archer, C. L., and K. Caldeira, 2008: Historical trends in the jet streams. *Geophys. Res. Lett*, **35 (8)**, 8.

Auer, A. H., 1972: Distribution of graupel and hail with size. *Mon. Wea. Rev.*, **100 (5)**, 325–328.

Auer, J., and H. August, 1994: Hail recognition through the combined use of radar reflectivity and cloud-top temperatures. *Mon. Wea. Rev.*, **122 (9)**, 2218–2221.

Banta, R. M., 1990: The role of mountain flows in making clouds. *Meteorol. Monographs., Amer. Meteor. Soc.*, 229–283.

Banta, R. M., and C. Barker Schaaf, 1987: Thunderstorm genesis zones in the Colorado Rocky Mountains as determined by traceback of geosynchronous satellite images. *Mon. Wea. Rev.*, **115 (2)**, 463–476.

Bartels, H., E. Weigl, T. Reich, P. Lang, A. Wagner, O. Kohler, N. Gerlach, and Coauthors, 2004: Projekt RADOLAN–Routineverfahren zur Online-Aneichung der Radarniederschlagsdaten mit Hilfe von automatischen Bodenniederschlagsstationen (Ombrometer). *Deutscher Wetterdienst, Hydrometeor.*, **5**, 12.

Barthlott, C., U. Corsmeier, C. Meißner, F. Braun, and C. Kottmeier, 2006: The influence of mesoscale circulation systems on triggering convective cells over complex terrain. *Atmos. Res.*, **81**, 150–175.

Barton, D. K., 1988: Modern radar system analysis. *Norwood, MA, Artech House*, **1**, 607.

Bastin, S., P. Drobinski, A. Dabas, P. Delville, O. Reitebuch, and C. Werner, 2005: Impact of the Rhône and Durance valleys on sea-breeze circulation in the Marseille area. *Atmos. Res.*, **74 (1)**, 303–328.

Batt, R., 1991: The radar war: Winning the war of the airwaves. *Robert Hale Ltd*, **4**, 207.

Battan, L. J., 1973: *Radar observation of the atmosphere*. The University of Chicago Press, Chicago, 324 pp.

Bean, B. R., and E. Dutton, 1966: *Radio meteorology*. Dover Publications, New York, 435 pp.

Beard, K. V., and H. T. Ochs, 1984: Collection and coalescence efficiencies for accretion. *J. Geophys. Res*, **89 (D5)**, 7165–7169.

Bedka, K., 2011: Overshooting cloud top detections using MSG SEVIRI Infrared brightness temperatures and their relationship to severe weather over Europe. *Atmos. Res.*, **99**, 175–189.

Berthet, C., J. Dessens, and J. L. Sanchez, 2011: Regional and yearly variations of hail frequency and intensity in France. *Atmos. Res.*, **100 (4)**, 391–400.

Berthet, C., E. Wesolek, J. Dessens, and J. L. Sanchez, 2013: Extreme hail day climatology in Southwestern France. *Atmos. Res.*, **123**, 139–150.

Billingsley, J. B., 1993: *Ground clutter measurements for surface-sited radar*. Massachusetts Inst. Tech., Chicago, 14 pp.

Blahak, U., 2005: Analyse des Extinktionseffektes bei Niederschlagsmessungen mit einem C-Band Radar anhand von Simulation und Messung. Ph.D. thesis, Karlsruhe Institute of Technology, 309 pp.

Bluestein, H. B., G. T. Marx, and M. H. Jain, 1987: Formation of mesoscale lines of precipitation: Nonsevere squall lines in Oklahoma during the spring. *Mon. Wea. Rev.*, **115**, 2719–2727.

Bolton, D., 1980: The computation of equivalent potentail temperature. *Mon. Wea. Rev.*, **108**, 1046–1053.

Bringi, V., T. A. Seliga, and E. A. Mueller, 1982: First comparisons of rainfall rates derived from radar differential reflectivity and disdrometer measurements. *IEEE Trans. Geos. Remote Sensing*, **2 (2)**, 201–204.

Brooks, H. E., J. W. Lee, and J. P. Craven, 2003: The spatial distribution of severe thunderstorm and tornado environments from global reanalysis data. *Atmos. Res.*, **67**, 73–94.

Browning, K. A., and G. B. Foote, 1976: Airflow and hail growth in supercell storms and some implications for hail suppression. *Quart. J. Roy. Meteor. Soc.*, **102 (433)**, 499–533.

Browning, K. A., and F. H. Ludlam, 1962: Airflow in convective storms. *Quart. J. Roy. Meteor. Soc.*, **88 (376)**, 117–135.

Burton, E., and W. Oliver, 1935: The crystal structure of ice at low temperatures. *Proc. Roy. Soc. London*, **153 (878)**, 166–172.

Busch, M., 2013: Untersuchung der Luftmasseneigenschaften und ihrer Transformation bei schweren Hagelereignissen über Europa. M.S. thesis, Karlsruhe Institute of Technology, 100 pp.

Calderbank, R., S. D. Howard, and B. Moran, 2009: Waveform diversity in radar signal processing. *Sig. Proc. Mag.*, **26 (1)**, 32–41.

Castellano, N., C. Scavuzzo, O. Nasello, G. Caranti, and L. Levi, 1994: A comparative study on hailstone trajectories using different motion equations, drag coefficients and wind fields. *Atmos. Res.*, **33 (1-4)**, 309–331.

Caylor, I., and V. Chandrasekar, 1996: Time-varying ice crystal orientation in thunderstorms observed with multiparameter radar. *Trans. Geosc. Remote Sensing*, **34 (4)**, 847–858.

Changnon, S. A., 1977: The scale of hail. *J. Appl. Meteorology*, **16 (9)**, 626–648.

Changnon, S. A., 1993: Relationships between thunderstorms and cloud-to-ground lightning in the united states. *J. Appl. Meteorology*, **32 (1)**, 88–105.

Chappell, C. F., 1986: *Quasi-stationary convective events*. Springer, London, 289–310 pp.

Chen, X., and Y. Liu, 2005: An advanced 3D boundary element method for characterizations of composite materials. *Eng. Analys. Bound.*, **29 (6)**, 513–523.

Cheng, L., and M. English, 1983: A relationship between hailstone concentration and size. *J. Atmos. Sci.*, **40 (1)**, 204–213.

Chu, C.-M., and Y.-L. Lin, 2000: Effects of orography on the generation and propagation of mesoscale convective systems in a two-dimensional conditionally unstable flow. *J. Atmos. Sci*, **57 (23)**, 3817–3837.

Chỳlek, P., 1976: Partial-wave resonances and the ripple structure in the mie normalized extinction cross section. *JOSA*, **66 (3)**, 285–287.

Clements, C. B., C. D. Whiteman, and J. D. Horel, 2003: Cold-air-pool structure and evolution in a mountain basin: Peter Sinks, Utah. *J. Appl. Meteorology*, **42 (6)**, 752–768.

Collin, R. E., 1985: *Antennas and radiowave propagation*. McGraw-Hill College, New York, 508 pp.

Cooper, W. A., 1986: *Ice initiation in natural clouds*. Springer, London, 29–32 pp.

Cotton, W. R., R. L. George, P. J. Wetzel, and R. L. McAnelly, 1983: A long-lived mesoscale convective complex. part i: The mountain-generated component. *Mon. Wea. Rev.*, **111 (10)**, 1893–1918.

Craven, J. P., and H. E. Brooks, 2004: Baseline climatology of sounding derived parameters associated with deep, moist convection. *Nat. Wea. Digest*, **28**, 13–24.

Cummins, K. L., M. J. Murphy, E. A. Bardo, W. L. Hiscox, R. B. Pyle, A. E. Pifer, and Coauthors, 1998: A combined TOA/MDF technology upgrade of the US National Lightning Detection Network. *J. Geophys. Res*, **103 (D8)**, 9035–9044.

Damian, T., 2011: Blitzdichte im Zusammenhang mit Hagelereignissen in Deutschland und Baden-Württemberg. M.S. thesis, Karlsruhe Institute of Technology, 65 pp.

Dayan, U., and R. Abramski, 1983: Heavy rain in the middle east related to unusual jet stream properties. *Bull. Am. Meteorol. Soc.*, **64 (10)**, 1138–1140.

Dee, D., and Coauthors, 2011: The ERA-Interim reanalysis: Configuration and performance of the data assimilation system. *Quat. J. Roy. Meteor. Soc.*, **137 (656)**, 553–597.

Defant, F., 1951: *Local winds*. Springer, London, 17 pp.

Dessens, H., 1960: Severe hailstorms are associated with very strong winds between 6,000 and 12,000 meters. Wiley Online Library, 333–338.

Dessens, J., 1986: Hail in southwestern France. I: Hailfall characteristics and hailstorm environment. *J. Comp. App. Mathem*, **25 (1)**, 35–47.

Dessens, J., C. Berthet, and J. Sanchez, 2015: Change in hailstone size distributions with an increase in the melting level height. *Atmos. Res.*, **158**, 245–253.

Dessens, J., and R. Fraile, 1994: Hailstone size distributions in southwestern France. *Atmos. Res.*, **33 (1)**, 57–73.

Doran, J., M. Wesely, R. McMillen, and W. Neff, 1989: Measurements of turbulent heat and momentum fluxes in a mountain valley. *J. Appl. Meteorology*, **28 (6)**, 438–444.

Dörnbrack, A., and T. Dürbeck, 1998: Turbulent dispersion of aircraft exhausts in regions of breaking gravity waves. *Atmos. Envir.*, **32 (18)**, 3105–3112.

Doswell III, C. A., and P. M. Markowski, 2004: Is buoyancy a relative quantity? *Mon. Wea. Rev.*, **132 (4)**, 853–863.

Doswell III, C. A., and E. N. Rasmussen, 1994: The effect of neglecting the virtual temperature correction on CAPE calculations. *Wea. Forecasting*, **9**, 619–623.

Dotzek, N., 2003: An updated estimate of tornado occurrence in europe. *Atmos. Res.*, **67**, 153–161.

Dotzek, N., P. Groenemeijer, B. Feuerstein, and A. M. Holzer, 2009: Overview of ESSL's severe convective storms research using the European Severe Weather Database ESWD. *Atmos. Res.*, **93**, 575–586.

Doviak, R. J., and D. S. Zrnic, 2014: *Doppler Radar & Weather Observations*. Academic press, 470 pp.

Durran, D. R., and J. B. Klemp, 1987: Another look at downslope winds. part ii: Nonlinear amplification beneath wave-overturning layers. *J. Atmos. Sci.*, **44 (22)**, 3402–3412.

DWD, 2011: RADOLAN/RADVOR-OP- Beschreibung des Kompositformats. Tech. rep., *Deutscher Wetterdienst*, 19 pp.

Dymarska, M., B. J. Murray, L. Sun, M. L. Eastwood, D. A. Knopf, and A. K. Bertram, 2006: Deposition ice nucleation on soot at temperatures relevant for the lower troposphere. *J. Geophys. Res*, **111 (D4)**.

Eccel, E., P. Cau, K. Riemann-Campe, and F. Biasioli, 2012: Quantitative hail monitoring in an alpine area: 35-year climatology and links with atmospheric variables. *Int. J. Climatol.*, **32 (4)**, 503–517.

Egger, J., 1990: Thermally forced flows: Theory. *Atmospheric processes over complex terrain*, Springer, 43–58.

Eliassen, A., 1962: On the vertical circulation in frontal zones. *Geophys. Publ.*, **24 (4)**, 147–160.

Fletcher, N., 1958: Size effect in heterogeneous nucleation. *J. Chem. Phys.*, **29 (3)**, 572–576.

Fouillet, A., and Coauthors, 2008: Has the impact of heat waves on mortality changed in France since the European heat wave of summer 2003? A study of the 2006 heat wave. *Int. J. Epidem.*, **37 (2)**, 309–317.

Fujita, M., H. Nakatsuka, H. Nakanishi, and M. Matsuoka, 1979: Backward echo in two-level systems. *Physical Review Letters*, **42 (15)**, 974.

Fujita, T. T., 1973: Proposed characterization of tornadoes and hurricanes by area and intensity. *Sat. and Mesometeor. Res.*, **97**, 37.

Fulton, R. A., J. P. Breidenbach, D.-J. Seo, D. A. Miller, and T. O'Bannon, 1998: The WSR-88D rainfall algorithm. *Weather and Forecasting*, **13 (2)**, 377–395.

García-Ortega, E., L. López, and J. L. Sánchez, 2011: Atmospheric patterns associated with hailstorm days in the Ebro Valley, Spain. *Atmos. Res.*, **100 (4)**, 401–427.

García-Ortega, E., A. Merino, L. López, and J. L. Sánchez, 2012: Role of mesoscale factors at the onset of deep convection on hailstorm days and their relation to the synoptic patterns. *Atmos. Res.*, **114–115**, 91–106.

Germann, U., G. Galli, M. Boscacci, and M. Bolliger, 2006: Radar precipitation measurement in a mountainous region. *Quart. J. Roy. Meteor. Soc.*, **132 (618)**, 1669–1692.

Gertzman, H. S., and D. Atlas, 1977: Sampling errors in the measurement of rain and hail parameters. *J. Geophys. Res*, **82 (31)**, 4955–4966.

Ginouves, J., 1978: Peut-on utiliser les données des assurances grêle en france pour évaluer les résultats d'une operation de suppression de ce fléau? *J. Atm. Oc. Tech.*, **16 (1)**, 120–128.

Gourley, J. J., P. Tabary, and J. Parent du Chatelet, 2006: Data quality of the Meteo-France C-band polarimetric radar. *J. Atmos. Oc. Tech*, **23 (10)**, 1340–1356.

Graf, M. A., M. Sprenger, and R. W. Moore, 2011: Central European tornado environments as viewed from a potential vorticity and Lagrangian perspective. *Atmos. Res.*, **101**, 31–45.

Greene, D. R., and R. A. Clark, 1972: Vertically integrated liquid water: A new analysis tool. *Mon. Wea. Rev.*, **100 (7)**, 548–552.

Groenemeijer, P., 2009: Convective storm development in contrasting thermodynamic and kinematic environments. Ph.D. thesis, Karlsruhe Institute of Technology, 96 pp.

Groenemeijer, P., and T. Kühne, 2014: A climatology of tornadoes in Europe: Results from the European Severe Weather Database. *Mon. Wea. Rev.*, **142 (12)**, 4775–4790.

Groenemeijer, P. H., and A. van Delden, 2007: Sounding-derived parameters associated with large hail and tornadoes in the Netherlands. *Atmos. Res.*, **83**, 473–487.

Gross, G., and F. Wippermann, 1987: Channeling and countercurrent in the upper rhine valley: Numerical simulations. *J. Appl. Meteorology*, **26 (10)**, 1293–1304.

Gudd, M., 2004: Gewitter und Gewitterschäden im südlichen hessischen Berg-und Beckenland und im Rhein-Main-Tiefland 1881 bis 1980. Ph.D. thesis, University of Mainz, 583 pp.

Gunn, R., and G. D. Kinzer, 1949: The terminal velocity of fall for water droplets in stagnant air. *J. Meteor.*, **6 (4)**, 243–248.

Haiden, T., Kann, A ., Wittmann, C ., Pistotnik, G., Bica, B ., and Gruber, C., 2011: The Integrated Nowcasting through Comprehensive Analysis (INCA) system and its validation over the Eastern Alpine region. *Wea. Forecasting*, **26 (2)**, 166–183.

Hamid, K., 2012: Investigation of the passage of a derecho in Belgium. *Atmos. Res.*, **107**, 86–105.

Handwerker, J., 2002: Cell Tracking with TRACE3D: a New Algorithm. *Atmos. Res.*, **61**, 15–34.

Harris, J., N. Gettys, P. Kenneth, and D. Shin, 2000: Comparison of freezing-level altitudes from the NCEP reanalysis with TRMM precipitation radar brightband data. *J. Clim*, **13 (23)**, 4137–4148.

Hennemuth, B., 1986: Thermal asymmetry and cross-valley circulation in a small alpine valley. *Bound. Lay. Meteorol.*, **36 (4)**, 371–394.

Hermida, L., L. López, A. Merino, C. Berthet, E. García-Ortega, J. L. Sánchez, and J. Dessens, 2015: Hailfall in Southwest France: Relationship with precipitation, trends and wavelet analysis. *Atmos. Res.*, **156**, 174–188.

Heymsfield, A. J., 1978: The characteristics of graupel particles in northeastern Colorado cumulus congestus clouds. *J. Atmos. Sci.*, **35 (2)**, 284–295.

Heymsfield, A. J., P. N. Johnson, and J. E. Dye, 1978: Observations of moist adiabatic ascent in northeast Colorado cumulus congestus clouds. *J. Atmos. Sci.*, **35**, 1689–1703.

Heymsfield, A. J., and M. Kajikawa, 1987: An improved approach to calculating terminal velocities of plate-like crystals and graupel. *J. Atmos. Sci.*, **44**, 1088–1099.

Hohl, R., H.-H. Schiesser, and I. Knepper, 2002: The use of weather radars to estimate hail damage to automobiles: an exploratory study in Switzerland. *Atmos. Res.*, **61 (3)**, 215–238.

Holleman, I., 2001: Hail detection using single-polarization radar. Tech. rep., *Koninklijk Institute of Netherlands*, 71 pp.

Holton, J. R., 2004: *An introduction to dynamic meteorology*. Academic press, San Diego, 535 pp.

Hooper, J., and A. Kippax, 1950: The bright band: A phenomenon associated with radar echoes from falling rain. *Quat. J. Roy. Meteor. Soc*, **76 (328)**, 125–132.

Houze, R. A., 1993: *Cloud Dynamics*. Academic Press, 570 pp.

Houze, R. A., 2004: Mesoscale convective systems. *Rev. Geophys.*, **42 (4)**, 43.

Huggel, A., W. Schmid, and A. Waldvogel, 1996: Raindrop size distributions and the radar bright band. *J. Appl. Meteorology*, **35 (10)**, 1688–1701.

Hughes, P., 1983: A high-resolution radar detection strategy. *IEEE Trans. Aeros. Elec. Sys.*, **(5)**, 663–667.

Johns, R. H., and W. D. Hirt, 1987: Derechos: Widespread convectively induced windstorms. *Wea. Forecasting*, **2**, 32–49.

Johnson, J., P. L. MacKeen, A. Witt, E. D. W. Mitchell, G. J. Stumpf, M. D. Eilts, and K. W. Thomas, 1998: The storm cell identification and tracking algorithm: An enhanced WSR-88D algorithm. *Wea. Forecasting*, **13 (2)**, 263–276.

Jolliffe, I., 2002: *Principal component analysis*. Wiley Online Library, New York, 518 pp.

Jones, A., 1979: Electromagnetic wave scattering by assemblies of particles in the Rayleigh approximation. *Proc. Roy. Soc. London*, **366 (1724)**, 111–127.

Kaimal, J. C., and J. J. Finnigan, 1994: *Atmospheric boundary layer flows: their structure and measurement*. Oxford University, 289 pp.

Kaltenböck, R., G. Diendorfer, and N. Dotzek, 2009: Evaluation of thunderstorm indices from ECMWF analyses, lightning data and severe storm reports. *Atmos. Res.*, **93 (1-3)**, 381–396.

Kapsch, M. L., M. Kunz, R. Vitolo, and T. Economou, 2012: Long-term variability of hail-related weather types in an ensemble of regional climate models. *J. Geophys. Res.*, **117**, D15 107, 16 PP.

Kasemir, H. W., 1960: A contribution to the electrostatic theory of a lightning discharge. *J. Geophys. Res*, **65 (7)**, 1873–1878.

Klein, B. J., and J. J. Degnan, 1974: Optical antenna gain. 1: Transmitting antennas. *App. Optics*, **13 (9)**, 2134–2141.

Knight, C. A., and N. C. Knight, 1970: Hailstone embryos. *J. Atmos. Sci*, **27 (4)**, 659–666.

Knight, N. C., and A. J. Heymsfield, 1983: Measurement and interpretation of hailstone density and terminal velocity. *J. Atmos. Sci.*, **40 (6)**, 1510–1516.

Knupp, K. R., and W. R. Cotton, 1985: Convective cloud downdraft structure: An interpretive survey. *Rev. Geophys.*, **23 (2)**, 183–215.

Kober, K., and A. Tafferner, 2009: Tracking and nowcasting of convective cells using remote sensing data from radar and satellite. *Meteor. Z.*, **18 (1)**, 75–84.

Koebele, D., 2014: Analysis of Convergence Areas during Orographically Induced Hailstorms with the COSMO Model. M.S. thesis, 93 pp.

Kottmeier, C., and Coauthors, 2008: Mechanisms initiating deep convection over complex terrain during COPS. *Meteor. Z.*, **17 (6)**, 931–948.

Kunz, M., 2007a: The skill of convective parameters and indices to predict isolated and severe thunderstorms. *Nat. Hazards Earth Syst. Sci.*, **7**, 327–342.

Kunz, M., 2007b: The skill of convective parameters and indices to predict isolated and severe thunderstorms. *Natural Hazards and Earth System Science*, **7 (2)**, 327–342.

Kunz, M., 2011: Characteristics of large-scale orographic precipitation in a linear perspective. *J. Hydrol.*, **12 (1)**, 27–44.

Kunz, M., and P. I. Kugel, 2015: Detection of hail signatures from single-polarization C-band radar reflectivity. *Atmos. Res.*, **153**, 565–577.

Kunz, M., and M. Puskeiler, 2010: High-resolution assessment of the hail hazard over complex terrain from radar and insurance data. *Meteor. Z.*, **19 (5)**, 427–439.

Kunz, M., J. Sander, and C. Kottmeier, 2009: Recent trends of thunderstorm and hailstorm frequency and their relation to atmospheric characteristics in southwest Germany. *Int. J. Climatol.*, **29 (15)**, 2283–2297.

Laing, A. G., and J. M. Fritsch, 2000: The large-scale environments of the global populations of mesoscale convective complexes. *Mon. Wea. Rev.*, **128 (8)**, 2756–2776.

Lane, R. M. M. B., T. P., and T. Clark, 2000: Observations and numerical modelling of mountain waves over the Southern Alps of New Zealand. *Quat. J. Roy. Meteor. Soc*, **126 (569)**, 2765–2788.

Langhans, W., J. Schmidli, O. Fuhrer, S. Bieri, and C. Schär, 2013: Long-term simulations of thermally driven flows and orographic convection at convection-parameterizing and cloud-resolving resolutions. *J. Appl. Meteorology*, **52 (6)**, 1490–1510.

Lemon, L. R., and C. A. Doswell III, 1979: Severe thunderstorm evolution and mesocyclone structure as related to tornadogenesis. *Mon. Wea. Rev.*, **107**, 1184.

Levanon, N., and E. Mozeson, 2004: *Radar signals*. John Wiley & Sons, 403 pp.

Ligda, M. G., 1956: The radar observation of lightning. *J. Atm. Terrest. Phys.*, **9 (5-6)**, 309–346.

Lindloff, V., 2003: Hagel–Jedes Jahr Schäden in Millionenhöhe. *Kurier*, **(2)**, 18–21.

Long, J. S., 1987: A graphical method for the interpretation of multinomial logit analysis. *Sociol. Method Res.*, **15 (4)**, 420–446.

Longley, R. W., and C. Thompson, 1965: A study of causes of hail. *J. Appl. Meteorology*, **4 (1)**, 69–82.

Lozowski, E. P., and A. G. Beattie, 1979: Measurements of the kinematics of natural hailstones near the ground. *Quart. J. Roy. Meteor. Soc.*, **105 (444)**, 453–459.

Ludlam, F. H., 1958: The hail problem. *Nubila*, **1**, 12–96.

Lugauer, M., and P. Winkler, 2005: Thermal circulation in south bavaria–climatology and synoptic aspects. *Meteor. Z.*, **14 (1)**, 15–30.

Lukach, M., and L. Delobbe, 2013: Radar-based hail statistics over Belgium. *7th European Conference on Severe Storms (ECSS), 7-13 June 2013, Helsinki, Finland*.

Maddox, R. A., 1980: Mesoscale convective complexes. *Bull. Amer. Meteor. Soc.*, **61**, 1374–1387.

Mahieu, P., and E. Wesolek, 2011: Contribution to an European Adaptation of the enhanced Fujita Scale: Analysis of damages caused by tornadoes in France. *6th European Conference one Severe Storm (ECSS), 3-7 October 2011, Palma de Mallorca, Spain*.

Makitov, V., 1999: Organization and main results of the hail suppression program in the northern area of the province of Mendoza, Argentina. *J. Wea. Modification*, **31 (1)**, 76–86.

Markowski, P., and Y. Richardson, 2010: *Mesoscale meteorology in midlatitudes*, Vol. 3. John Wiley, 407 pp.

Markowski, P. M., and N. Dotzek, 2011: A numerical study of the effects of orography on supercells. *Atmos. Res.*, **100 (4)**, 457–478.

Marshall, J., W. Hitschfeld, and K. Gunn, 1955: Advances in radar weather. *Adv. Geophys.*, **2**, 1–56.

Marshall, J. S., and W. M. K. Palmer, 1948: The distribution of raindrops with size. *J. Meteor.*, **5 (4)**, 165–166.

Mason, B., 1971: *The physics of clouds*. Oxford University Press, Oxford, 540 pp.

Matsumoto, M., S. Saito, and I. Ohmine, 2002: Molecular dynamics simulation of the ice nucleation and growth process leading to water freezing. *Nature*, **416 (6879)**, 409–413.

Meischner, P., 2005: *Weather radar: principles and advanced applications*. Springer, Berlin, 337 pp.

Merino, A., E. García-Ortega, L. López, J. Sánchez, and A. Guerrero-Higueras, 2013: Synoptic environment, mesoscale configurations and forecast parameters for hailstorms in southwestern europe. *Atmos. Res.*, **122**, 183–198.

Mezeix, J., B. Vaissieres, and P. Admirat, 1976: Etude physique des chutes de grêle dans la région du Napf. Tech. rep., *University of Montpelier*, 34 pp.

Millot, C., and L. Wald, 1980: The effect of Mistral wind on the Ligurian current near Provence. *Oceanol. Acta*, **3 (4)**, 399–402.

Mohr, S., 2013: Änderung des Gewitter- und Hagelpotentials im Klimawandel. Ph.D. thesis, Karlsruhe Institute of Technology, 269 pp.

Mohr, S., and M. Kunz, 2013: Recent trends and variabilities of convective parameters relevant for hail events in Germany and Europe. *Atmos. Res.*, **123**, 211–228.

Mohr, S., M. Kunz, and B. Geyer, 2015a: Hail potential in Europe based on a regional climate model hindcast. *Geophys. Res. Lett*, **42 (24)**.

Mohr, S., M. Kunz, and K. Keuler, 2015b: Development and application of a logistic model to estimate the past and future hail potential in Germany. *J. Geophys. Res*, **120 (9)**, 3939–3956.

Mohr, S., M. Kunz, J. Speidel, and D. Piper, 2016: Long-term variability of the thunderstorm and hail potential in Europe. *18th European Geosciences Union General Assembly, 17-22 April 2016, Vienna, Austria*.

Moncrieff, M. W., and M. J. Miller, 1976: The dynamics and simulation of tropical cumulonimbus and squall lines. *Quart. J. Roy. Meteor. Soc.*, **102**, 373–394.

Monfredo, W., 2011: Investigation into the record hailstone on 23 July 2010 at Vivian, South Dakota, USA. *Weather*, **66 (8)**, 216–221.

Morgan Jr, G. M., and N. G. Towery, 1975: Small-scale variability of hail and its significance for hail prevention experiments. *J. Appl. Meteorology*, **14 (5)**, 763–770.

Morgan Jr, G. M., and N. G. Towery, 1976: *Crop Damage: Hailpad Parameter Study in Illinois*. Urbana, 59 pp.

Morris, R., 1986: The spanish plume-testing the forecasters nerve. *Meteorol. Mag.*, **115 (1372)**, 349–357.

Muriset, F., 2003: Schwergewitter auf der Alpennordseite der Schweiz. M.S. thesis, Berner Maturitätsschule für Erwachsene, 92 pp.

Musil, D. J., S. A. Christopher, R. A. Deola, and P. L. Smith, 1991: Some interior observations of southeastern Montana hailstorms. *J. Appl. Meteorology*, **30 (12)**, 1596–1612.

Nelson, S. P., 1983: The influence of storm flow structure on hail growth. *J. Atmos. Sci*, **40 (8)**, 1965–1983.

Nesbitt, S. W., and E. J. Zipser, 2003: The diurnal cycle of rainfall and convective intensity according to three years of trmm measurements. *J. Clim*, **16 (10)**, 1456–1475.

Nisi, L., O. Martius, A. Hering, M. Kunz, and U. Germann, 2016: Spatial and temporal distribution of hailstorms in the alpine region: a long-term, high resolution, radar-based analysis. *Quat. J. Roy. Meteor. Soc*, **142 (697)**, 1590–1604.

NOAA, 2010: Thunderstorms: Introduction. National Weather Service Weather Forecast Office, Silver Spring, USA, 2.

Noppel, H., U. Blahak, A. Seifert, and K. D. Beheng, 2010: Simulations of a hailstorm and the impact of CCN using an advanced two-moment cloud microphysical scheme. *Atmos. Res.*, **96 (2)**, 286–301.

Normand, C. W. B., 1938: On instability from water vapour. *Quart. J. Roy. Meteor. Soc.*, **64 (273)**, 47–70.

Orlanski, I., B. Ross, L. Polinsky, and R. Shaginaw, 1985: Advances in the theory of atmospheric fronts. *Adv. Geophys.*, **28**, 223–252.

Palencia, C., A. Castro, D. Giaiotti, F. Stel, F. Vinet, and R. Fraile, 2009: Hailpad-based research: A bibliometric review. *Atmos. Res.*, **93**, 664–670.

Pamdey, S., H. Kumar, and H. Rathor, 1976: Computation of Vertical Velocities during Western Disturbance over the Indian Region. *Rivista italiana di geofisica e scienze affini*, **3 (5-6)**, 252–254.

Parent du Châtelet, J., P. Tabary, and P. Lamarque, 2005: Evolution du réseau radar opérationnel de Météo-France pour une meilleure estimation des lames d'eau. *Hydrol. Cont.*, **49**, 1–4.

Pédeboy, S., 2015: Analysis of the French lightning locating system location accuracy. *International Symposium on Lightning Protection*, IEEE, 337–341.

Peltier, W., and T. Clark, 1979: The evolution and stability of finite-amplitude mountain waves. part ii: Surface wave drag and severe downslope windstorms. *J. Atmos. Sci*, **36 (8)**, 1498–1529.

Pierrehumbert, R., and B. Wyman, 1985: Upstream effects of mesoscale mountains. *J. Atmos. Sci.*, **42 (10)**, 977–1003.

Pruppacher, H. R., and J. D. Klett, 1997: *Microphysics of clouds and precipitation*, Vol. 18. Kluwer Academic Publishers, Dordrecht, Netherlands, 954 pp.

Przybylinski, R. W., 1995: The bow echo: Observations, numerical simulations, and severe weather detection methods. *Wea. Forecasting*, **10 (2)**, 203–218.

Púčik, T., P. Groenemeijer, D. Rỳva, and M. Kolář, 2015: Proximity soundings of severe and nonsevere thunderstorms in Central Europe. *Mon. Wea. Rev.*, **143 (12)**, 4805–4821.

Punge, H., K. Bedka, M. Kunz, and A. Werner, 2014: A new physically based stochastic event catalog for hail in Europe. *Nat. Hazards*, **73 (3)**, 1625–1645.

Punge, H., and M. Kunz, 2016: Hail observations and hailstorm characteristics in Europe: A review. *Atmos. Res.*, **176**, 159–184.

Puskeiler, M., 2013: Radarbasierte Analyse der Hagelgefährdung in Deutschland. Ph.D. thesis, Karlsruhe Institute of Technology, 226 pp.

Puskeiler, M., M. Kunz, and M. Schmidberger, 2016: Hail statistics for germany derived from single-polarization radar data. *Atmos. Res.*, **178**, 459–470.

Raghavan, S., 2013: *Radar meteorology*, Vol. 27. Springer, Dordrecht, 537 pp.

Rasmussen, R., and A. Heymsfield, 1985: A generalized form for impact velocities used to determine graupel accretional densities. *J. Atmos. Sci.*, **42 (21)**, 2275–2279.

Reynolds, O., 1883: An experimental investigation of the circumstances which determine whether the motion of water shall be direct or sinuous, and of the law of resistance in parallel channels. *Proc. Roy. Soc. London*, **35 (224-226)**, 84–99.

Rinehart, R. E., 1991: *Radar for Meteoroiogists I*. Rinehart Pub, 482 pp.

Robbins, N. B., 2012: *Creating more effective graphs*. Wiley, New York, 395 pp.

Rust, W. D., D. R. MacGorman, and R. T. Arnold, 1981: Positive cloud-to-ground lightning flashes in severe storms. *Geophys. Res. Lett*, **8 (7)**, 791–794.

Saltikoff, E., J.-P. Tuovinen, J. Kotro, T. Kuitunen, and H. Hohti, 2010: A climatological comparison of radar and ground observations of hail in finland. *J. Appl. Meteorology*, **49 (1)**, 101–114.

Sánchez, J. L., L. López, C. Bustos, J. L. Marcos, and E. García-Ortega, 2008: Short-term forecast of thunderstorms in Argentina. *Atmos. Res.*, **88 (1)**, 36–45.

Sánchez-Diezma, R., I. Zawadzki, and D. Sempere-Torres, 2000: Identification of the bright band through the analysis of volumetric radar data. *J. Geophys. Res*, **105 (D2)**, 2225–2236.

Sauvageot, H., 1992: *Radar meteorology*. Artech House, Norwood, 366 pp.

Schemm, S., L. Nisi, A. Martinov, D. Leuenberger, and O. Martius, 2016: On the link between cold fronts and hail in switzerland. *Atmos. Sci. Lett*, **17 (5)**, 315–325.

Schiesser, H., 1990: Hailfall: the relationship between radar measurements and crop damage. *Atmos. Res.*, **25 (6)**, 559–582.

Schleusener, R. A., 1960: An energy method for relative estimates of hail intensity. Tech. Rep. 1, *Colorado State University*, 6 pp.

Schmid, W., H. H. Schiesser, and B. Bauer-Messmer, 1997: Supercell storms in Switzerland: case studies and implications for nowcasting severe winds with Doppler radar. *Meteor. Appl.*, **4 (01)**, 49–67.

Schmidt, T., A. de la Torre, and J. Wickert, 2008: Global gravity wave activity in the tropopause region from champ radio occultation data. *Geophys. Res. Lett*, **35 (16)**.

Schulz, P., 1989: Relationships of several stability indices to convective weather events in northeast Colorado. *Wea. Forecasting*, **4**, 73–80.

Schuster, S. S., R. J. Blong, and M. S. Speer, 2005: A hail climatology of the greater Sydney area and New South Wales, Australia. *Int. J. Climatol.*, **25 (12)**.

Schwind, M., 1957: *Die Hagelhäufigkeit in der Bundesrepublik Deutschland*. Institut für Raumforschung, Dortmund, 35 pp.

Sekhon, R., and R. Srivastava, 1970: Snow size spectra and radar reflectivity. *J. Atmos. Sci*, **27 (2)**, 299–307.

Shapiro, A., K. M. Willingham, and C. K. Potvin, 2010: Spatially variable advection correction of radar data. part i: Theoretical considerations. *J. Atmos. Sci*, **67 (11)**, 3445–3456.

Simpson, J. E., 1994: *Sea breeze and local winds*. Cambridge University Press, Cambridge, 239 pp.

Skolnik, M. I., 1962: *Introduction to Radar Systems*, Vol. 2. McGraw-Hill Book Company, New York, 476 pp.

Smith, R. B., 1989: Hydrostatic airflow over mountains. *Adv. Geophys.*, **31**, 1–41.

Snyder, W. H., R. S. Thompson, R. E. Eskridge, R. E. Lawson, I. P. Castro, J. Lee, J. C. Hunt, and Y. Ogawa, 1985: The structure of strongly stratified flow over hills: dividing-streamline concept. *J. Fluid Mechan.*, **152**, 249–288.

Soden, B. J., and I. M. Held, 2006: An assessment of climate feedbacks in coupled ocean-atmosphere models. *J. Clim*, **19 (14)**, 3354–3360.

Sorbjan, Z., 1996: Effects caused by varying the strength of the capping inversion based on a large eddy simulation model of the shear-free convective boundary layer. *J. Atmos. Sci.*, **53 (14)**, 2015–2024.

Soula, S., H. Sauvageot, G. Molinie, F. Mesnard, and S. Chauzy, 1998: The CG lightning activity of a storm causing a flash-flood. *Geophys. Res. Lett*, **25 (8)**, 1181–1184.

Soula, S., Y. Seity, L. Feral, and H. Sauvageot, 2004: Cloud-to-ground lightning activity in hail-bearing storms. *J. Geophys. Res*, **109 (D2)**.

Soumekh, M., 1999: *Synthetic aperture radar signal processing*. Wiley, New York, 648 pp.

Steinacker, R., 1984: Area-height distribution of a valley and its relation to the valley wind. *Beiträge zur Physik der Atmosphäre*, **57 (1)**, 64–71.

Stensrud, D. J., 1996: Importance of low-level jets to climate: A review. *J. Clim*, **9 (8)**, 1698–1711.

Straka, J. M., 2009: *Cloud and precipitation microphysics: principles and parameterizations*. Cambridge University Press, Cambridge, 408 pp.

Stull, R. B., 1994: A convective transport theory for surface fluxes. *J. Atmos. Sci.*, **51 (1)**, 3–22.

Tabary, P., 2007: The new French operational radar rainfall product. Part I: Methodology. *Wea. Forecasting*, **22 (3)**, 393–408.

Tabary, P., J. Desplats, K. Do Khac, F. Eideliman, C. Gueguen, and J. Heinrich, 2007: The new French operational radar rainfall product. Part II: Validation. *Wea. Forecasting*, **22 (3)**, 409–427.

Tang, M., and E. R. Reiter, 1984: Plateau monsoons of the Northern Hemisphere: A comparison between North America and Tibet. *Mon. Wea. Rev.*, **112 (4)**, 617–637.

Tobin, M. C., 1974: Theory of phase transition kinetics with growth site impingement. I. Homogeneous nucleation. *J. Polym. Sc.*, **12 (2)**, 399–406.

Tuovinen, J. P., A. J. Punkka, J. Rauhala, H. Hohti, and D. M. Schultz, 2009: Climatology of severe hail in Finland: 1930-2006. **137 (7)**, 2238–2249.

Twomey, S., 1959: The nuclei of natural cloud formation part ii: The supersaturation in natural clouds and the variation of cloud droplet concentration. *Geofisica pura e applicata*, **43 (1)**, 243–249.

Vali, G., 1971: Quantitative evaluation of experimental results an the heterogeneous freezing nucleation of supercooled liquids. *J. Atmos. Sci*, **28 (3)**, 402–409.

Van Delden, A., 1998: The synoptic setting of a thundery low and associated prefrontal squall line in western Europe. *Meteorol. Atmos. Phys.*, **65 (1)**, 113–131.

Van Delden, A., 2001: The synoptic setting of thunderstorms in Western Europe. *Atmos. Res.*, **56 (1-4)**, 89–110.

Verspecht, A., G. Van Huylenbroeck, J. Buysse, and Coauthors, 2014: Extreme weather events in belgium: calamity fund and on-farm strategies hand in hand? *EAAE 2014 Congress "Agri-Food and Rural Innovations for Healthier Societies, 26-29 August 2014, Ljubljana, Slovenia*.

Vinet, F., 2001: Climatology of hail in France. *Atmos. Res.*, **56**, 309–323.

Vinet, F., 2002: La question du risque climatique en agriculture: le cas de la grêle en France. *Annales de géographie*, Ann. Geo., 592–613.

Viúdez, Á., J. Tintoré, and R. L. Haney, 1996: About the nature of the generalized omega equation. *J. Atmos. Sci.*, **53 (5)**, 787–795.

Wagner, H., 1932: Über Stoß-und Gleitvorgänge an der Oberfläche von Flüssigkeiten. *J. Appl. Mathem.*, **12 (4)**, 193–215.

Waldvogel, A., B. Federer, and P. Grimm, 1979: Criteria for the detection of hail cells. *J. Appl. Meteorology*, **18 (4)**, 12.

Waldvogel, A., W. Schmid, and B. Federer, 1978: The kinetic energy of hailfalls. part i: Hailstone spectra. *J. Appl. Meteorology*, **17 (4)**, 515–520.

Weisman, M. L., 1992: The role of convectively generated rear-inflow jets in the evolution of long-lived mesoconvective systems. *J. Atmos. Sci.*, **49 (19)**, 1826–1847.

Weisman, M. L., and J. B. Klemp, 1982: The dependence of numerically simulated convective storms on vertical wind shear and buoyancy. *Mon. Wea. Rev.*, **110**, 504–520.

Weisman, M. L., and J. B. Klemp, 1984: The structure and classification of numerically simulated convective storms in directionally varying wind shears. *Mon. Wea. Rev.*, **112 (12)**, 2479–2498.

Weisman, M. L., J. B. Klemp, and R. Rotunno, 1988: Structure and evolution of numerically simulated squall lines. *J. Atmos. Sci.*, **45 (14)**, 1990–2013.

Wesolek, E., and P. Mahieu, 2011: The F4 tornado of August 3, 2008, in Northern France: Case study of a tornadic storm in a low CAPE environment. *Atmos. Res.*, **100 (4)**, 649–656.

Wexler, R., and D. Atlas, 1963: Radar reflectivity and attenuation of rain. *J. Appl. Meteorology*, **2 (2)**, 276–280.

Whiteman, C. D., and J. C. Doran, 1993: The relationship between overlying synoptic-scale flows and winds within a valley. *J. Appl. Meteorology*, **32 (11)**, 1669–1682.

Willemse, S., 1995: A statistical analysis and climatological interpretation of hailstorms in Switzerland. Ph.D. thesis, Swiss Federal Institute of Technology, 204 pp.

Witt, A., M. D. Eilts, G. J. Stumpf, J. Johnson, E. D. W. Mitchell, and K. W. Thomas, 1998: An enhanced hail detection algorithm for the WSR-88D. *Wea. Forecasting*, **13 (2)**, 286–303.

Witt, A., and S. P. Nelson, 1991: The use of single-Doppler radar for estimating maximum hailstone size. *J. Appl. Meteorology*, **30 (4)**, 425–431.

Wold, S., K. Esbensen, and P. Geladi, 1987: Principal component analysis. *Chemo. int.Lab. Syst.*, **2 (1-3)**, 37–52.

Young, K. R., and B. León, 2009: Natural hazards in perú: causation and vulnerability. *Dev. Earth Surf. Proc.*, **13**, 165–180.

Zimmerli, P., 2005: Hagelstürme in Europa: neuer Blick auf ein bekanntes Risiko. Tech. rep., *Swiss Re*, 7 pp.

Zinner, T., H. Mannstein, and A. Tafferner, 2008: Cb-tram: Tracking and monitoring severe convection from onset over rapid development to mature phase using multi-channel meteosat-8 seviri data. *Meteor. Atmos. Phys*, **101 (3)**, 191–210.